DISSERTATION

Hybrid MOEMS Displacement Sensor and Accelerometer

Sensing Concept, Design, and Technology

ausgeführt zum Zwecke der Erlangung des akademischen Grades eines
Doktors der technischen Wissenschaften unter der Leitung von

Ao.Univ.Prof. Dipl.-Ing. Dr.techn. Franz Keplinger

Institut für Sensor- und Aktuatorsysteme

eingereicht an der Technischen Universität Wien
Fakultät für Elektrotechnik und Informationstechnik

von

Dipl.-Ing. Wilfried Hortschitz

Matrikelnummer: 9955615

Wien, September 2013

Contents

Kurzfassung

Inertialsensoren werden heute in verschiedensten Bereichen verwendet. Sie ermöglichen neuartige Produkteigenschaften und Dienstleistungen im Bereich der Unterhaltungselektronik generell aber auch speziell hinsichtlich mobiler Geräte. Durch eine genaue Messung der Bewegung der Erdoberfläche wird aber auch eine Vorhersage von Erdbeben möglich. Darüber hinaus finden sie seit Jahrzehnten Einsatz in der Automobilindustrie für sicherheitsrelevante Anwendungen. Der Großteil der komerziell erhältlichen Inertialsensoren nutzt kapazitive Messmethoden welche hinsichtliche weiterer Sensitivitätserhöhungen massive technologische Herausforderungen mit sich bringen.

In dieser Arbeit wird eine Messmethode basierend auf der Modulation von Lichtfluß durch ein Mikrosystem für Verschiebung, Vibration und Beschleunigung hinsichtlich der wichtigsten Aspekte analysiet. Die drei Hauptpunkte sind dabei die erreichbare Auflösung bezüglich einer differentiellen Auslenkung, die Implementierung von speziellen Übertragungsfunktionen durch die Formgebung der Modulatoren, und die Diskussion der damit zugänglichen als auch neuartiger Anwendungen. Die Auslenkungen werden durch Beschleunigungskräfte hervorgerufen, welche auf eine auf Federn aufgehängte Masse aus mono-kristallinem Silizium wirken. Diese Masse wirkt zugleich als ein Element einer variablen Apertur durch welche ein Lichtfluß die Mikrostruktur passiert. Dieser Lichtfluß stammt von einer LED und trifft, nachdem er den Modulator passiert hat, auf eine Photodetektor. Trotz der Verwendung von kostengünstigen optoelektrischen Komponenten wurden mit den Prototypen Verschiebewege von einigen Mikrometern und Auflösungen von sub $1\,\mathrm{pm}/\sqrt{\mathrm{Hz}}$ erreicht, welche sub $1\,\mu\mathrm{g}/\sqrt{\mathrm{Hz}}$ als Beschleunigungen entsprechen. Den beiden Apterturteilen wird durch die räumliche Trennung eine unterschiedliche Formgebung erlaubt. Damit wird die vorteilhafte und nahezu freie Gestaltung der Aperturen ermöglicht wodurch die Implementierung von passiven Transferfunktionen, für zum Beispiel die Linearisierung von nichtlinearen Eingangssignalen zu Stande kommt.

Verarbeitet werden können neben Beschleunigungen all jene Größen, welche in eine räumliche Auslenkung umsetzbar sind. Damit können Gravitation, Kräfte die dem elektromagnetischen Feld zugehören aber auch Druck oder Temperaturausdehnung sehr einfach mit diesem Auswerteprinzip aufgenommen werden. Zusammen mit der galvanischen Trennung der Krafteinbringung und der opto-elektronischen Auswertung werden damit schlussendlich eine Vielfalt an neuen Applikationen ermöglicht.

Abstract

Today, inertial sensors are used in many different fields of application such as enabling advanced features and novel services in consumer electronics or mobile devices. They can also be used to forecast earthquakes by precisely measuring ground motion. Additionally, they have seen decades of service for safety applications in the automotive industry. However, the majority of commercially available inertial sensing products rely on capacitive sensing which presents technological challenges regarding their further improvement in sensitivity.

Within this thesis, a transduction method for measuring displacement, vibration and inertia based on the modulation of a light flux through a microsystem is analyzed regarding its most important aspects. The three main subjects are the achievable resolution regarding differential deflections of incorporated components, the implementation of particular transfer characteristics by shaping modulator apertures, and the discussion of the most feasible as well as novel applications.

In the presented work, differential deflections are generated by inertial forces acting upon a spring suspended mass made from mono-crystalline silicon. The mass also acts as one element of a variable aperture for the light flux passing through the structure. This flux may originate from an attached LED and hits a photodetector after passing the modulator.

Using low-cost optoelectronic components, the characterized prototypes achieved displacement ranges of several microns combined with encouraging sub $1\,\mathrm{pm}/\sqrt{\mathrm{Hz}}$ resolutions corresponding to sub $1\,\mu\mathrm{g}/\sqrt{\mathrm{Hz}}$ in terms of acceleration.

The spatial separation of the two aperture parts involved allows different shapes for both parts. This yields the benefit that the aperture can be designed almost freely in shape enabling the implementation of passive transfer characteristics to, for example, linearize nonlinear input signals.

Beside inertial forces, any quantity that can be translated into spatial displacement may be converted as well. Thus gravitation, electromagnetic field related forces, and pressure or temperature expansion can be easily covered with this transduction principle. Together with the galvanic separation of the force actuation and the opto-electrical readout, this ultimately enables a wide range of completely novel applications.

Nomenclature

0.1 List of Abbreviations

CAD	Computer Aided Design
CCD	Charge-coupled Device
CD	Combdrive
CMOS	Complementary Metal Oxide Semiconductor
DRIE	Deep Reactive Ion Etching
FEM	Finite Element Method
LED	Light Emmiting Diode
LF-Mod	Lightflux Modulator
MEMS	Micro-Electro-Mechanical System
MOEMS	Micro-Opto-Electro-Mechanical System
MSA	Micro System Analyzer
PCB	Printed Circuit Board
PhTr	Phototransistor
PSD	Power Spectral Density
SEM	Scanning Electrode Microscope
SMD	Surface-Mounted Device
SOI	Silicon On Insulator
TF	Transfer Function
TIA	Transimpedance Amplifier

0.2 List of Symbols

A_{m}	input acceleration amplitude at the mass	m/s^2
η	responsitivity of receiver	$\mathrm{A/W}$
η_{PTD}	quantum efficiency of electron-hole pair generation	1
λ	wavelength	m
λ_{peak}	wavelength at peak emission	m
NEA	noise equivalent acceleration	$\mathrm{g}/\sqrt{\mathrm{Hz}}$
NED	noise equivalent deflection	$\mathrm{m}/\sqrt{\mathrm{Hz}}$
NED_{Br}	Brownian motion equivalent deflection	$\mathrm{m}/\sqrt{\mathrm{Hz}}$
NED_{E}	noise equivalent deflection for the electronics	$\mathrm{m}/\sqrt{\mathrm{Hz}}$
NED_{M}	noise equivalent deflection for the mechanical system	$\mathrm{m}/\sqrt{\mathrm{Hz}}$
$SNR_{\mathrm{mech,a}}$	signal to noise ratio for accelerative input	1
$SNR_{\mathrm{mech,v}}$	signal to noise ratio for vibrational input	1
g	gravitational unit	$9.81\mathrm{m/s}^2$
ν	frequency of the incident light	Hz
ω_0	natural angular frequency	1/s
ω_{res}	angular resonance frequency	1/s
$\overline{i_0^2}$	squared fluctuation of the phototransistor collector current	A^2
π	$\pi = 3.1415...$	
τ	transmission ratio for perpendicularly incident light	1
$\tilde{x_{\mathrm{f}}}$	mean deflection of the foundation	m
φ_{f}	phase of the foundation	1°
φ_{Out}	phase of the sensor output signal	1°

φ_S	phase of the sensor	1°
A_b	phototransistor base area	m^2
$A_\mathrm{c,m}$	consumed chip area of the seismic mass	m^2
A_eff	transparent, effective area of the apertures	m^2
a_f	acceleration of foundation	m/s^2
A_ol	overlapping area	m^2
A_op	area of the opening	m^2
b_mass	width of mass	m
b_op	width of opening	m
b_spring	width of spring	m
c	spring constant	N/m
c_l	speed of light	$2.99\,10^8\,{}^\mathrm{m}/_\mathrm{s}$
D	damping ratio	1
d	damping coefficient	$\mathrm{kg/s}$
d_δ	air damping due to shear waves	$\mathrm{kg/s}$
d_Sp	air damping between seismic mass and glass substrate	$\mathrm{kg/s}$
d_t	air damping at sidewalls	$\mathrm{kg/s}$
E	band gap energy	eV
E_x, E_y	Young's modulus of silicon in x and y direction	Pa
$F(\nu)$	photon flux rate per area	$\mathrm{J/m}^2$
$f(x)$	aperture related form function	m
f_β	phototransistors cutoff frequency	Hz
F_n	Brownian force on the mechanical part	N
f_0	resonance frequency	Hz

f_c	cut off frequency of electronical subsystem	Hz
F_ext	external force onto the mass	N
F	force at the mass	N
$g(x)$	aperture related form function	m
g_elec	gain of the optoelectrical subsystem	1
h	Planck-constant	$4.13\,10^{-15}\mathrm{eVs} = 6.62\,10^{-34}\mathrm{Js}$
$h(x)$	output transfer function	m^2
$H_\mathrm{a}(\omega)$	Acceleration induced mechanical transfer function	$\mathrm{m/m/s}^2$
$H_\mathrm{elec}(\omega)$	acceleration induced mechanical transfer function	$1/\mathrm{s}^2$
h_FE	DC current gain of the phototransistor	1
h_fe	incremental current gain of the phototransistor	1
$H_\mathrm{n}(\omega)$	Brownian motion transfer function	m/N
$H_\mathrm{S}(\omega)$	sensor transfer function	A/m
$H\mathrm{v}(\omega)$	vibration induced mechanical transfer function	m/m
$H(s)$	transfer function	1
I	illumination of the MOEMS	$\mathrm{A/m}^2$
i_D	darkcurrent	A
I_e	radiation intensity of the LED	W
i_off	photocurrent due to offset light flux at rest	A
$i_\mathrm{pc,0}$	collector current of a phototransistor	A
i_pc	photocurrent	A
i_x	photocurrent due to differential grating deflections	A
j	imaginary unit, $j = \sqrt{-1}$	
J_0	optical power density at the aperture array	$\mathrm{W/m}^2$

$J_{\lambda \mathrm{D}}$	average photocurrent density of the photodiode	$\mathrm{A/m^2}$
k_B	Boltzmann constant	$1.38 \cdot 10^{-23}$J/K
l_e	effective moving edge length	m
l_mass	length of mass	m
l_op	length of opening	m
l_spring	length of spring	m
m	seismic mass	kg
n	refraction index	1
n_rel	relative refraction index	1
nr_op	number of openings	
P_O	total radiated power	W
Q	quality factor	1
q	electron charge	$1.602 \cdot 10^{-19}\mathrm{C}$
R_Comp	resistor for offset compensation	Ω
R_OPAMP	resistor in TIA feedback loop	Ω
S_i	power spectral density of the photocurrent noise	$\mathrm{A^2/\sqrt{Hz}}$
S_V	noise voltage power spectral density	$\mathrm{V^2/Hz}$
S_x	noise equivalent displacement spectral density	$\mathrm{m^2/\sqrt{Hz}}$
S	sensitivity of the phototransistor	A/W
T	absolute temperature	K
t	silicon device thickness	m
t	thickness of the structure	m
t_Sp	thickness of the spacer	m
u	underetching	m

V_0	noise voltage	$\mathrm{V}/\sqrt{\mathrm{Hz}}$
V_{Out}	output voltage	V
W_0	width of the open aperture at rest	m
W_{open}	width of the open aperture	m
x_{d}	relative displacement of mass relative to the foundation	m
x_{f}	displacement of the foundation	m
x_{m}	displacement of the mass	m
X_{n}	Brownian motion deflection	$\mathrm{m}/\sqrt{\mathrm{Hz}}$
DR	dynamic range	dB

Chapter 1

Introduction

An essential part of the technical progress is based on the increasing number of physical and chemical quantities that can be detected or measured. Here, key components are sensors which convert the required quantity into an electrical signal. Typical examples are sensors for temperature, pressure, or acceleration. The number of available sensor principles and sensor types exceeds the corresponding number of the quantities by far, however, only a small subset of principles is suitable for miniaturization which is an essential prerequisite for integration and mass production and consequently for versatile applications and economical benefit.

Miniaturized, silicon based sensors have been available for decades [1] and continuously gain additional market shares due to the ongoing advances in micro system technology. While today's fast growing computational power in mobile systems is obvious for the average consumer, the progress in sensor technology is normally hidden.

Nowadays, for specific applications such as measuring acceleration, a number of established sensor principles [2] are available. The capacitive MEMS (Micro-Electro-Mechanical System) accelerometer is one of the best known examples, and is used, e.g. in consumer electronics or in safety applications such as the air bag sensor [3, 4]. These sensors are improved continuously and for particular applications special electronics are developed to augment the sensor performance, making these sensors highly specialized systems.

For a further expansion of the field of application for MEMS, novel types of sensors are crucial for exploiting new transduction principles. Beneficial for these new sensors is for instance, insensitivity to electrical interference, undisturbed operation in harsh environments where high temperature, high electromagnetic field or shock can additionally harm a typical vibration sensor device. Furthermore, the sensor's performance, its power consumption and the technological complexity regarding the fabrication are key features deciding on its successful adoption by a competitive market. Numerous transduction principles with exciting features have been published but only a few enable unattended operations as well as fabrication as an integrated MEMS based device.

This unsatisfactory situation was stimulating research on alternative transducers. In contrast to very sophisticated solutions published in literature, the current work attempts to find solutions that combine moderate cost and ease of manufacturing with excellent sensitivity data.

1.1 Objective and Structure of the Thesis

The objective of the thesis is to reveal the potential of light flux modulation as a transduction principle for Micro-Opto-Electro-Mechanical System (MOEMS) displacement sensors and accelerometer. Additionally, the advantages and novel characteristics offered by this type of sensor such as the implementation of virtually any transfer characteristics with passive means will be pointed out. The sensor principle is scalable and is furthermore analyzed regarding the fabrication of the MOEMS and the integration of optoelectronics and MEMS for creating a single miniaturized sensor device. The selected approach is generic and also enables transducers for measuring the electrostatic field strength as well as sensors for magnetic field measurement. Due to the generic nature of the sensor principle, only the applications as displacement and vibration sensor as well as accelerometer are discussed in detail in this thesis. Further feasible applications which will expand the field of application beyond those mentioned are briefly described in the outlook.

The thesis is structured as follows: In Sec. 1.2, an overview of related work covering the state of the art of displacement sensing is presented. Chapter 2 gives a description of the optical MEMS approach in more detail. The basic transfer characteristics are discussed including noise considerations of the MEMS and the optoelectronic parts. In chap. 3 the fabrication process of the MOEMS is presented followed by a discussion of the experimental results.

The consequences of the aperture design are discussed in chapter 4. Finally chapter 5 summarizes the work in the thesis in a conclusion and a short outlook. The thesis contains fragments of former publications with contributions by the author. These are marked with quotation marks and the referenced paper is listed at the end of each citation while adopted text inside the quotations is put into square brackets.

1.2 Related Work - State of the Art Overview

Various principles for sensing acceleration and displacement have been successfully transferred into mass market [5]. A classification of these miniaturized inertial sensors is possible by their transduction method. The diagram in Fig. 1.1 depicts a state of the art overview of inertial displacement and acceleration sensing with miniaturized devices [6, 7, 8, 9, 10, 11, 12, 13, 14, 15, 16, 17, 18]. Further material about the sensor principles to be discussed can be found in [19, 20, 21, 22, 23, 24]. The basic frequency characteristic of the conversion of the motion of the foundation into relative displacement of a spring-mass-damper system was inserted into Fig. 1.1 to illustrate the bandwidth of a sensor which was designed as an accelerometer and may be used as displacement sensors, or vice versa. The displacement resolution degrades below the resonance of a sensor whereas above the resonance the sensitivity is constant over frequency. For accelerometers, this behavior is slightly different. Here, the sensitivity is constant below the resonance while the resolution decreases beyond the resonance frequency.

”High inertial transduction efficiency may be achieved by heavy proof masses, leading to high inertial forces, in conjunction with a soft suspension. However, a heavy proof mass combined with a compliant suspension results [also] in a large displacement bias due to gravitational forces.

Moreover, soft suspensions combined with small gaps between [e.g.,] capacitor plates make this type of transducers very vulnerable to collapses of the plates gap caused by the inherent instability of the electrostatic attraction [25, 26].”[27] Tunneling transducers and some optical transducers like the one described by [18] do feature small gaps between deflectable and fixed MEMS parts necessitating relatively mechanically stiff systems or a closed loop control to avoid damage of the system when exposing the sensor to high acceleration or shock.

In particular, the sensors with the best displacement resolution in Fig. 1.1 ([15, 18]) were operated in extensive laboratory arrangements and are not integrated or integrable to compact sensors devices. Furthermore, most groups do not detail the power consumption of their device, and many are operated under low pressure.

Below, the main types of transducers will be discussed in detail.

Capacitive MEMS sensors “Capacitive transducers utilize the deflection of spring suspended capacitor plates which act also as proof mass of the arrangement subjected to inertial forces. Inertial forces compete with gravi-

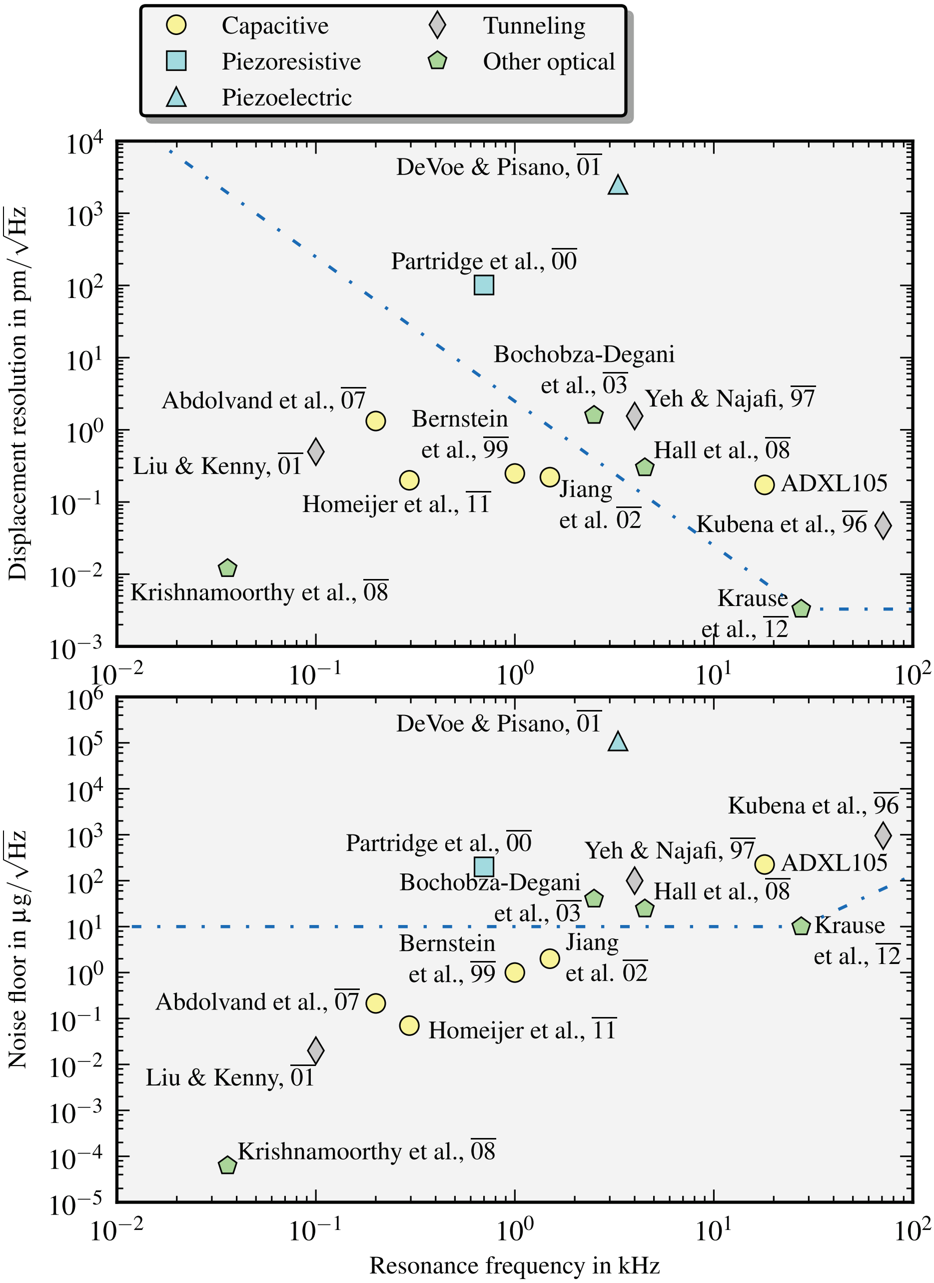

Figure 1.1: Displacement and acceleration resolutions of various MOEMS sensors. The corresponding frequency characteristics of a critically damped mass-spring transducer (blue dot-dashed line) is schematically added to indicate the course characteristic of displacement resolution for different sensors.

tation and the force on the proof mass generated by the Brownian motion of the ambient atmosphere [11]. This random force imposes an ultimate sensitivity limit on the inertial and displacement transduction. Several published sensors approach this thermal noise limit of the mechanical part, whereas the typical resolution of commercial products typically ranges from 3 μm/s² to about 10 mm/s² (approximately 0.3 μg to 1 mg where g denotes the unit gravity) [2].“[27]

“Recently, high-resolution capacitive transducers utilizing the fringe field of closely spaced planar microelectrode arrays were reported [28]. They apply a fixed planar array of interdigital electrodes featuring alternating potentials of the driving signals. The second electrode pattern on the movable mass is connected to charge amplifiers to enable position sensing. Hence, insulated interconnection leads have to be attached to the springs to connect the array of electrodes on the seismic mass. To achieve high displacement resolution, the array planes must be positioned as closely as possible. A high displacement resolution [of sub-pm] was reported for such structures. However, large displacements require specific measures due to the periodicity of the transducer characteristic [28, 29, 30].”[27]

Nevertheless, sophisticated evaluation circuits with low power consumption [31, 32] are available and monolytically integrable [33] for capacitive MEMS sensors making them extraordinarily attractive for mobile devices and mass markets.

Piezoresistive MEMS sensors “MEMS piezoresistive transducers convert mechanical stresses generated in dedicated parts of the MEMS suspension into electrical signals. Stresses are induced by displacements of the suspended structure due to, e.g., inertial or gravitational forces. The piezoresistive conversion depends on the temperature and therefore these sensors show an unwanted temperature dependency [1]. Furthermore, they typically suffer from 1/f noise limiting the displacement resolution. Despite these disadvantages the seamless integration of piezoresistors with microelectronic circuits should be mentioned.”[27]

Piezoelectric MEMS sensors Although piezoelectric sensors made from quartz are cost-effective, they exhibit a limited sensitivity and are difficult to integrate with other MEMS components and ICs [19, 34, 35]. Piezoelectric materials such as PZT ceramic feature higher sensitivities but are incompatible with most processes in MEMS and CMOS (Complementary Metal Oxide Semiconductor) industry.

Tunneling MEMS sensors This transduction can be highly sensitive, but requires a closed loop control to adjust the nonlinear tunneling current depending on the distance of the electrodes. The control is further necessary to avoid damage of the tunneling tip electrode when exposing the sensors to high acceleration or shock [22, 24]. Most likely, due to the challenging fabrication and the required control, this type of sensor did not gain any market share in the MEMS mass markets. Furthermore, there are no compact sensor devices based on tunneling effects available.

Optical MEMS sensors "The high resolution of grating-based displacement and inertial transduction is well recognized by the sensor community [5, 15]. There are various device concepts but most published concepts and implementations are based on reflection modulation [15, 16, 36] and utilize various diffraction phenomena. [These] conversion principles suffer from limited variability of the displacement transduction characteristic. Modulation of light transmission by MEMS is found only occasionally on a very modest level of sophistication [17, 37]."[27]

Recently, a new type of MOEMS accelerometer was reported. In this MOEMS two sets of photonic crystal optomechanical cavities separated by a small gap and fixed to the seismic mass and the foundation are used [18]. This MOEMS exhibits excellent displacement resolution, but high resonance frequencies have to be chosen for these types of senors to avoid damage to the closely spaced cavities sets. In other words, the transduction of displacement becomes worse the lower the exciting frequency becomes.

Finally, new optical chip-chip interconnection as introduced by [38] may enable complete new MOEMS sensor concepts in the future.

Chapter 2

Sensor Principle

2.1 The Optical MEMS Sensor

”The general concept [uses] optoelectronic transduction of displacement or inertia by a hybrid implementation of an optical modulator, an LED, and a photodetector. The light flux received at the photodetector is modulated by in-plane relative movement of two stencil masks which usually represent arrays of apertures, in short called apertures. Therefore, one mask is placed in front of the second. By illuminating the stencil pair from the front side, the transmitted light intensity can be measured with a photo-diode placed at the backside of the apertures (Fig. 2.1). For proof of concept a MEMS inertial sensor was chosen, where one mask is attached to a mass that is suspended by springs to a silicon frame. This mask can move in-plane driven by inertial forces. [In] contrast, the second grating is fixed to the frame which in turn is fixed to a vibrating body. The utilized optoelectrical components were selected as SMD (Surface-Mounted Device).

Usually, the frame of both masks and the photodetector are held together by a thin spacer [e.g., of SU-8 resist] which can be structured by photolithography. The SU-8 approach well defines the distance between the grating planes and acts simultaneously as a bonding promoter. Due to the in-plane movement of the MEMS mass, squeeze film damping is virtually negligible. Therefore, relatively high quality factors of the optical transducer are achieved even at ambient pressure and hermetical sealing is not mandatory.

The concept of the transducer depicted in Fig. 2.1 is easily understood with a simple ray optics approach. When the movable MEMS grating is displaced, the transmitted light flux changes according to the shading by both gratings (Fig. 2.2).

This modulation is converted into an electrical signal by a suitable photodetector which is preferably attached to the frame of the MEMS to

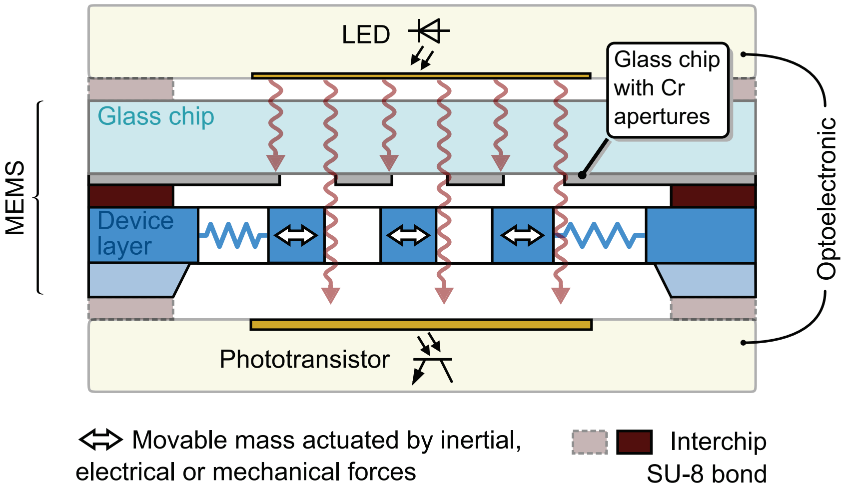

Figure 2.1: Schematic cross-section of the sensor for a fully encapsulated device. The emitted light flux is partially blocked by two microstructured gratings. The output signal of the phototransistor is proportional to the deflection of the movable mass.

minimize stray light effects. It may also serve as a part of the sensor encapsulation."[27]

The transfer characteristic between input deflection and output signal also depends on the shape of the openings. Additionally, the transfer characteristics is influenced by the rest position of the movable grating. For instance, when the grating pair is completely opaque at a chosen rest position, the spatial direction information is lost. A complete opaque grating pair rises also technological issues regarding the alignment of the two gratings. Related examples are discussed in more detail in section 4.5.2 and section 3.2.1.

Unique Characteristics

The presented sensor principle distinguishes itself from others transduction methods by several unique characteristics:

- The **galvanic separation** of the MEMS and the optical readout offers the possibility to use the sensor in harsh environments when combining the readout with, e.g., optical fibers.

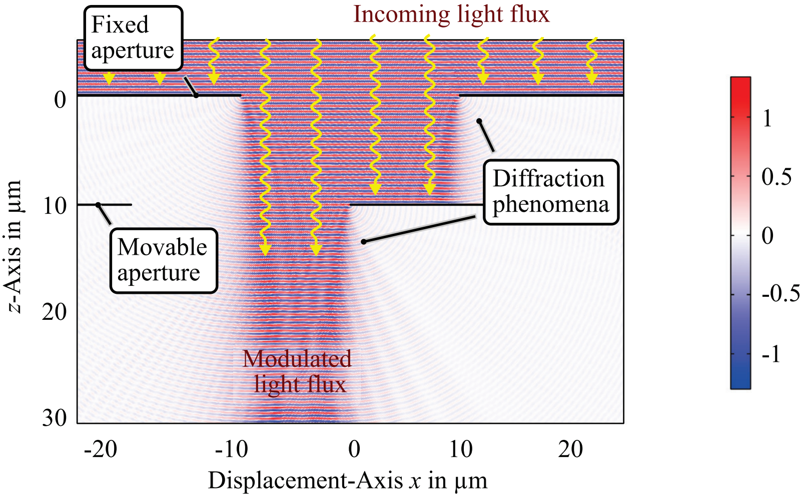

Figure 2.2: FEM simulation of light propagating through partially shading planar apertures arranged in two different planes. Assumptions: An incident plane wave (wavelength = 500 nm) arrives at the top of the fixed aperture. The width of the openings in both aperture gratings is 20 µm. A 10 µm gap between the gratings and perfectly absorbing boundaries were modeled. If the apertures are displaced with respect to each other, the transmitted light flux will change.[27]

- The spacial separation of the MEMS gratings, the relatively large dimensions of the apertures and no need for narrow gaps for the transduction imply **simplicity of the MOEMS fabrication**.
- The **shape of the openings** offers a **wide design scope** of the transfer characteristics of the MOEMS.
- **Broad options** are given **for designing the seismic mass, the stiffness and the viscous damping** of the MEMS due to the spatial separation of the aperture gratings and the freely moving mass, usually operating at ambient pressure.
- An **electromechanical feedback loop** can easily be implemented by incorporating combdrive actuators acting onto the movable mass.

Because the transduction mechanism is based on the relative displacement of a mask, an application as displacement sensor is obvious. Nevertheless, at the same time is the sensor vulnerable to acceleration of the frame, requiring different design considerations. Furthermore, an application as seismometer based on the evaluation of velocity variations is feasible.

2.2 Transfer Characteristics

In the presented assembly, the MOEMS sensor incorporates electronic as well as mechanic components which act unidirectionally. From a system point of view, these subsystems are connected in series and can, therefore, be analyzed separately. First, the impact of the serial connection on the transfer characteristics will be discussed.

2.2.1 Sensor Transfer Function

Due to the serial connection of the mechanical and opto-electrical subsystems, the total transfer function of the MEMS is given by the product

$$H_{\mathrm{S}}(s) = H_{\mathrm{mech}}(s) \cdot H_{\mathrm{elec}}(s) \quad . \tag{2.1}$$

$H_{\mathrm{S}}(s)$ is the sensor transfer function without feedback. A system overview is given in Fig. 2.3 with all input and output values. The subsystems are discussed in detail in the following sections.

2.2.2 Analytical Model of the Micro-mechanical Subsystem

"Based on the mechanical design of the MEMS device, the transduction is expected to exhibit a second-order high pass characteristic to seismic actuation, i.e., for accelerated motion of the Si frame. For gravitational forces [acting directly] on the spring-suspended mass, a second-order low pass characteristic is envisioned."[27]

The general differential equation of the motion for a damped spring supported mass suspended to the foundation can be written as

$$m\ddot{x}_{\mathrm{m}} + d \cdot (\dot{x}_{\mathrm{m}} - \dot{x}_{\mathrm{f}}) + c \cdot (x_{\mathrm{m}} - x_{\mathrm{f}}) + F_{\mathrm{ext}} = 0 \quad , \tag{2.2}$$

where x_f is the foundation excitation, $\ddot{x}_{\mathrm{m}}$, $\dot{x}_{\mathrm{m}}$, x_{m} is the acceleration, the velocity, and the deflection of the mass, respectively. The movable mass is denoted m, d is the damping coefficient (e.g., for slide film damping [23]) and c the spring constant. The force F_{ext} is the sum of all external forces directly acting on the mass, such as gravity. In the case of a MEMS device this also can be a force generated by a comb drive.

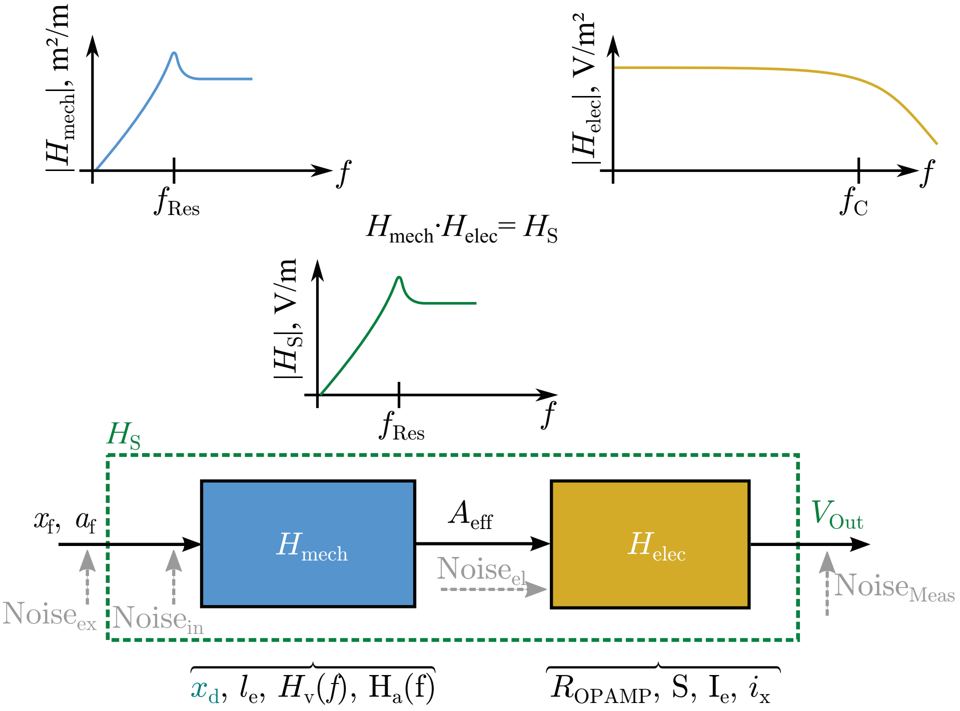

Figure 2.3: Schematic of the sensor transfer function H_S and its subsystems. The input deflection x_f (acceleration a_f) of the foundation is transferred to the transparent area of the apertures A_eff, the output of the mechanical subsystem H_mech (H_v, H_a). R_OPAMP is the gain of the current to voltage conversion resulting in an output voltage $V_\mathrm{Out} = i_\mathrm{x} \cdot R_\mathrm{OPAMP}$. The generated photocurrent can be expressed as $i_x = S \cdot I_\mathrm{e} \cdot A_\mathrm{eff}$, where S is the sensitivity of the phototransistor and I_e is the radiation intensity of the LED. The noise source $\mathrm{Noise}_\mathrm{ex}$ includes all extrinsic noise sources such as acoustic and mechanical coupling during the measurements. $\mathrm{Noise}_\mathrm{in}$ and $\mathrm{Noise}_\mathrm{el}$ are the intrinsic thermal noise and the electrical noise originating from the optoelectronic, respectively. $\mathrm{Noise}_\mathrm{Meas}$ is the noise introduced by the measurement equipment [39, 40].

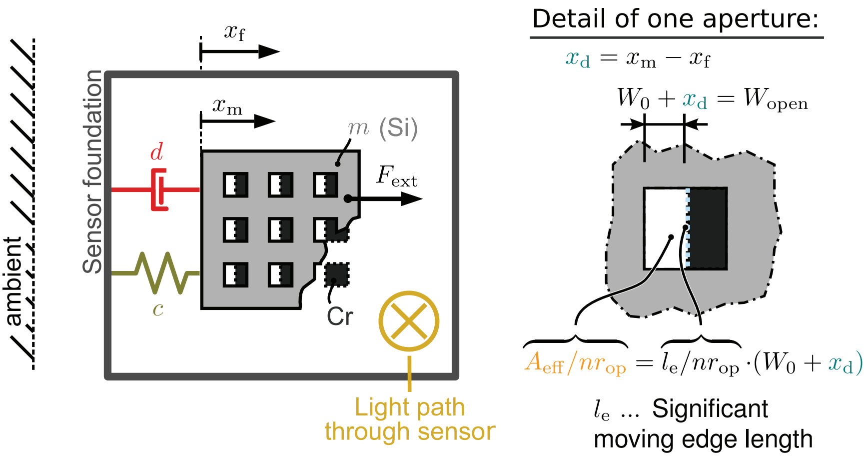

Figure 2.4: Schematic drawing of the MEMS which is excited at the foundation forming a mechanical second-order high pass system according to Eq. 2.6. A_eff is the transparent and therefore effective area of the apertures and nr_op is the number of openings. Here the light flux is modulated by the perforated silicon (Si) mass and the pattern fabricated in chromium (Cr), fixed to the foundation.

Excitation at the Foundation

For excitation at the foundation such as seismic actuation and without additional external forces, the equation of motion for the mass is

$$m\ddot{x}_\mathrm{d} + d \cdot \dot{x}_\mathrm{d} + c \cdot x_\mathrm{d} = -m\ddot{x}_\mathrm{f}, \tag{2.3}$$

introducing the relative deflection $x_\mathrm{d} = x_\mathrm{m} - x_\mathrm{f}$ between mass displacement x_m and motion of foundation x_f (Fig. 2.4). The differential Eq. 2.3 can be rewritten by applying the unilateral Laplace transformation defined by

$$X(s) = \mathcal{L}\{x(t)\} = \int_{0-}^{\infty} x(t)e^{-st}\mathrm{d}t\,, \tag{2.4}$$

to the second-order differential Eq. 2.3 to obtain the regular equation

$$s^2 \cdot X_\mathrm{d}(s) + s \cdot \frac{d}{m} \cdot X_\mathrm{d}(s) + \frac{c}{m} \cdot X_\mathrm{d}(s) = -s^2 \cdot X_\mathrm{f}(s) \quad . \tag{2.5}$$

For vibrational input at the foundation the corresponding transfer function

$$H_\mathrm{v}(s) = \frac{X_\mathrm{d}(s)}{X_\mathrm{f}(s)} = -\frac{s^2}{s^2 + \frac{d}{m}s + \frac{c}{m}} \tag{2.6}$$

exhibits a second-order high pass characteristic with a resonance at the (undamped) natural angular frequency

$$\omega_0 = \sqrt{\frac{c}{m}} \quad . \tag{2.7}$$

The magnitude response of the vibration sensor with the deflection signal x_f as input is a measure for the sensitivity of the system and is given by

$$|H_\mathrm{v}(\omega)| = \frac{m\,\omega^2}{\sqrt{d^2\omega^2 + (m\,\omega^2 - m\omega_0^2)^2}} \tag{2.8}$$

This mechanical transfer characteristics of typical MEMS sensors are shown in Fig. 2.5 illustrating the influence of the mass. Equation 2.8 can be simplified, for $\omega \gg \omega_0$, to

$$|H_\mathrm{v}(\omega)| = 1 \tag{2.9}$$

which does not depend on the mass m. This can be easily tested in Eq. 2.8 with $d \ll 1$ and $\omega \gg \omega_0$.

Acceleration of the Mass

The application of the system as an accelerometer becomes obvious by replacing $\ddot{x}_\mathrm{f}$ in Eq. 2.3 with a_f, i.e., the input acceleration. The related transfer characteristic for converting an acceleration into a differential deflection reads

$$H_\mathrm{a}(s) = \frac{X_\mathrm{d}(s)}{s^2 \cdot X_\mathrm{f}(s)} = \frac{X_\mathrm{d}(s)}{A_\mathrm{f}(s)} = -\frac{m}{ms^2 + ds + c}, \tag{2.10}$$

The corresponding magnitude response which is equivalent to the sensitivity of the system is given by

$$|H_\mathrm{a}(\omega)| = \frac{m}{\sqrt{d^2\omega^2 + (m\omega^2 - m\omega_0^2)^2}} \quad , \tag{2.11}$$

exhibiting a magnitude response analogous to a second-order low pass with a resonance at ω_0. Figure 2.6 depicts $|H_\mathrm{a}(\omega)|$ for a typical micro-mechanical

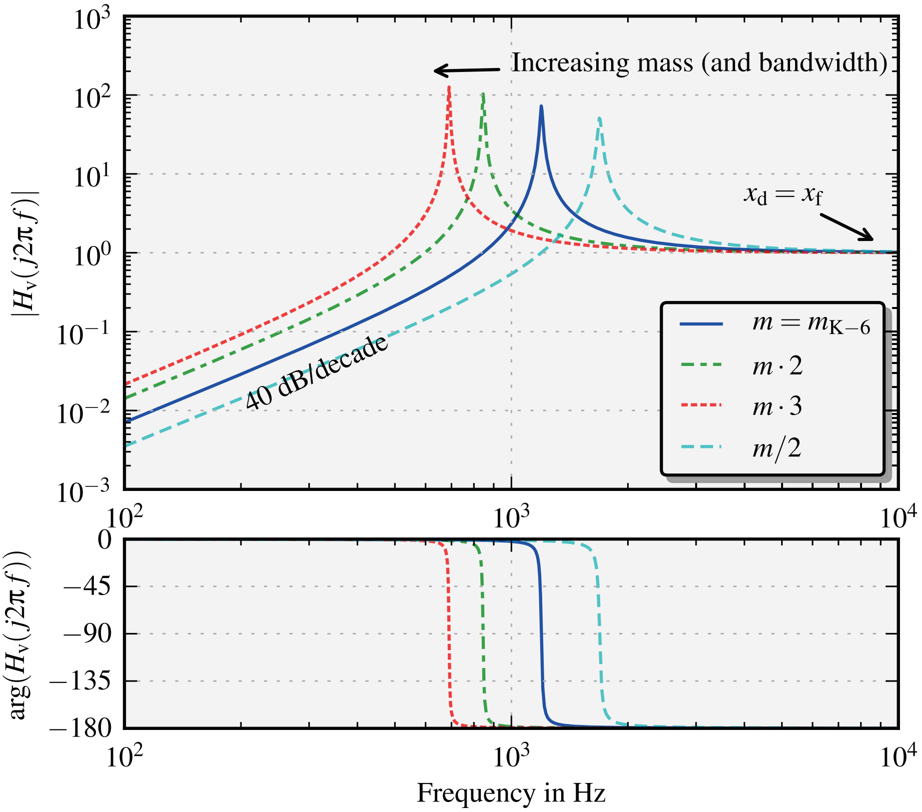

Figure 2.5: Bode plots of four mass-spring-damper systems for input excitation at the foundation x_f and the differential deflection x_d as output. The systems differ in their seismic mass. The mechanical parameters were taken from a fabricated sensor (K-6, listed in Sec. 3.4). The systems exhibit different natural frequencies influencing their bandwidth. The damping coefficient and the stiffness are the same for all systems. The magnitudes approximate unity for frequencies far above the natural frequency. For these high-frequency vibrations, the spring suspended mass does not follow the vibrations of the foundation due to its inertia, resulting in $x_d = x_f$.

system with various values of the mass. Equation 2.11 can be simplified for $\omega \ll \omega_0$ to

$$|H_\mathrm{a}(\omega)| \propto \frac{1}{\omega_0^2} = \frac{m}{c} \quad . \tag{2.12}$$

Hence, the magnitude response of the relative displacement below the natural frequency is directly proportional to the mass m and inversely proportional to the stiffness c. Nevertheless, both values, m and c, do also effect the natural frequency and, therefore, the bandwidth of the system.

2.2.3 Mechanical Subsystem

The relative displacement of the apertures which is read out optically is coupled by inertial forces to the motion of the foundation. Hence, the mechanical subsystem is suited for transduction of acceleration as well as displacement and velocity are related to vibrations of the foundation.

The transduction of velocity is frequency dependent for any frequency in contrast to the displacement and acceleration conversion which exhibit regions of flat frequency response. However, in the design of the mechanical subsystem the preferred application must be taken into account.

The low frequency cutoff of a vibration sensor is lowered by the resonance frequency, while simultaneously the bandwidth of the sensor increases (see Fig. 2.5 and Eq. 2.6) [13]. In the accelerometer mode, a wide bandwidth is achieved by increasing its resonance frequency, but in turn, the displacement resolution at low frequencies of the resulting system decreases.

“Low resonance frequencies require a low c/m ratio of the MEMS structure [primarily achieved by incorporating softer springs]. Therefore, low resonance frequencies are coupled to extended mass displacement $x_\mathrm{d} = F/c$. Furthermore, the structure becomes more vulnerable to mechanical shocks or [forces acting directly on the proof mass, [such as] gravity. The latter can cause snap-in] for variable gap capacitive transducers.

Obviously, there are only few sensitive MEMS transducers based on a capacitor gap variation featuring a resonant frequency below ~1 kHz (compare with Fig. 1.1).”[27]

One benefit of the MOEMS in this context is that the freely movable mass offers a large scope for the independent design of the mass and the springs without the constraints of narrow gaps and small deflection ranges as given for, e.g., capacitive or tunneling displacement transducers.

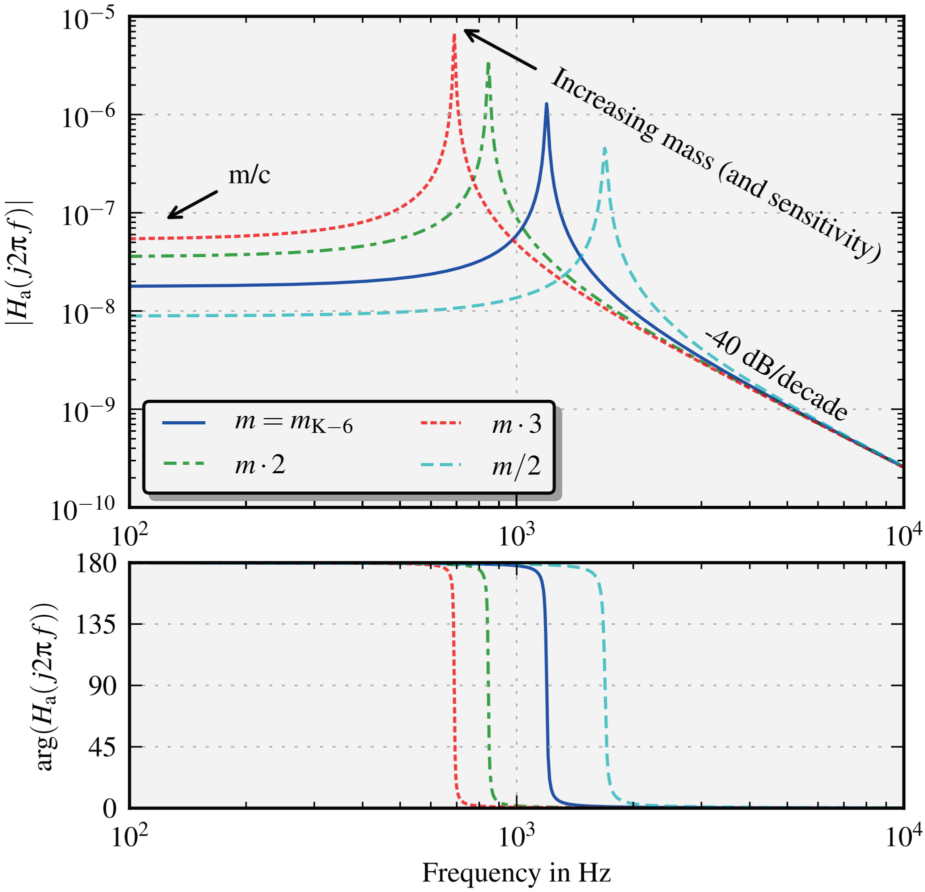

Figure 2.6: Magnitude response of mass-spring-damper systems with an acceleration acting on the mass. The systems differ in their seismic mass and exhibit, therefore, different natural frequencies. The mechanical parameters are taken from a fabricated sensor (K-6, listed in Sec. 3.4). The magnitude is proportional to m/c at low frequencies. The bandwidth where the systems exhibit high sensitivity varies with the resonance frequency and is lowered with increasing mass. The same response is achieved by lowering the stiffness while setting the mass to a fixed value.

Characterization of the Mechanical Subsystem

Figure 2.7 shows the results of the mechanical characterization of a prototype MOEMS (chip J-18) obtained with the in-plane stroboscopic mode of a Mico-system-analyzer. A detailed overview of the measurement set-up is discussed in Sec. 3.3.1. The data confirms the second order high pass model of the mechanical transfer characteristic $H_{\mathrm{v}}(f)$. The deviations between model and measurements at lower frequencies are due to the small deflections of less than 100 nm of the foundation and the mass, resulting in a large relative error of the computed difference of deflections, $x_{\mathrm{d}} = x_{\mathrm{m}} - x_{\mathrm{f}}$. As the excitation frequency proceeds towards the resonance, the deflection of the mass increases and, therefore, the relative error decreases resulting in a smooth transfer function above the resonance. The good agreement between the mechanical transfer function $H_{\mathrm{v}}(\mathrm{f})$ and the sensor $H_{\mathrm{S}}(f)$ transfer function suggests a flat transfer function of the opto-electrical readout $H_{\mathrm{elec}}(f) = g_{\mathrm{elec}}$ in the measured frequency range (compare Sec. 2.2.5).

2.2.4 Mechano-optical Coupling

The apertures in the silicon part as well as in the chromium mask are arranged by now as regular rectangle arrays with equal pitch. “Because [of the uniform illumination] the presented intensity modulation does not depend on the spatial extend of the gratings. [The] displacement of the edges and areas of the whole grating can also be considered as changes of one single *super-aperture*.

For the time being, both apertures are considered to be rectangularly shaped (Fig. 2.4 and Fig. 4.3) and the aperture in the silicon is always fabricated as an [opening] inside the intransparent moving mass. [Neglecting diffraction effects], the transparent and, therefore, effective area A_{eff}, where the light flux can pass through both apertures is also rectangularly shaped and can be expressed by $A_{\mathrm{eff}} = (x_{\mathrm{d}} + W_0) \cdot l_{\mathrm{e}}$, where l_{e} is the effective moving edge length [and W_0 denotes the slit width of the apertures of the unloaded system] (Fig. 2.4 and Fig. 4.3). To describe the complete mechanical behavior in terms of A_{eff}, the deflection transfer function $H_{\mathrm{v}}(s)$ between x_{f} and x_{d} has to be extended with the [effective] moving edge length l_{e}, resulting in” [41]

$$H_{\mathrm{mech}}(s) = (H_{\mathrm{v}}(s) + W_0 X_{\mathrm{f}}) \cdot l_{\mathrm{e}} = \left(\frac{X_{\mathrm{d}}}{X_{\mathrm{f}}} + W_0 X_{\mathrm{f}} \right) \cdot l_{\mathrm{e}} = \frac{\mathcal{L}\left\{A_{\mathrm{eff}}(t)\right\}}{X_{\mathrm{f}}} \quad . \tag{2.13}$$

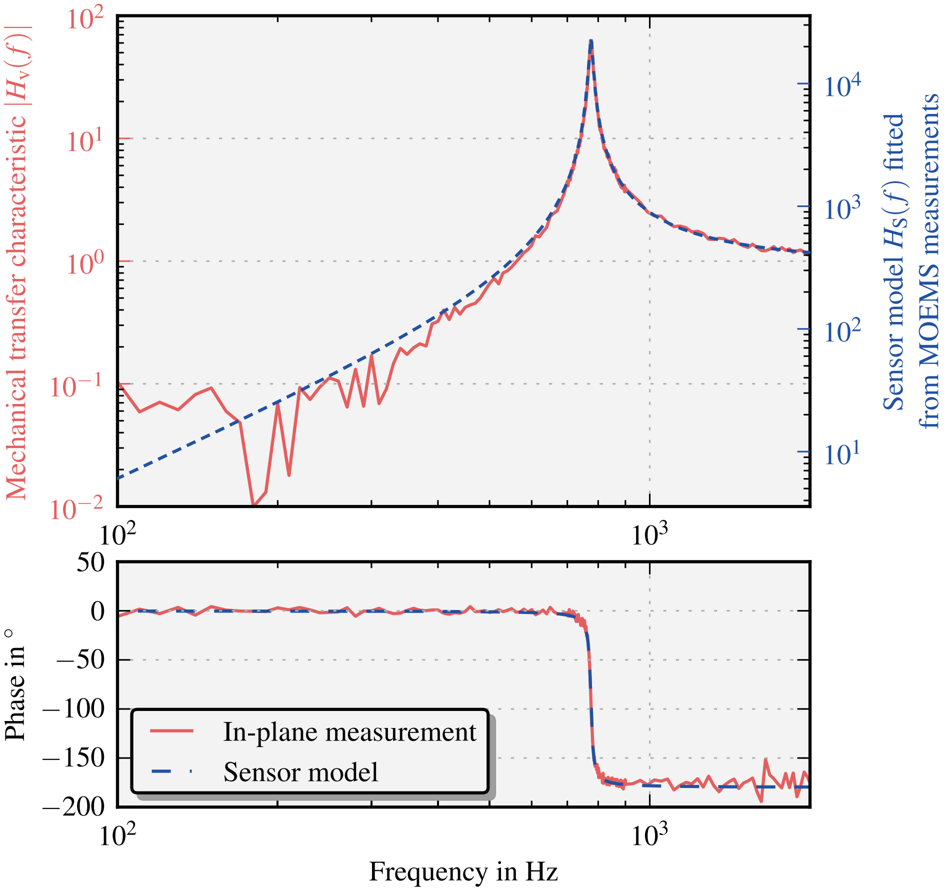

Figure 2.7: Comparison of magnitude and phase data from an in-plane measurement with an ideal second order high pass model of the sensor J-18 revealing good agreement. The deviations at lower frequencies are mainly due to measurement errors of the small relative displacement of the foundation $\ll 100\,\mathrm{nm}$ which complicates the evaluation of the in-plane observation. The evaluation of the presented data is also discussed in detail in Fig. 3.20.

Hence, the transparent cross-section area A_{eff} is the output variable of the mechanical system. Furthermore, A_{eff} could be the characteristic output variable of the complete sensor transfer function considering a flat transfer function of the opto-electrical subsystem.

2.2.5 Optoelectrical Subsystem - Electrical Circuit

The optoelectrical subsystem is characterized by an extraordinarily simple and linear readout.

"Figure 2.8 shows the electrical circuit biasing the LED, the photodetector, as well as the amplifying readout stage. The MOEMS modulates the light flux from the LED to the photodetector and, therefore, the photocurrent out of the detector. The presented [MOEMS] device is [discussed] for single direction excitation[. The] difference between the photocurrent i_{pc} and the darkcurrent i_{D} is directly proportional to the total [transparent] or effective area A_{eff} of the apertures

$$i_{\text{pc}} - i_{\text{D}} = i_{\text{pc,0}} + i_{\text{x}} \propto A_{\text{eff}} = l_{\text{e}} \cdot (W_0 + x_{\text{d}}), \tag{2.14}$$

where [i_{x} is the photocurrent change generated by differential deflections of the gratings, and $i_{\text{pc,0}}$ corresponds to the photocurrent of the unloaded system], W_0 denotes the slit width of the apertures of the unloaded system while l_{e} is the total length of the moving edges (see Fig. 2.4)."[27] The relation between the photocurrents and the mechanical properties can also be expressed as

$$\underbrace{i_{\text{D}} + \overbrace{i_{\text{pc,0}}}^{\propto W_0}}_{i_{\text{off}}} + \underbrace{i_{\text{x}}}_{\propto x_{\text{d}}} = i_{\text{pc}} \quad . \tag{2.15}$$

"The photodetector is forward biased [by] a constant voltage supplied to the inverting input of the op-amp. This voltage can be adjusted with $R_{\text{OPA+1}}$ and $R_{\text{OPA+2}}$. The [transimpedance amplifier (TIA)] converts the photocurrent modulations into a voltage signal. The conversion gain g_{elec} is set by the resistor R_{OPAMP} [resulting in]

$$V_{\text{Out}} = i_{\text{pc}} \cdot R_{\text{OPAMP}} \quad . \tag{2.16}$$

The generated photocurrent can be expressed [in simplified terms] as $i_{\text{pc}} = S \cdot I_{\text{e}} \cdot A_{\text{eff}}$, where S is the sensitivity of the phototransistor and I_{e} is the radiation intensity of the LED. The [discussed MOEMS was designed to have

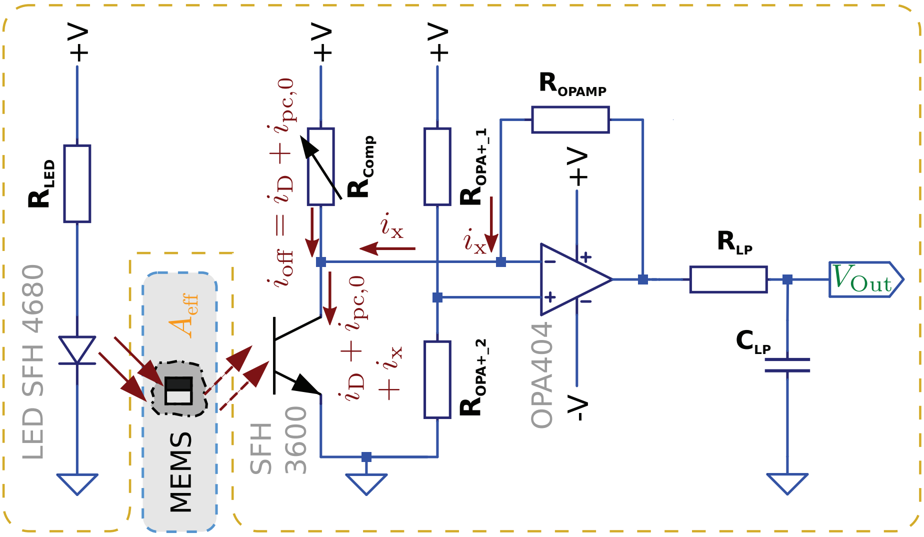

Figure 2.8: Circuit diagram of the optoelectrical components and the evaluation electronics. The continuously powered LED produces light flux whose intensity is modulated by the mechanical part of the MEMS and detected by the phototransistor. i_{D} is the dark current of the phototransistor, i_{x} is the photocurrent generated by differential deflections of the gratings, and $i_{\mathrm{pc},0}$ corresponds to the photocurrent of the unloaded system.[27]

rectangular] apertures which are shifted by a half pitch period to guarantee a linear transfer characteristic. The thereby generated photocurrent i_{off}, originating from the offset light flux [at rest], is compensated [by] the resistor $\mathrm{R}_{\mathrm{Comp}}$.

For the experiments, the circuit was built using the low-noise, high-bandwidth, and low-bias current amplifier OPA404 (BurrBrown), an SMD LED type Osram SFH4680, and a phototransistor of type Osram SFH3600. The circuit was supplied by ±12 V and a bias voltage of 4 V was imposed on the phototransistor. The conversion gain was set via R_{OPAMP} to $10\,\mathrm{k}\Omega$ and R_{Comp} was realized with a ten turn potentiometer. In principle, the whole circuit could be manufactured as a fully integrated circuit with a low electrical noise level and with the LED as only external device. Using PIN diodes, the electrical noise of the photodetector can be reduced resulting in a further enhanced displacement resolution."[27]

"The LED is operated with a [serial] resistor $R_{\mathrm{LED}} = 660\,\Omega$, [thus] setting the current with [an] SFH4680 to 16 mA.

Typically, the electronical subsystem exhibits a low pass behavior whose cut off frequency f_C is [limited] by the amplifier's gain-bandwidth product. Hence, H_elec is [constant] for measurements [at] frequencies below f_c

$$H_\mathrm{elec} = R_\mathrm{OPAMP} \cdot S \cdot I_\mathrm{e} \quad . \tag{2.17}$$

[This will be, from now on, referred to as the] gain of the optoelectrical subsystem g_elec. Therefore, as long as the gain-bandwidth product of the operational amplifier is not reached the generated photocurrent is linearly transformed to the output voltage V_Out [by Eq. 2.17]. The gain-bandwidth product of the amplifier [of] the current voltage [to] converter (OPA404) is 6.4 MHz. The sensor was operated at frequencies up to 5 kHz with an amplification factor of 10 000 V/A which is set by R_OPAMP. [Considering] the phototransistor [as a] capacitor at the input of the operational amplifier, the [evaluation] circuit acts as a differentiator [resulting in an extraordinarily increased] gain-bandwidth product [$f_\mathrm{c} \cdot g_\mathrm{elec}$ and a constant magnitude curve up to more than 20 kHz]."[41] A first order RC-lowpass was placed following the TIA output in order to suppress disturbances at high frequencies.

Characterization of the Evaluation Circuitry

The transfer function of the TIA was characterized by means of a network analyzer. The characterization was done with an Agilent E5061B Network Analyzer while replacing the phototransistor with a resistor R_PhTr of $75\,\mathrm{k\Omega}$ at the inverting input of the TIA. This resistance was chosen to fit the collector emitter resistance of the phototransistor of $77.5\,\mathrm{k\Omega}$ when it is operated at collector emitter voltages above $0.5\,\mathrm{V}$. The non-inverting input of the operational amplifier was connected to ground introducing a virtual ground at the inverting input. This yields a current i when applying the output voltage of the network analyzer V_In to the free port of R_PhTr. The magnitude of the transfer characteristic between V_In and V_Out at frequencies far below the corner frequency of the operational amplifier was calculated to be $20 \cdot \log_{10}(V_\mathrm{Out}/V_\mathrm{In}) = 20 \cdot \log_{10}(R_\mathrm{OPAMP}/R_\mathrm{PhTr}) = -17.5\,\mathrm{dB}$ which is consistent with the measured values in Fig. 2.9. The transfer characteristic equivalent to that of the TIA between the current i and V_Out results accordingly in an amplification by $80\,\mathrm{dB\Omega}$ or $10\,\mathrm{k\Omega}$. Figure 2.9 depicts two bode plots of the adapted evaluation circuit with and without the output low pass filter. The TIA itself exhibits a 3 dB cutoff frequency of 160 kHz or 123 kHz with a low pass filter in series. Therefore, the prerequisite for distortion free measurement of the MEMS characteristics, i.e., $f_\mathrm{c} \gg f_0$ is fulfilled.

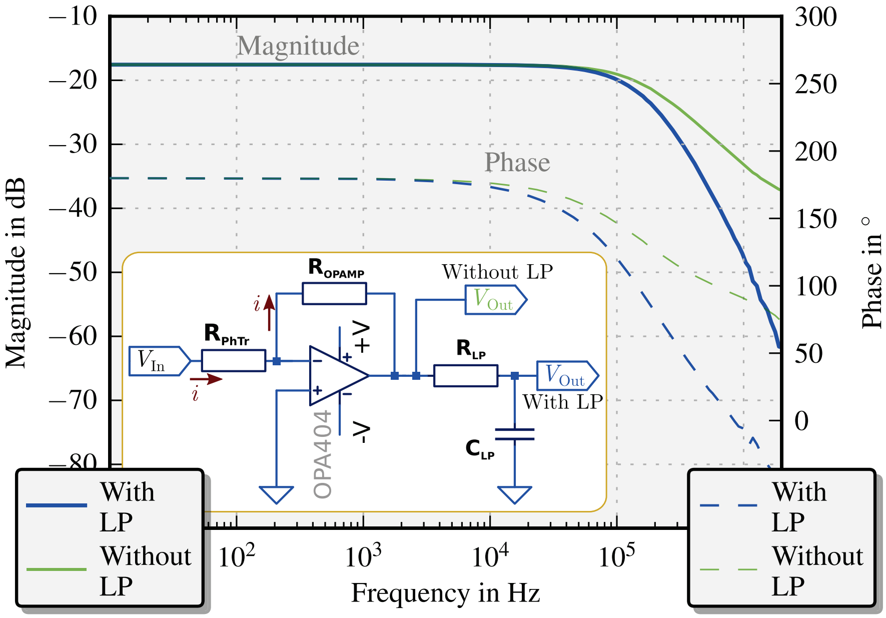

Figure 2.9: Bode plots of the adapted transimpedance amplifier circuit with and without the low pass at the output. The corresponding circuit diagram can be seen in the inset. The TIA itself exhibits a 3 dB cutoff frequency of 160 kHz. With the lowpass the bandwidth is smaller and $f_c = 123\,\text{kHz}$.

2.3 Noise Sources

The inherent and intrinsic noise of the MOEMS can be estimated by summing up the noise originating from the mechanical parts of the MEMS sensor and that of the opto-electronics [40]. Both contributions can be compared and added after transferring them into a noise equivalent deflection NED

$$NED = \sqrt{NED_{\mathrm{M}}^2 + NED_{\mathrm{E}}^2} \quad . \tag{2.18}$$

Here, NED_{M} corresponds to the mechanical noise and NED_{E} is the noise equivalent deflection caused by the opto-electronics. The mechanical as well as the opto-electronic contributions will be discussed in detail in the following sections.

2.3.1 Mechanical Noise

One force acting on the MEMS mass is generated by the thermal motion of the surrounding gas particles and gives (spectral density of the fluctuating force [11, 42], in $\mathrm{N}/\sqrt{\mathrm{Hz}}$)

$$F_\mathrm{n} = \sqrt{4\,k_\mathrm{B}\,T\,d}, \tag{2.19}$$

where k_B is the Boltzmann-constant, T the absolute temperature and d in $\mathrm{kg/s}$ the damping coefficient. The damping coefficient can be expressed by

$$d = D\,2\,m\,\omega_0 \tag{2.20}$$

using the damping ratio D or the quality factor Q which are defined by

$$Q = \frac{\omega_0 m}{d} = \frac{1}{2\,D} \quad . \tag{2.21}$$

Therefore, Eq. 2.19 can be rewritten with Eq. 2.20 as

$$F_\mathrm{n} = \sqrt{4\,k_\mathrm{B}\,T\,D\,2\,\omega_0\,m} \quad . \tag{2.22}$$

This force acts directly on the mass of the system described by Eq. 2.10 resulting in a Brownian motion of the mass and the Brownian noise transfer function

$$H_\mathrm{n}(s) = \frac{X_\mathrm{n}(s)}{F_\mathrm{n}} = -\frac{1}{m\,s^2 + d\,s + c} \quad . \tag{2.23}$$

where X_n is the Brownian motion deflection. Solving for the magnitude response of Eq. 2.23 results in

$$|H_\mathrm{n}(\omega)| = \frac{1}{\sqrt{d^2\omega^2 + \left(m\omega^2 - m\omega_0^2\right)^2}} \quad . \tag{2.24}$$

Generally, this transfer function which is equivalent to a second order low pass, describes the displacement response to forces such as, e.g., electrostatic forces acting directly on the spring suspended mass. Equation 2.24 can be simplified for $\omega \ll \omega_0$ to

$$|H_\mathrm{n}(\omega)| \propto \frac{1}{m\,\omega_0^2} = \frac{1}{c} \quad . \tag{2.25}$$

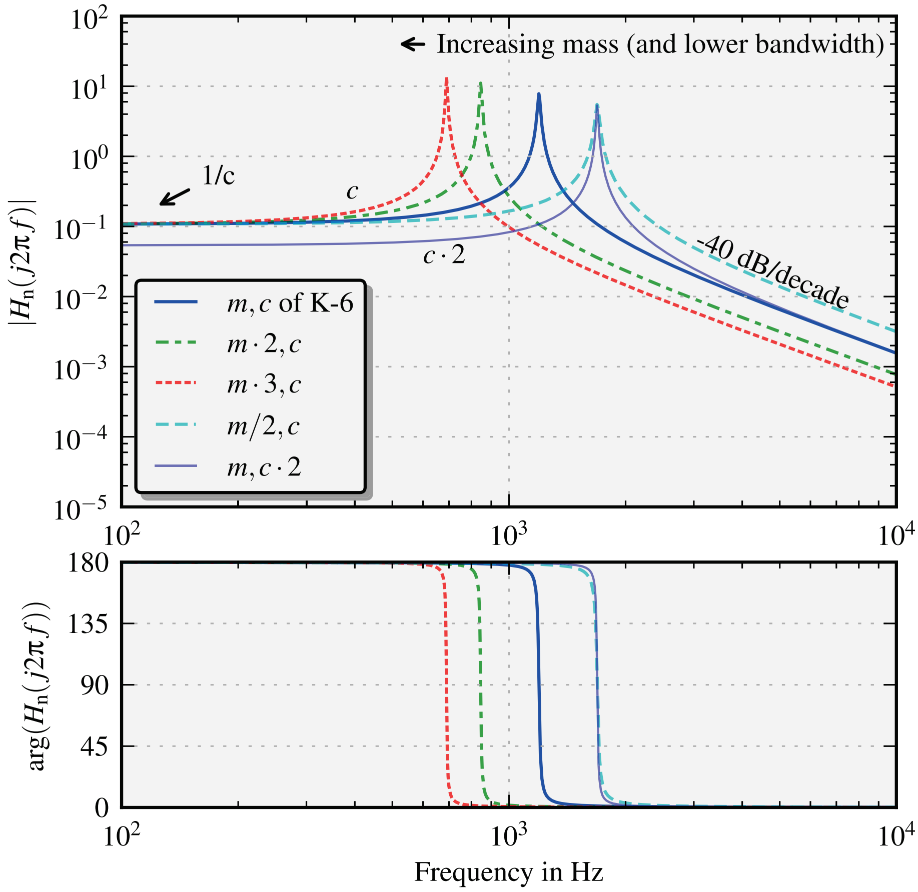

Figure 2.10: Examples of ideal second order low-pass models for the Brownian (motion) force acting on the mass. The bandwidth of the systems is lower for lower resonance frequencies. At lower frequencies, the four systems with the same stiffness c reveal the same magnitude of $1/c = 1/9.3\,\mathrm{N/m} = 0.107\,\mathrm{m/N}$. The initial parameter for m and c are equal to the one of prototype K-6 (see Sec. 3.4).

Hence, the magnitude below the natural frequency is inversely proportional to the stiffness. Figure 2.10 depicts the magnitude response for the Brownian motion force for a typical MEMS system and four equivalent systems with different masses and stiffness.

For quasi static deflection or $\omega \ll \omega_0$, Eq. 2.23 can be transformed together with Eq. 2.25 into the intrinsic noise equivalent deflection originating from 'mechanical' thermal noise (spectral density of the fluctuating deflection)

$$NED_{\mathrm{Br}} = |X_{\mathrm{n}}(\omega)| = F_{\mathrm{n}} \cdot |H_{\mathrm{n}}(\omega)| = \frac{F_{\mathrm{n}}}{c} \quad (\mathrm{m}/\sqrt{\mathrm{Hz}}) \tag{2.26}$$

which can also be rewritten as

$$NED_{\mathrm{M}} = NED_{\mathrm{Br}} = X_{\mathrm{n}} = \frac{\sqrt{8\,k_{\mathrm{B}}\,T\,d}}{c} \quad . \tag{2.27}$$

The diagram in Fig. 2.11 depictes this relationship for constant d. Lowering x_{n} for a system with given ω_0 results in the change of both parameters m and c according to the inserted curve with constant resonance frequency. The mechanical thermal noise can also be reduced by lowering d. On the one hand, this can be achieved by changing the design, i.e., by reducing the amount of front and top faces of the MEMS-mass which mainly induce damping in the form of shear waves [43]. On the other hand, the damping ratio can be reduced by lowering the pressure inside the package of the MEMS. To guarantee a sufficiently low pressure inside a MEMS package over years, however, imposes enormous technological challenges which should therefore be avoided.

In contrast, to the NED_{Br} the signal response of a system excited at the foundation is

$$|X_{\mathrm{d}}(\omega)| = |H_{\mathrm{v}}(\omega)|\,|X_{\mathrm{f}}| \tag{2.28}$$

and the response of an acceleration, A_{m}, of the mass is

$$|X_{\mathrm{d}}(\omega)| = |H_{\mathrm{a}}(\omega)|\,|A_{\mathrm{m}}| \quad . \tag{2.29}$$

The resulting signal to noise ratios versus frequency results in

$$SNR_{\mathrm{mech,v}}(\omega) = \left|\frac{X_{\mathrm{d}}(\omega)}{X_{\mathrm{n}}(\omega)}\right|^2 = \left|\frac{H_{\mathrm{v}}(\omega)\,X_{\mathrm{f}}(\omega)}{H_{\mathrm{n}}(\omega)\,F_n}\right|^2 = \frac{m^2\omega^4|X_{\mathrm{f}}|^2}{4\,d\,k_{\mathrm{B}}\,T} \tag{2.30}$$

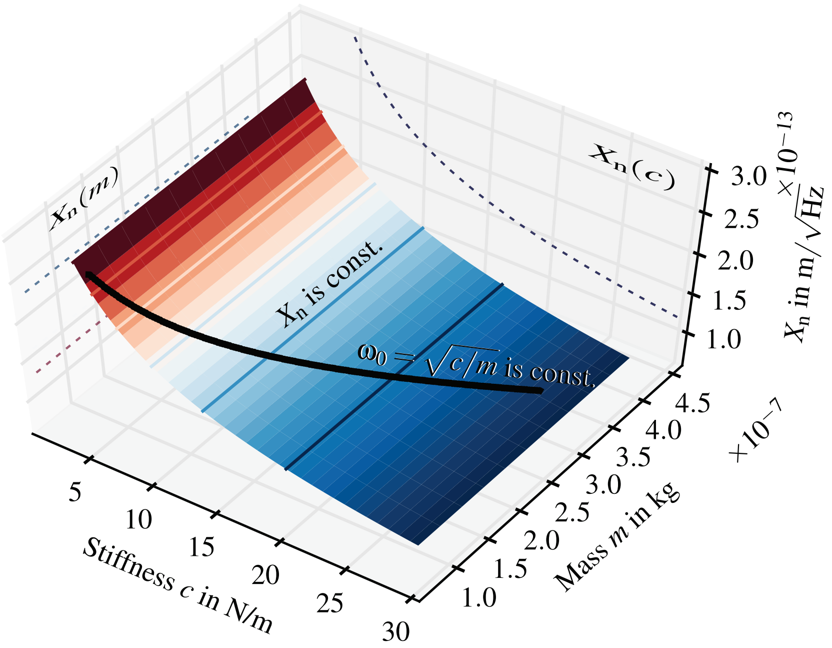

Figure 2.11: Deflection of the suspended mass by Brownian motion with respect to variations of the mass and the stiffness of the system with a constant damping factor. The line in black represents the deflection $X_\mathrm{n}(c, m)$ for constant natural frequency ω_0. The contour illustrates levels of constant X_n. The curves of X_n in dependency of c and m are illustrated on the box faces of the axis.

$$SNR_\mathrm{mech,a}(\omega) = \left|\frac{X_\mathrm{d}(\omega)}{X_\mathrm{n}(\omega)}\right|^2 = \left|\frac{H_\mathrm{a}(\omega)\,A_m(\omega)}{H_\mathrm{n}(\omega)\,F_n}\right|^2 = \frac{m^2|A_\mathrm{m}|^2}{4\,d\,k_\mathrm{B}\,T} \qquad (2.31)$$

where $\omega^2 X_\mathrm{f}$ is equal to the magnitude of the input acceleration at the foundation which is equivalent to $-A_\mathrm{m}$. Both signal to noise ratios versus frequency are depicted in Fig. 2.12.

Summary. The inertial mass influences several properties of accelerometers and vibration sensors. The increase of the inertial mass of an accelerometer improves the sensitivity but reduces the bandwidth. In case of a vibration sensor additional inertial mass increases the bandwidth of the sensor (see Eq. 2.9). For the vibration sensor an increased inertial mass lowers the bandwidth of Brownian noise impact. For the acceleration sensor this bandwidth reduction corresponds to the accelerometer bandwidth reduction.

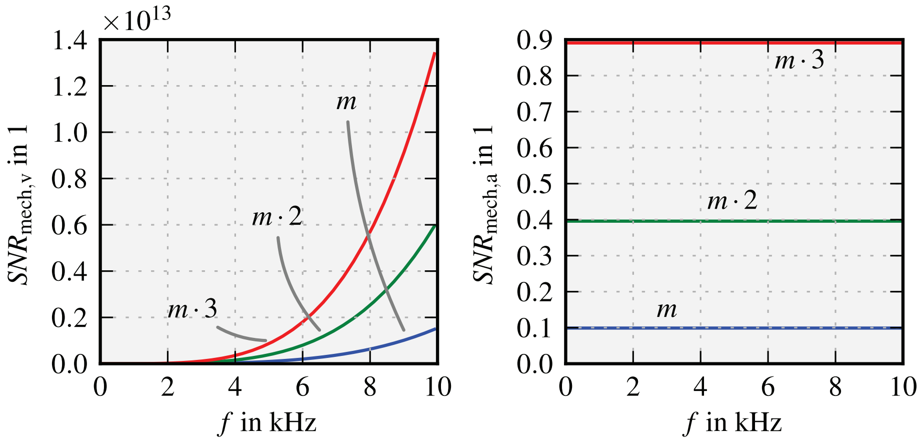

Figure 2.12: Dependency of $SNR_{\mathrm{mech,v}}$ and $SNR_{\mathrm{mech,a}}$on m versus the frequency. Three different systems were modeled by varying the mass of a system. Considering thermal noise as the main noise source, the signal to noise ratio increases with ω^4 for a vibration sensor while it is constant for an accelerometer.

A fundamental understanding of the damping of the MEMS part is required to minimize Brownian noise, avoiding the need of hermetic sealing to reduce the pressure inside the MEMS-package and to directly lower the damping.

2.3.2 Noise Consideration of Opto-Electronics

“The collector current of a phototransistor

$$i_{\mathrm{pc},0} = (h_{\mathrm{FE}} + 1)\,\eta_{\mathrm{PTD}}(\nu)\,F(\nu)\,A_{\mathrm{b}} \tag{2.32}$$

linearly rises with [the] light flux $F(\nu)A_{\mathrm{b}}$ arriving at the photodetector [44, 45]. In the above equation [is] h_{FE} the DC current gain, η_{PTD} is the quantum efficiency of electron-hole pair generation in the base of the phototransistor, ν is the frequency of the incident light, $F(\nu)$ is the photon flux rate per area and A_{b} is the area of the base region exposed to radiation. Due to the function principle of the intensity modulation [of the] MOEMS the photon flux $F(\nu)$ is proportional to the transparent area A_{eff} of the apertures.

The squared fluctuation of the phototransistor collector current can be written as

$$\overline{i_0^2} = 2\,q\,i_{\mathrm{pc},0}\left[1 + \frac{2\,h_{\mathrm{fe}}^2/h_{\mathrm{FE}}}{1+(f/f_\beta)^2}\right]\Delta f \quad , \tag{2.33}$$

where q denotes the electron charge, h_{fe} is the incremental current gain of the phototransistor, and Δf is the bandwidth of the opto-electronics [44]. Considering only frequencies f well below the phototransistors cutoff frequency f_β and approximate $h_{\mathrm{FE}} \simeq h_{\mathrm{fe}}$ the collector square temporal average value can be expressed as

$$\overline{i_0^2} \simeq 4\,q\,i_{\mathrm{pc},0} h_{\mathrm{fe}} \Delta f \quad . \tag{2.34}$$

Design Impact of Noise Level Estimation

The photocurrent variation of a [photodetector] due to displacement of the apertures can be written as $i_x = J_{\lambda\mathrm{D}}\,x_d\,l_{\mathrm{e}}$, where l_{e} is the edge length of a all apertures (see Fig. 3.43), x_{d} is the displacement of the grating and $J_{\lambda\mathrm{D}}$ is the average photocurrent density of the photodiode [46]. Taking into account that the power spectral density S_{i} of the photocurrent noise is also given by

$$S_{\mathrm{i}} = 4qJ_{\lambda\mathrm{D}}A_{\mathrm{eff}} \quad , \tag{2.35}$$

where q is the electron charge and $A_{\mathrm{eff}} = W_0 l_{\mathrm{e}}$ the open area at rest position, the noise equivalent displacement spectral density can be expressed as

$$S_{\mathrm{x}} = \left|\frac{x_{\mathrm{d}}}{i_x}\right|^2 S_{\mathrm{i}} = 4q\frac{W_0}{J_{\lambda\mathrm{D}} l_{\mathrm{e}}} \propto \frac{A_{\mathrm{eff}}}{l_{\mathrm{e}}^2} \quad . \tag{2.36}$$

In the case of prevailing $\overline{i_0^2}$ and half opened aperture at rest position, the photocurrent and the related noise power are given by $i_{\mathrm{pc},0} = \eta\,J_0\,l_{\mathrm{e}}\,W_0$. Here J_0 denotes the optical power density at the aperture array and η the related conversion. A small displacement x_{d} results in a photocurrent variation $i_x = x_{\mathrm{d}}\,l_{\mathrm{e}}\,\eta\,J_0 = x_{\mathrm{d}}\,i_{\mathrm{pc},0}/W_0$ and the corresponding [ideal] signal-to-noise ratio

$$SNR_{\mathrm{i}} = \frac{|i_x|^2}{|i_0|^2} = |x_{\mathrm{d}}|^2\,\frac{\eta\,J_0 l_{\mathrm{e}}}{W_0}\,\frac{1}{4q\,h_{\mathrm{fe}}\Delta f} = \left|\frac{x_{\mathrm{d}}}{W_0}\right|^2 \frac{i_{\mathrm{pc},0}}{4q\,h_{\mathrm{fe}}\Delta f} \,. \tag{2.37}$$

[This suggests] the use of high aspect ratios l_{e}/W_0 [in order to achieve] high displacement resolutions. The increase of the signal-to-noise ratio with $i_{\mathrm{pc},0}$ can be seen in Fig. 3.45 where S_V is proportional to $\overline{i_0^2}$."[47]

At $SNR_\mathrm{i} = 1$ the noise equivalent displacement resolution results from Eq. 2.37 to

$$NED_E = x_{\mathrm{d},0} = W_0 \sqrt{\frac{4\,q\,h_\mathrm{fe}\Delta f}{i_{\mathrm{pc},0}}} = \sqrt{\frac{W_0}{l_\mathrm{e}} \frac{4\,q\,h_\mathrm{fe}\Delta f}{\eta J_0}} \quad . \tag{2.38}$$

Equation 2.38 reveals that the noise equivalent displacement of the opto-electrical system is proportional to the square-root of the aspect ratio of the aperture W_0/l_e. Corresponding measurements are discussed in Sec. 3.5.1.

Dynamic Range

By means of the maximum useful deflection $2W_0$ (see Fig. 2.4) with respect to the rest position, the dynamic range can be expressed by transforming Eq. 2.38 as

$$\begin{aligned} DR &= 20\,\log_{10}\left(\frac{2W_0}{x_{\mathrm{d},0}}\right) = 20\,\log_{10}\left(2\sqrt{\frac{i_{\mathrm{pc},0}}{4\,q\,h_\mathrm{fe}\,\Delta f}}\right) && (2.39)\\ &= 20\,\log_{10}\left(2\sqrt{l_\mathrm{e} W_0 \frac{\eta J_0}{4\,q\,h_\mathrm{fe}\Delta f}}\right) \quad . && (2.40)\end{aligned}$$

The corresponding results are discussed in Sec. 3.4.1.

Summary

The dependency of NED_E on the square-root of the aspect ratio of the aperture W_0/l_e in Eq. 2.38 reveals that with the presented MOEMS it is not possible to achieve a high displacement resolution over a wide range of displacements even if it is suggested by the dynamic range in Eq. 2.39.

2.4 Temperature Dependency

The temperature dependencies of the opto-electrical components of the MOEMS dominate the overall sensor dependency on temperature. The temperature dependency can be divided into three major parts.

First, the darkcurrent of the phototransistor shows a logarithmic temperature dependency. The darkcurrent can not be compensated for and it is therefore limiting the displacement resolution of the sensor.

Second, the LED has a linear temperature dependent radiant intensity factor of -0.5%/K. Nevertheless, this dependency can easily be overcome by e.g., adjusting the current through the LED.

Third, the operational amplifier OPA404 reveals temperature dependent bias and offset currents which shift the sensor output offset level. They can easily be compensated for with a feedback loop even if their dependency is logarithmic.

The influence of the temperature on mechanical properties such as the Young's modulus is in the range of several ppm [48] and negligible compared to the above listed parts.

Chapter 3

Prototypes

This chapter describes the design and fabrication process of the sensors developed throughout the thesis. To determine the resolution limit and to analyze the linearity of the sensor, different types of MEMS were designed and fabricated. All of these prototypes can be classified into two groups, the vibration sensors and the combdrive-actuated sensors. The first prototype of a vibration sensor was fabricated to ensure the applicability of the transduction principle. Corresponding results are discussed in [49, 50]. Recent results for this sensor type concern its noise equivalent deflection (NED). On the contrary, MOEMS incorporating a comb-drive enable the determination of aperture related design criteria, such as the optimum side length of a rectangular opening.

The first part of this chapter describes essential design aspects for the MOEMS sensors. Afterwards, the MEMS fabrication and its limitations are discussed and the experimental set-up is presented together with the corresponding results. Finally, the layout of the combdrive-structure prototypes is discussed in more detail.

Parts of this chapter were earlier discussed in [51, 47, 52] and were adopted to fit into the present context. These parts are set under quotation marks.

3.1 Sensor Design

The essential parts of the MOEMS sensor (see chapter 2) can basically be grouped into the MEMS and the optoelectronics. The design of the MEMS part depends on the spectral region covered by the optoelectronics and therefore, the consequences on the essential parameter of the mechanical parts such as mass and wavelength range are discussed subsequently.

3.1.1 Optoelectronics

MEMS related criteria. “When designing accelerometers or vibration sensors, a main goal is the improvement of the mechanical signal to noise ratio which can be achieved by increasing the inertial mass (compare Eq. 2.30 and 2.31). Two options are directly available for increasing the mass in case of a micro-opto-electro-mechanical intensity modulator (MOEMS), if the perforated mass is fabricated into a silicon layer of a certain height. A larger mass can be achieved firstly by, increasing the chip area of the mass, and secondly, by lowering the size and number of openings. The enlargement of the chip area is directly proportional to the sensitivity, but also leads to higher sensor costs. By transferring the openings for intensity modulation into a metal layer on top of an unperforated inertial mass and by choosing a range of wavelengths in which silicon is transparent, the mass can reach its maximum value for a certain chip area and height.”[52] An illustration of both described set-ups can be seen in Fig. 3.1.

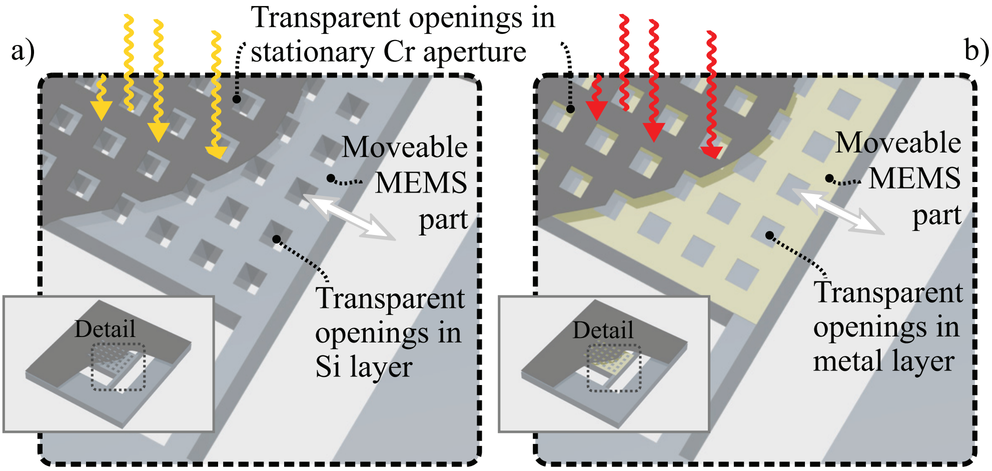

Figure 3.1: Schematic of the micro-mechanical set-up of the sensor a) for visible light with openings etched into silicon and b) for infrared light with a wavelength above 1.1 µm and an unperforated mass with a metal aperture on top.[52]

”One benefit of this principle is that the MEMS fabrication becomes easier. The creation of fine metal structures using lift-off is preferable compared to etching narrow openings into a thick silicon layer. Hence, the metal layer can be processed with a higher precision than its etched counterpart.”[52]

Basics of Optoelectronics. Due to the applied transmissive transduction principle, it is necessary to discuss the spectral properties of silicon. For the discussed sensor application, single-crystal silicon is used. Since silicon is a semiconductor, it exhibits a band gap between the top of the valence band and the bottom of the conduction band (see Fig. 3.2).

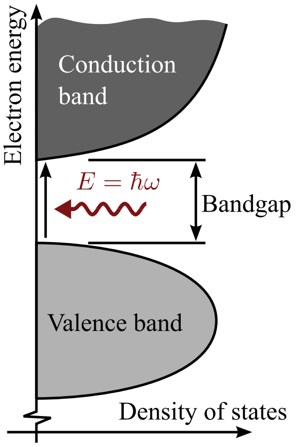

Figure 3.2: Simplified band structure of a semiconductor such as silicon [53]. To lift an electron from valence to conduction band across the indirect energy-gap, a certain amount of energy is needed.

An electron jumps from the valence band to a conduction band if it absorbs a specific minimum amount of energy. This energy can be obtained by absorbing a photon, whereas conservation of momentum requires an additional lattice phonon. The cut-off wavelength of mono-crystalline silicon can be calculated from the band gap energy of silicon at 300 K,

$$E = \hbar\omega = 1.11\,\mathrm{eV} \quad , \tag{3.1}$$

where $\hbar = \frac{h}{2\pi}$, h is the Planck-constant and ω is the angular frequency of the incident light. This results in a cut-off frequency of $f = 2.68\,10^{14}\,\mathrm{Hz}$. Giver that the speed of light is $c_\mathrm{l} = 2.99\,10^{8}\,\mathrm{m/s}$, the demanded wavelength can be calculated as

$$\lambda = \frac{c_\mathrm{l}}{f} = 1.11\,\mathrm{\mu m} \qquad . \tag{3.2}$$

The material, therefore, absorbs light for wavelengths shorter than the cut-off wavelength. The absorption edge is not very sharp due to the contribution of the phonon energy. As long as the energy of the incident photon is smaller than E, it is not absorbed and the silicon crystal is transparent. In literature ([54] or [55]), a more detailed definition of the terms used above as well as absorption spectra of silicon at 300 K can be found.

Hence, silicon based opto-electrical receivers can be applied for wavelengths of up to 1.1 µm. Popular opto-electronic components for wavelengths greater than 1.11 µm are build of e.g., InGaAs/InP [56, 57] and are used up to 1.8 µm.

Current components for operating the MOEMS in the near infrared are listed in Tab. 3.1.

	Part-number	Wavelength at peak emission λ_{peak} in nm	Durk-current nA	Total radiated power P_{O} in mW
Transmitter (LED)	SMC1550	1550	/	1[a]
Receiver (PIN diode)	LAPD-1-09-17-TO46	1550	2	/

Table 3.1: Overview of the main parameters of the optoelectronic components of the MOEMS operated in the near infrared region above 1.1 µm. [a]The rated forward current of the LED is 50 mA.

Optoelectronics for the conventional approach. For the MOEMS operating at wavelengths shorter than 1.1 µm, other components than in the near infrared regime are applied and listed in Tab. 3.2. SMD-components internally equipped with reflectors are used for the opto-electrical parts which ensures relatively compact sensors. It is worth mentioning that the difference between optimum wavelength of transmitter and receiver was taken into account and the parts were selected because of their robustness and the availability as SMD incorporating a reflector and therefore offering a larger illumination area at near field.

3.1.2 Design-process of the MEMS

2D design process. In the design, most fabrication procedures for MEMS can be considered as processes controlled by 2D patterns. Fabrication steps like lithography and DRIE (deep reactive ion etch) are directly applying 2D geometries, or map 2D forms into 3D by etching vertical sidewalls into a wafer. The thickness of the device layer, neither influences the functional-

	Part-number	Wavelength at peak emission λ_{peak} in nm	Durk-current nA	Total radiant flux $\Phi_{\mathrm{e\,typ}}$ in mW
Transmitter (LED)	SFH 4680	880	/	23^{b}
Receiver (Phototr.)	SFH 3600	990	1	/

Table 3.2: Overview of the main parameters of the optoelectronic components of the MOEMS with light of a wavelength below 1.1 µm. [b]The forward current of the LED is 100 mA.

ity of vibration sensors, nor the functionality of the combdrive-structures. The seismic mass increases with the thickness of the device layer in the same ratio as the value of the spring constant or the force generated by the combdrives. The benefit of increasing the seismic mass is that the mechanical thermal noise is lowered (compare [42]). All further discussed steps of the process are therefore designed and illustrated with the help of 2D shapes. The geometries are automatically generated in MATLAB in combination with COMSOL-Multiphysics geometry scripting routines and can be basically treated as a sequence of combined or intersected polylines forming shapes such as rectangles. The advantages of scripting the building process are reproducibility, easy design of variants of typical layouts and automated compensation of variations of process specifics such as underetching.

Aperture shapes. In the case of the vibration sensor, different ratios regarding the apertures' width to length have been designed and fabricated to determine the influence of the aperture shape on the sensitivity and the NED. The sensors have been designed with varying masses, different spring shapes and, therefrom, varying chip areas. As a result, the sensors exhibit different resonance frequencies and sensitivities. The designs were implemented without a specific underetching during the fabrication process, but the designs were layouted regarding their resonance frequencies to cover a wide frequency range. An overview of the different aperture designs and spring shapes can be found in Table 3.3 and 3.4.

Table 3.3: Overview of tested chips with different types of aperture. The apertures labeled with “Cr” represent the stationary apertures. Both “Si” and “Au” indicate the movable apertures.

Aperture type on glass	Filled outside			Filled inside	Filled outside
Infrared (IR)	Non-IR				IR
W/l	20/20	10/100	5/100	10/100	10/100
Chip code	E-12	K-6	D-6	M-4, J-18	D-15
Micrographs of exemplary aperture cells 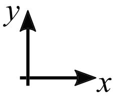	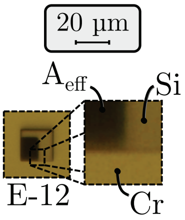			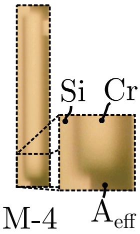	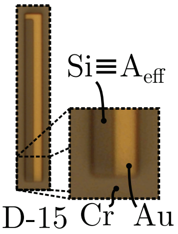

Table 3.4: Applied spring shapes.

Spring shape	Chip code	Micrographs
I	E-12, D-6, K-6, D-15	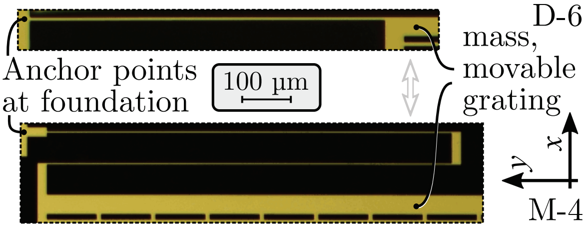
U	M-4, J-18	

Spring shapes. Each movable sensor mass is suspended at its four corners. In general, the folded or U-shaped spring offers the advantage that residual intrinsic stress after production results only in a small deformation of the spring itself, but does not shift the movable grating relative to the designed rest position. In terms of the chip area, an U-shaped spring can be built more compact due to the lower elongation for the same stiffness compared to a straight spring. Straight or I-shaped springs do feature, on the other hand, higher stiffness in z-direction and higher resistance against rotation around the z-axis. Corresponding results with finite element simulation methods (FEM) are discussed in section 3.4.1.

Adjustment of sensitive directions. The adjustment of the sensitivity in a particular direction and the suppression in another can be designed with both the springs and the apertures. For instance, apertures with a narrow, rectangular shape do exhibit a sensitivity inversely proportional to the elongation of the rectangle. The apertures of D-6 exhibit side lengths of $5\,\mu\mathrm{m}$ in x-direction and $100\,\mu\mathrm{m}$ in y-direction resulting in a sensitivity 20 times lower in y-direction than in x-direction. The I-shaped spring of E-12 in Table 3.4 also exhibits one direction of preferred deflection while the spring is stiffer in all other directions. Therefore these deflections are suppressed. In the depicted case of the I-shaped spring the direction of preferred deflection is the x-direction which is approximately 96 times less stiff then in z and approximately 9000 times less stiff than in y-direction. Related results of finite element simulations are discussed in section 3.4.1.

Travel stop. Large deflections of the seismic mass occurring during manual handling of the MEMS devices, can result in a contact between the mass and the supporting silicon frame. Therefore, a travel stop ensuring a very small contact area was added to prevent stiction [58] at the sidewalls due to adhesive forces. The requirements for such a travel stop for the presented sensors are less complex than, for instance, in the case of a capacitive sensor, where the travel stop is required for preventing the capacitive plates to touch each other during operation. For all layouts the contact length (viewed from top) of the travel stop on both sides of the mass was set to 20 µm. The distance between the movable mass and the neighboring sidewalls was chosen so that during sensor operation no contact is possible. If the mass hits the travel stop, the spring force is still greater than the adhesion, ensuring the release of the structure from the travel stop. Hence, for the prototypes, the

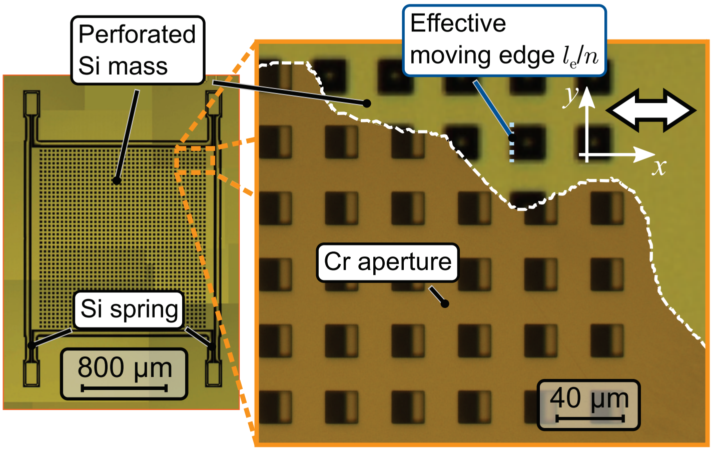

Figure 3.3: The micrographs show the MEMS part of a sensor of type E-12. The geometry of the sensor apertures (20 µm × 20 µm) are enlarged on the right.

travel stop only serves as a protection during transportation, keeping the mass from sticking to the surrounding silicon frame when exposed to multiples of the gravitational acceleration.

Figure 3.3 and 3.4 depict two micrographs of complete sensor designs incorporating four springs of a certain type at each corner of the perforated mass.

3.2 MEMS Fabrication

The fabrication steps for the seismic mass, the springs of the vibration sensor and the combdrive-structure are similar. However, the combdrive-structure requires additional steps to implement the electrostatic actuation. The fabrication of the combdrive-structure is discussed subsequently and the additional steps are highlighted.

Wafer. The MEMS are processed on wafer level. The movable parts were fabricated in the device-layer of an overall 350 µm thick silicon on insulator (SOI) wafer. The excellent mechanical properties of single crystal silicon offer outstanding characteristics of the spring suspended mass system. The device layer of these wafers is a boron doped p-type material and the handle layer is n-type doped with phosphorus. Heavily doped device layer have been chosen to lower the series resistance of the capacitive actuator plates and lead

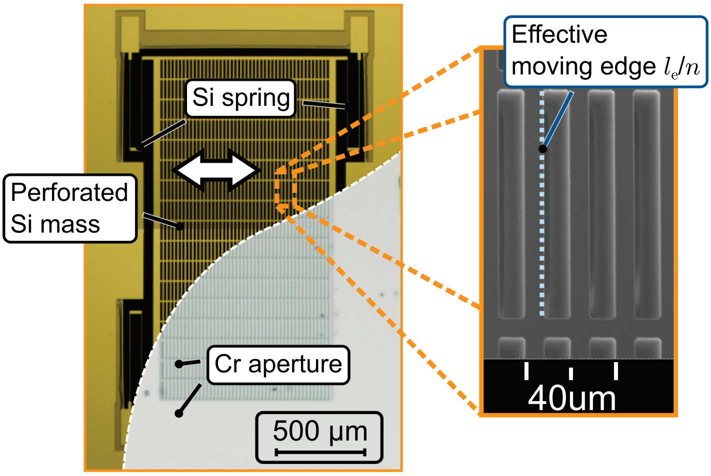

Figure 3.4: Micrographs of a sensor of type J-18. The scanning electron micrograph on the right shows the geometry of the apertures of $10\,\mu\mathrm{m} \times 100\,\mu\mathrm{m}$ in detail.

contacts of the combdrive-structure. For the performance of the MOEMS vibration sensor they are not relevant. The specific resistance for the device layer is $\leq 0,01\,\Omega\mathrm{cm}$ and for the handle layer $1 - 5\,\Omega\mathrm{cm}$. The stationary apertures were established on the surface of a 350 µm thick $\mathrm{Pyrex}^{\circledR}$ glass wafer.

Fabrication steps. The processing of the SOI wafer starts with the removal of the natural silicon-dioxide. The silicon structures are fabricated in the device layer of the SOI wafer using a DRIE process. Electrically insulated regions in the device layer can be fabricated by etching trenches into device layer of a SOI wafer. These subregions ares still mechanically connected via the supporting SiO_2 layer connecting them to the handle wafer. This is especially important for the combdrive-structure where the attracting parts are supplied with different potentials. The SiO_2 intermediate layer functions as etch stop and enables a well defined device thicknesses across the wafer. In principle, the MOEMS vibration sensor could also be etched into a bare silicon wafer, but this requires a sophisticated etching technology.

Figure 3.5 summarizes the individual fabrication steps. The process steps for the SOI wafer are given on the left half of the figure, whereas on the right, the processes for the glass wafer are shown. In the last three steps at the bottom of the figure both wafers were processed together after wafer level bonding. In particular, Fig. 3.5 a) shows:

1. The resist layer for the metal layer is structured with photolithography.
2. Evaporation of Ti-Au onto the structured resist and patterning by lift-off, forming the electrical contacts for the comb-drives and the shape layer of the movable metal gratings.
3. Structuring the resist layer with the geometry of the silicon structure in the device layer by lithography.
4. Fabrication of the main silicon structure into the device layer of the SOI wafer by DRIE.
5. Protection of the device layer by a photoresist.
6. Coating of the surface of the handle wafer with resist and structuring by lithography.
7. Release of the microstructure from the handle layer by DRIE from the backside of the SOI wafer.
8. Finally, etching of the remaining buried oxide (SiO_2) with buffered hydrofluoric acid.

The fabrication of the glass wafer (Fig. 3.5 b) includes:

1. Patterning of the resist on the surface of the glass wafer to form the geometry of the stationary apertures.
2. Evaporating chromium (Cr) onto the surface.
3. Subsequently a silicon nitride (Si_3Ni_4) layer is vapor deposited onto the glass wafer to protect from electrostatic discharge due to the high field between the combdrive components and the Cr-layer on the glass wafer. This step is not necessary for vibration sensors.
4. The SU-8 bonding layer is structured on top of the Si_3Ni_4.
5. Turn over for wafer level bonding.

Fabrication step for the hybrid wafer:

9. Removing of the protection layer on the Si-wafer, wafer cleaning in a deionized water rinse and cleaning the Si-wafer with oxygen plasma.

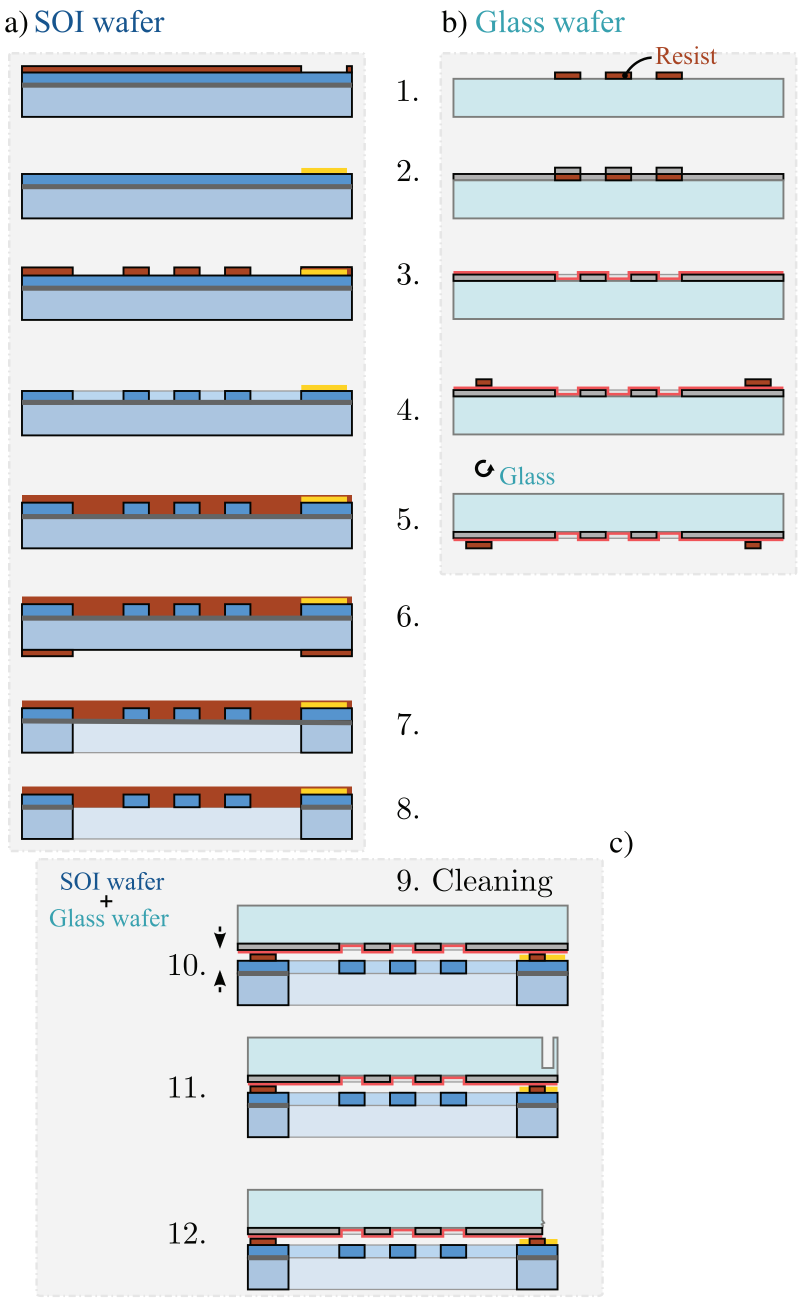

Figure 3.5: Fabrication: a) 1. Lithography for metal layer, 2. metal deposition, 3. lithography for device layer, 4. DRIE etching in device layer, 5. resist for protecting device layer, 6. lithography for handle layer, 7. DRIE through handle layer, 8. SiO_2-etching, b) 1. patterning resist, 2. Cr-layer evaporation, 3. vapor deposition of Si_3Ni_4, 4. lithography of SU-8 bonding layer, 5. wafer turn over, c) 9. cleaning, 10. wafer bonding, 11. dicing and glass structuring, 12. releasing the bonding pads.

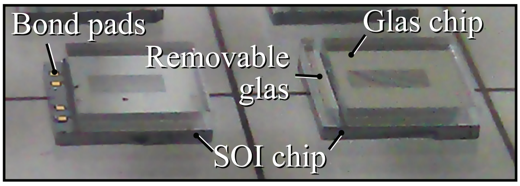

Figure 3.6: Photographs of the fabricated MEMS light modulators with partially removed glass chips.

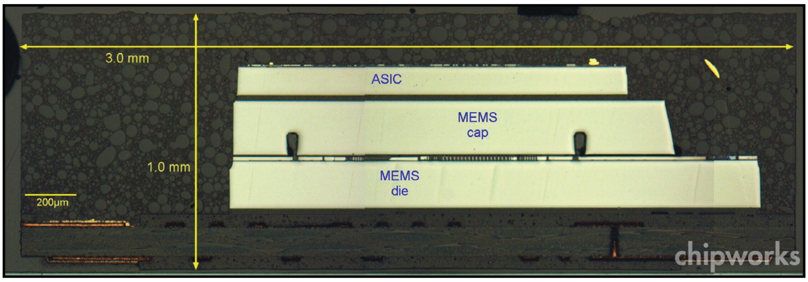

Figure 3.7: Cross section through the package of the three axis accelerometer LIS331DLH of STMicroelectronics done by Chipworks and presented at [59]. The height of silicon layer incorporating the movable parts is approximately 15 µm.

10. The custom wafer level bonding process creates 4 to 13 µm high spacers between the wafers depending on the original height of the SU-8 resist layer. During the chip separation the SU-8 bonding layer serves also as protection frame for the silicon structure holding off cooling water and dust.
11. Afterwards, the wafer is cut into single chips by an automatic wafer saw. Additional notches were which serve as breaking promoter of the covering glass. This step forms regions on the glass chips which can be removed by applying a mechanical force onto the freestanding glass cover. Thus access to bondpads connected to combdrives is established.
12. The bonding pads of the combdrive-structure are thereafter connected by wire bonding them to external voltage and/or current sources.

Two combdrive-actuated MEMS are depicted in Fig. 3.6, illustrating the partially removal of the glass chip to access the bond pads. For mass production of highly robust sensors, one can also use glass fritt bonding instead of SU-8. Glass fritt features higher physical stability but it is also much more challenging to deposit it homogeneously onto the glass wafer, although it is used in high volume production as it is used to seal the MEMS chip with a covering chip as depicted in Fig. 3.7.

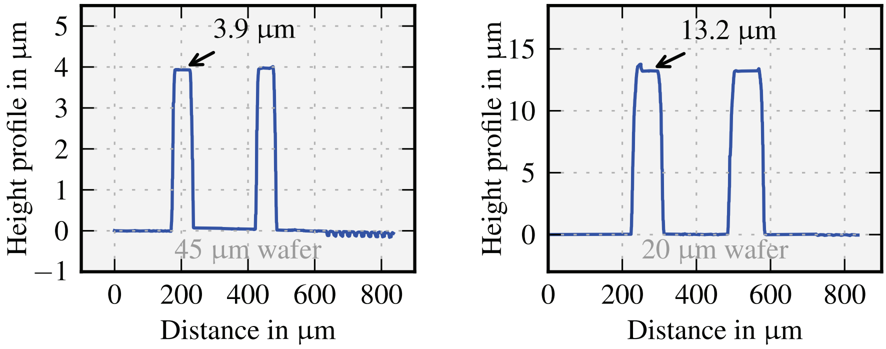

Figure 3.8: Profilometer (Dektak 8 stylus) measurements of the height of the SU-8 spacer of both glass wafers. For the 45 µm wafer set, the SU-8 thickness is 3.9 µm. For the 20 µm wafer set, the SU-8 thickness is 13.2 µm.

The MEMS presented in Sec. 3.4 can be divided into two groups of prototypes. The differences are due to the fabrication process of two wafers sets which differ in thickness of the silicon-device-layer, in the thickness of the SU-8 spacer (see Fig. 3.8) and in the occasional presence of a silicon nitride layer. The two corresponding SOI wafers with device layer thicknesses of 20 µm and 45 µm have been processed with the same layout data. These wafers are subsequently referred as 20 µm and 45 µm wafer. After fabrication, the wafer stack is diced into single chips which were addressed by alpha-numeric chip code, e.g., 'A-1'.

3.2.1 Fabrication Limitations

Wafer Misalignment

During the wafer level bonding of the SOI and the glass wafer, pressure and temperature have to be applied on both wafers. Under these conditions, the SU-8 becomes viscous and bonds to the silicon surface. Simultaneously, however, the mechanical stability of SU-8 against lateral displacement decreases. Hence, the alignment of the glass wafer to the silicon wafer is slightly different for the two processed wafer sets. Therefore, the respective measurement results are not always directly comparable.

The misalignment has an impact on the aperture cross section area at rest. The noise arising from the opto-electrical receiver depends on this according to Eq. 2.34 and Eq. 2.32. Therefore, variations of the sensor noise at rest

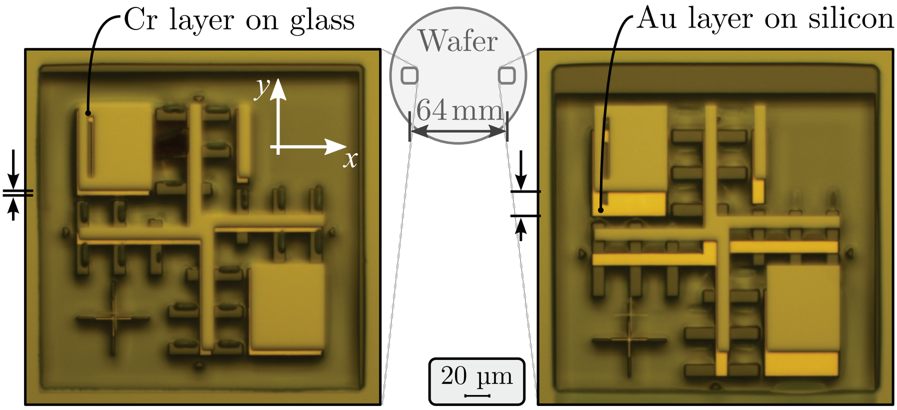

Figure 3.9: Alignment markers on the 20 µm wafer. The markers are are 64 mm apart, symmetrically located on the x-axis of the wafer. The misalignment towards the left side of the wafer is of approximately 2 µm in x and 4 µm in y-direction. Towards the right, the misalignment is of approximately 2 µm in x and 20 µm in y-direction

and furthermore in the noise equivalent displacement can emerge for sensors with identical designs.

The discussed misalignment is not constant over the entire wafer due to a slight rotation (angular misalignment) of the glass wafer during bonding, but it can be approximated for the 45 µm wafer by one micron in the x-direction and 5 µm in the y-direction. The misalignment was determined with the help of alignment markers (Fig. 3.9). On the 20 µm wafer set (Fig. 3.9) it is 2 µm in the x-direction and 4 µm to 19.4 µm in the y-direction, indicating a rotation of the glass wafer by 0.014°. The difficult alignment persists when the second grating would be deposited directly onto the photodetector.

Alternative wafer bonding. The alignment problems can be reduced by an other wafer bonding process or by fabricating the two aperture gratings in one manufacturing step. Anodic bonding, for instance, features higher alignment resolution but does not inherently provide the formation of a spacer layer. Furthermore, high voltages have to be applied during the bonding process resulting in forces onto the electrically insulated parts in the device layer, which can permanently damage the MEMS device.

Aperture fabrication on a single wafer. An exemplary fabrication procedure with only one SOI wafer and no glass wafer is depicted in Fig. 3.10.

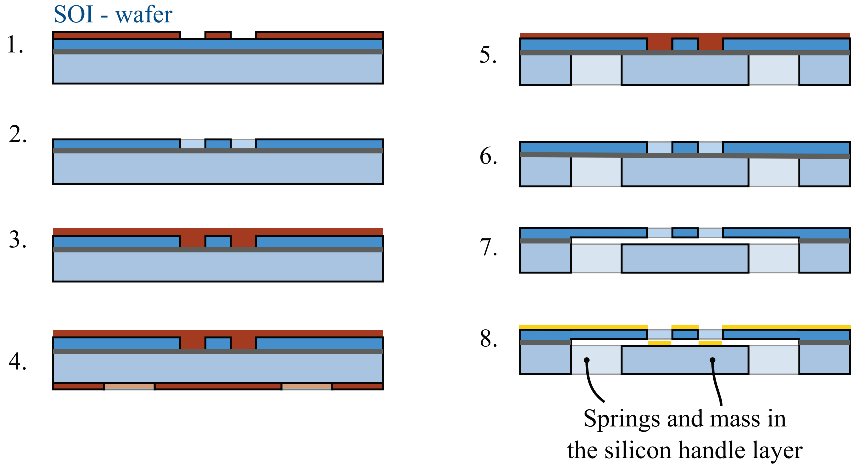

Figure 3.10: Single SOI wafer fabrication: 1. Lithography for the device layer, 2. DRIE in the device layer, 3. resist for protecting the device layer, 4. lithography for the handle layer, 5. DRIE through the handle layer, 6. cleaning, 7. removing SiO_2, 8. deposition of the metal layer.

The aperture shape is etched into a thin device layer of the wafer (Fig. 3.10 2.). Afterwards, the aperture is fabricated by depositing a metal layer onto the device and onto the handle layer (Fig. 3.10 8.). Inside the etched openings, the metal is deposited onto the handle layer incorporating the movable mass. The metal layer on the movable mass has the complementary shape of the metal layer at the top of the device layer. The output signal of such an aperture pair will have twice the frequency of the vibration input. The height of the movable structure inside the handle layer ensures that the z-deflection is negligible. The space due to the removed SiO_2 layer is sufficient to avoid stiction. The main difference compared to the sensor introduced above is that an optical wavelength has to be chosen in which silicon is transparent, i.e., in the infrared spectra.

Aspect ratio dependent etching and notching. The single wafer fabrication avoids etching of the narrow trenches into relatively thick silicon layers. The etching of the DRIE-process depends on the width of the trenches (openings), i.e. wide trenches are etched faster than smaller ones (Fig. 3.11). The process stops at the buried oxide layer. While the narrower trenches are etched, unwanted effects like notching [61] can occur at the bottom of the wider trenches near the SiO_2 (Fig. 3.12). Therefore, the infrared set-up is simpler to fabricate.

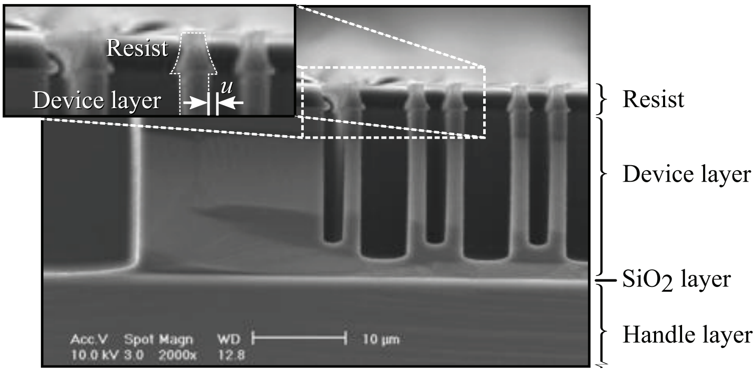

Figure 3.11: Typical scanning electrode microscope (SEM) micrographs of an SOI wafer showing etch trenches with different dimensions illustrating the aspect ratio dependent etching. The zoomed inset shows the underetching u [60].

3.2.2 Underetching

Underetching causes a difference between the original size of the layout in the resist and the etched shape in the silicon layer. Figure 3.11 depicts how underetching (u) occurs during fabrication. Underetching has, mainly, two undesired effects. First, it lowers the spring stiffness and, second, it reduces the mass of the movable structure. For certain aperture shapes fabricated in silicon, underetching always increases the size of the openings and rounds off corners. Figure 3.13 illustrates how underetching modifies a geometry. The geometry is not simply scaled, but all lateral faces are shifted perpendicularly to the resist edge. The wafer level fabrication implies slightly non-uniform process conditions for sensor chips at different locations on the wafer. The chip-location specific size of the underetching was estimated by micrographs of the top and bottom side of the silicon MEMS (compare Fig. 3.14). In contrast to the presented cross-section SEM picture (Fig. 3.11), the determination of u by micrographs is a non-destructive method, but it does not reveal the form of the etch front with respect to the penetration depth. A linear approximation between the value on the top and bottom side is applied to estimate the underetching which is in turn used to estimate the actual mass and stiffness of the MEMS. Additionally, the underetching was also estimated a least squares fit of the measured transfer function data. The corresponding findings are treated in Sec. 3.4 which also includes an overview in Tab. 3.5. The fit involves an analytical model describing dependency of the stiffness and mass on u and yields the magnitude of the transfer characteristics. The

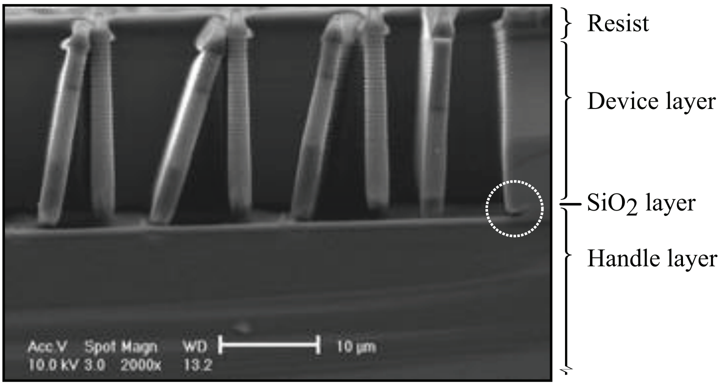

Figure 3.12: Exemplary SEM of an SOI wafer showing notching [60] at the bottom of the trenches.

estimation of the parameters was additionally verified by a FEM computation of the eigenfrequencies of a model with simplified underetched shape (compare Fig. 3.13). The simulation results revealed that the observed deviations from the designed resonance frequencies are mainly due to underetching. The corresponding results are discussed in detail in Sec. 3.4.1.

3.3 Experimental Characterization

Due to the small dimensions of MEMS components, the resulting small deflections of their subparts, and the special assembly of the MOEMS apertures, the characterizations of the sensors is challenging. All measurements of the mechanical and opto-electro-mechanical transfer characteristics were, therefore, done by means of a Polytec Micro System Analyzer MSA400 (MSA). The MSA incorporates a laser doppler vibrometer for precise out-of-plane measurements and a stroboscopic in-plane video analyzer. The mechanical characterization of the MEMS is difficult, especially after bonding the fixed aperture on top of the silicon structures (compare Fig. 3.14). For the characterization of such devices, the MSA can be focused only on one plane of the aperture pair. The evaluation software correlates the acquired images and works best if there is high contrast for the moving edges. Furthermore, for the in-plane mode, minimal deflections of $\geq 10\,\mathrm{nm}$ are required whereas the detection limit for the MOEMS is in the range of a few picometers. For the determination of noise levels of the MOEMS it is, therefore, necessary to measure the deflection of the foundation with picometer accuracy. This is

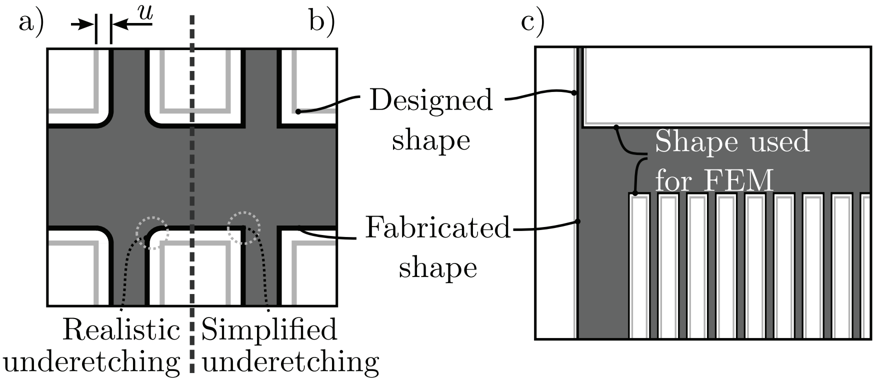

Figure 3.13: Schematic illustration of a) the difference between the realistic and simplified changes of the shape due to underetching and b) of the simplified underetched geometry used for FEM simulation. All etched sidewalls are shifted and roundings formed at corners. The simplified FEM model shapes show perpendicularly shifted sidewalls without roundings. c) A part of the shape of the spring suspended aperture geometry (design D-6).

only achievable by the laser Doppler vibrometer configuration and by an additional lock-in equipment. The following subsections reveal the differences of both measurement set-ups and measurement procedures to characterize the vibration sensors.

3.3.1 Measurement Set-ups

The complete experimental set-up for the characterization of the vibration sensors is depicted in Fig. 3.15. The sensor and the evaluation circuit are located inside a metal housing to avoid stray light and electromagnetic coupling from the surrounding set-up. The metal housing is positioned on a mounting platform bearing the MSA-400 laser-vibrometer sensing head. The granite platform (71 kg [60]) itself is vibration-cushioned to lower ambient mechanical noise [60]. Figure 3.16 shows a block diagram of the measurement equipment involved in the characterization of the sensor transfer function $H_\mathrm{S}(f)$. The complete measurement procedure is controlled by a PC next to the MSA and automated in order to avoid errors and to guarantee reproducibility. The measurement programs and evaluation scripts were created in addition to the MSA software. They are written in the programming language 'Python' using a scientific environment[1] which includes libraries

---

[1] www.pythonxy.com

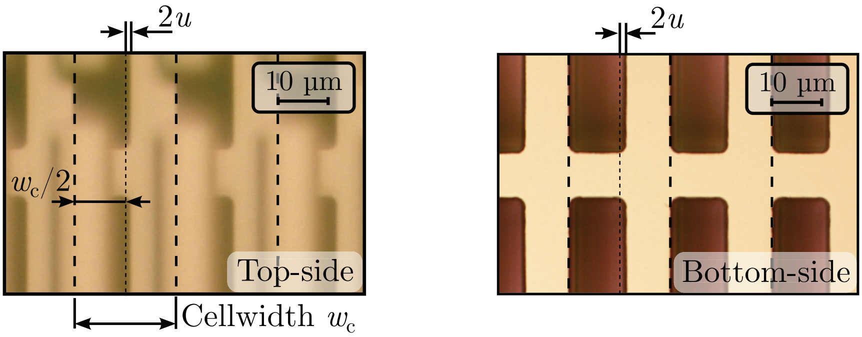

Figure 3.14: Micrographs of the underetching of chip M-4 of the 20 µm wafer. Top-side: $527\,\mathrm{nm} \pm 372\,\mathrm{nm}$, Bottom-side: $640\,\mathrm{nm} \pm 200\,\mathrm{nm}$, linear fit $u_{\mathrm{mic}} = 583\,\mathrm{nm}$. In the micrograph from the top, the Cr-layer is out of focus and thus blurred. This chip also exhibits a large misalignment in y-direction between the glass and the silicon wafer.

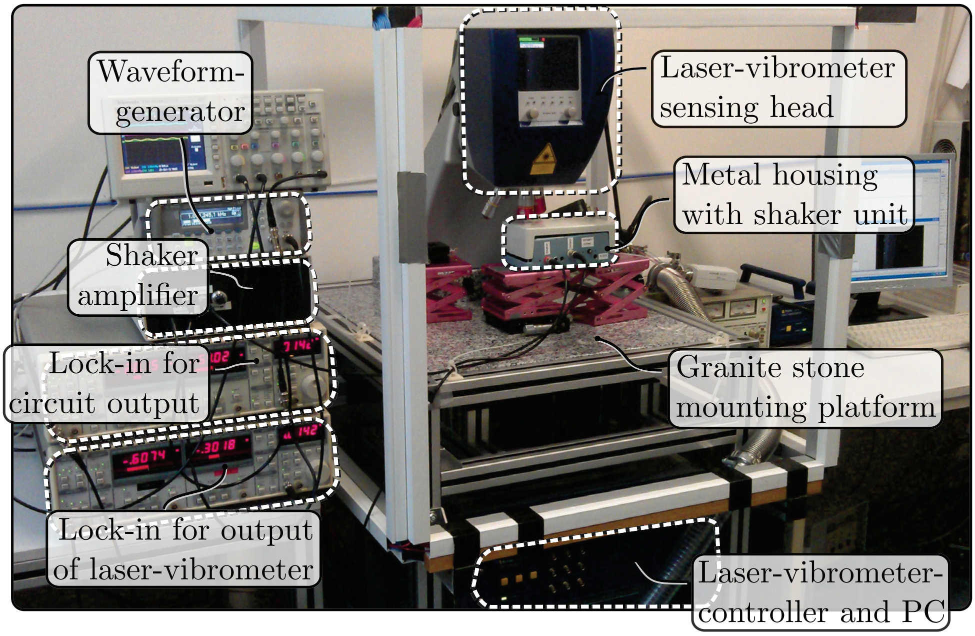

Figure 3.15: The measurement set-up including the waveform-generator, the piezo amplifier and the shaker-unit for the excitation of the vibration sensors as well as the lock-in amplifiers for measuring the deflection equivalent output signal of the MSA and the sensor output signal. The laser-vibrometer and the shaker unit are mounted on a vibration-cushioned granite mounting platform.

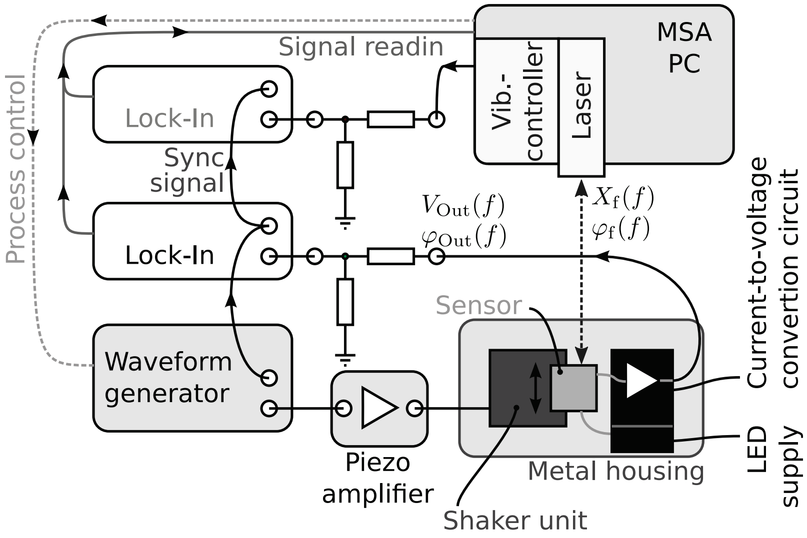

Figure 3.16: Schematic of the measurement set-up including main signal and control paths. The PC controls the measurements with the waveform generator (Agilent 33220A) which generates the input for the piezo amplifier (Physikinstrumente High-Power Piezo Amplifier E-617) and thereafter the shaker unit. The output signals of the laser vibrometer and of the sensor circuit are attenuated in order not to exceed the maximum input signal range (1 V) of the Lock-in amplifiers (Stanford Research SR830 Lock-In amplifiers).

for controlling instruments such as waveform generators and Lock-In amplifiers. ”The sensor devices were characterized by mounting them on a custom-made piezoelectric shaker unit. In this set-up the MEMS device, the LED, and the phototransistor were fixed on separate disks which were stapled and aligned to each other in a specially constructed mounting device (Fig. 3.19).”[51] “The sensor itself was examined in two different arrangements which are depicted in Fig. 3.19 as I and II.”[51] To characterize the mechanical behavior of the MEMS the movement x_{m} and phase information of the inertial mass and the excitation at the foundation x_{f} are determined by the stroboscopic video microscopy mode of the MSA after the LED was removed (Fig. 3.19 I and Fig. 3.17). This in-plane observation is done after rotating the shaker unit by 90°. During the evaluation of the optical readout (Fig. 3.19 II), the laser doppler vibrometer of the MSA measures the footplate excitation x_{f} which serves as input variable for the determination of the sensor transfer characteristics $H_{\mathrm{S}}(f)$. Figure 3.18 shows a section of the

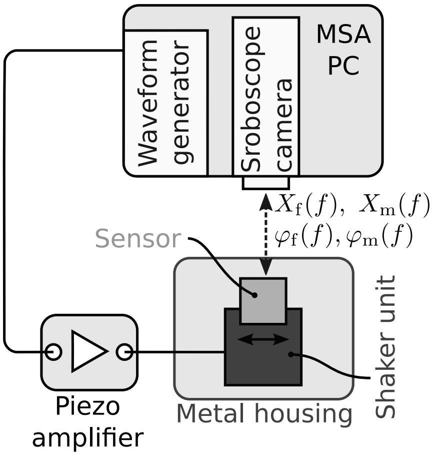

Figure 3.17: Schematic of the measurement set-up for the characterization of the mechanical properties by evaluating video data acquired with the in-plane motion analyzer of the MSA. The shaker unit deflectes the MEMS perpendicular to the optical axis. The piezo amplifier is controlled by the internal waveform generator of the MSA.

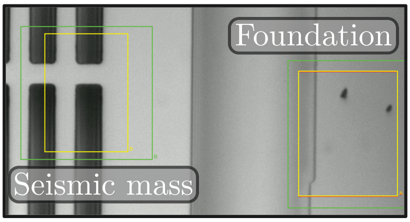

Figure 3.18: The photomicrograph taken with the MSA shows parts of the seismic mass and the foundation of the MEMS chip. The green and red box indicate the areas where the recorded video data is evaluated to determine the in-plane deflection of this region.

mechanical structure and the regions which were used for the evaluation of the movement of the seismic mass and the foundation.

Measurement Procedure. “The shaker unit was designed to excite the tested sensors in a frequency band from 100 Hz to 10 kHz. The footplate displacements determined by the laser vibrometer measurements reveal strong resonances of the shaker unit of more than 40 dB [dynamic] which prevent a straightforward characterization of the MOEMS device (see Fig. 3.21). To [reduce] this effect, a two-step procedure was applied. Based on a first measurement scan, the shaker resonances can be determined and subsequently compensated in the following measurement cycles by properly adjusting the excitation voltage. The remaining [ripples] in the footplate excitation originate from measurement inaccuracies especially at small deflection values near zeros in the shaker transfer characteristic. Compensation of these inaccuracies would in principle be possible by means of a closed-loop amplitude control of the shaker, but this option would have been too complicated to implement. Nevertheless, the residual variations of the shaker amplitude

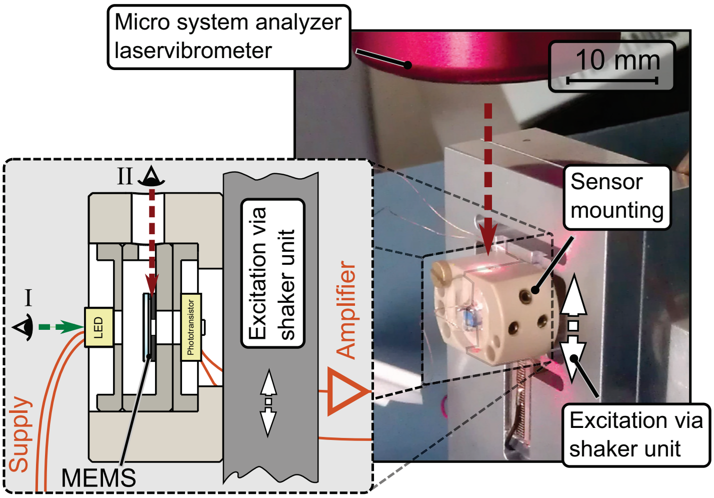

Figure 3.19: Detailed vibration measurement set-up for transducer characterization. In the depicted set-up the optical transmission axis of the transducer is horizontally oriented whereas the vertically aligned laser beam of the Doppler-vibrometer probes the motion of the footplate through a hole in the sample holder. The laser beam of the Doppler-vibrometer (MSA-400) measures the vibration amplitude and phase of the footplate at the edge of the MEMS die. The chip inside the sensor mounting device is examined in two different positions: I to determine the deflection of the inertial mass relative to the chip excitation and II to obtain the movement of the die.[51]

are small enough to avoid input overload of the electronic front-end. In a subsequent spectral scan, the excitation of the footplate as measured by the laser vibrometer and the optoelectronic output were recorded simultaneously. Both the velocity equivalent output signal of the laser vibrometer as well as the amplified sensor output signal V_{Out} were acquired with lock-in amplifiers (Stanford Research Instruments SR830)”[51] yielding magnitude and phase data of the overall sensor transfer function $H_{\mathrm{S}}(f)$ referred to 1 Hz power bandwidth. This correction procedure was repeated for different excitation voltages in order to determine the linearity of the MOEMS regarding input deflection. The lock-in amplifiers were also used to characterize the sensor output noise.

Discussion of Phase Relations. The relative phase of the laser vibrometer signal φ_{f} and the sensor output signal φ_{Out} with respect to the excitation voltage phase φ_{Wg} exhibits a steady negative drift as it can be seen in the phase plot in Fig. 3.23. However, there is no physical mechanism that pro-

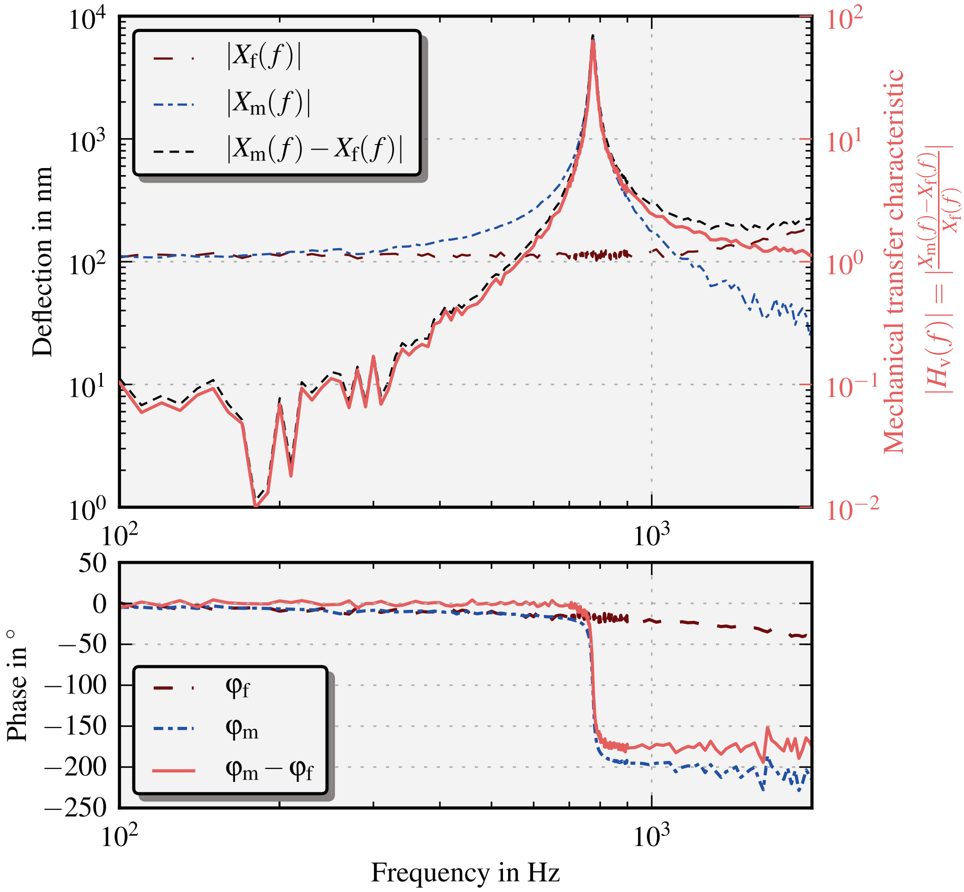

Figure 3.20: The mechanical transfer function of the model discussed in Fig. 2.7.

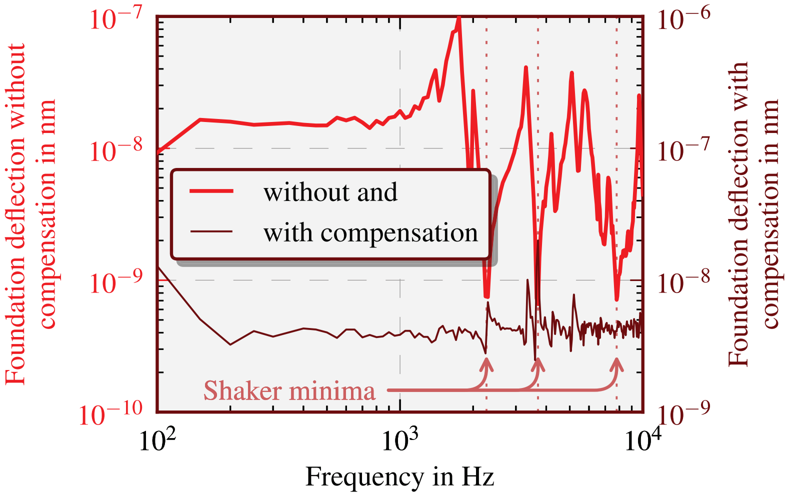

Figure 3.21: Sample foundation excitation x_{f} measured with the laser vibrometer at the sensor foundation. The thick bright red line depicts the deflections generated by the piezo actuator with constant excitation voltage (first run). The thin line represents the result of a partial compensation of the shaker resonances by changing the excitation amplitude according to the inverse amplitude out of the first run. Before the compensation, the deflection amplitude ranges from 0.7 to 100 nm and afterwards from 2 to 20 nm. The main shaker amplitude minima are, in this case, at 2270 Hz, 3700 Hz and 7800 Hz.[51] The mean excitation at the foundation $\tilde{x_{\mathrm{f}}}$ is 4 nm.

vides such a behavior. This phenomenon can be explained with the measurement set-up. Both signals are acquired synchronously with the excitation signal from the waveform generator but experience a phase shift in the piezo amplifier. This phase shift is equal for both phases and is canceled out after calculating the phase information for the sensor by $\varphi_{\mathrm{S}} = \varphi_{\mathrm{Out}} - \varphi_{\mathrm{f}}$. The additional phase shift of the laser vibrometer signal is caused by a constant time delay during the digital filter processing in the analog decoder VD-02 of the OFV-5000 vibrometer controller (see Fig. 3.22). This phase term increases linear with increasing frequency and is subtracted in all computations of the transfer function.

The phase plot reveals also at which frequency the signal to noise ratio of the sensor system approximates unity. In the measurement results shown in Fig. 3.23, the phase relation of the sensor is stable for frequencies above 177 Hz. By computing the standard deviation of a floating sub-array of ten values of the phase data and by determining the frequency at which the standard deviation first becomes higher than 10 degrees, this threshold was as-

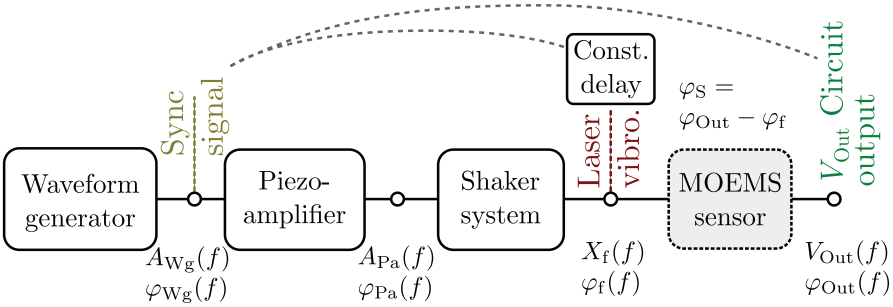

Figure 3.22: Phase relationship between subsystems of the measurement chain. The constant time delay inside the vibrometer controller yields a continuously increasing phase for increasing frequency which is compensated for all measurements by subtracting a linear fitted term.

signed. The thresholds for the sensor phase and the laser phase are indicated in the phase plots by diamonds. An equivalent procedure was applied on the phase of the input deflection at the foundation φ_f in order to determine the frequency threshold f_{NEV} to compute the noise equivalent velocity of the laser vibrometer NEV_L. Below f_{NEV} the phase of the foundation φ_f starts to fluctuate. The evaluation of the *NED* from the sensitivity magnitude characteristic does not reveal the *SNR* that simply (compare Fig. 3.29) because the magnitude curve of the sensitivity can start fluctuating even if the output signal of the sensor is stable. This happens due to $|H_S| = \frac{|V_{Out}(f)|}{|X_f(f)|}$ if the laser signal is fluctuating.

3.4 Results

This section discusses the results obtained by six relevant prototypes. They all differ from each other in the form of the single apertures, the number of apertures in the array, the stiffness and the seismic mass. Table 3.5 provides an condensed overview of the designed as well as the identified parameters. The columns of Table 3.5 are split into five groups: the first two column groups next to the Chip-code include mechanical parameters given by the design or determined by measurements. The next group lists the obtained sensitivity and noise equivalent deflection values which are also related to design parameters like l_e and consumed chip area $A_{c,m}$. In the last two columns the technological parameters, i.e., underetching and wafer thickness, are listed for each sensor. They are the main reasons, why the values of

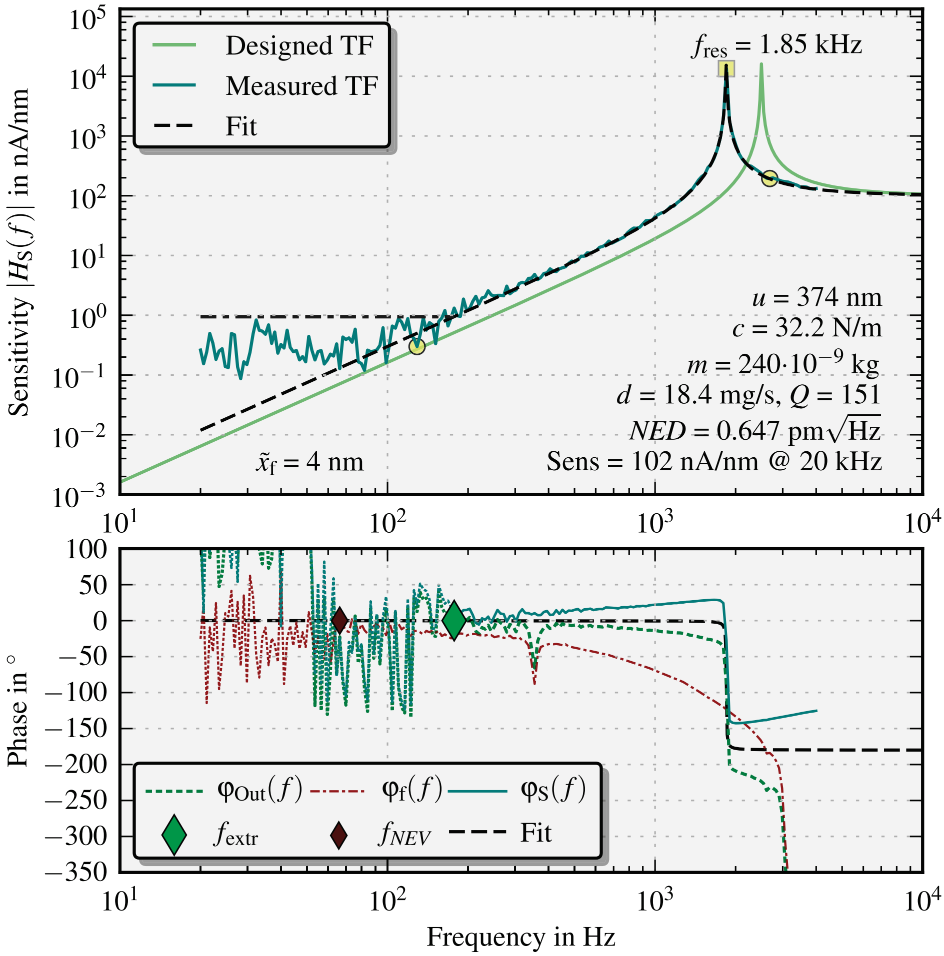

Figure 3.23: Sensor transfer function (TF) of chip E-12 (compare Fig. 3.24). The magnitude plot $|H_S(f)|$ represents the frequency dependent displacement sensitivity of the sensor. All fitted MEMS device parameters are listed inside the plot. The uncertainties of the measured sensor signal's phase and the vibrometer signal's phase reveal the transition region where the SNR approximates unity. For E-12 the transition appears at $f_{\mathrm{extr}} = 177\,\mathrm{Hz}$ resulting in $SNR_{\mathrm{extr}} = 102/0.945 = 108$ at $20\,\mathrm{kHz}$ and a $NED_{\mathrm{extr}} = 35.2\,\mathrm{pm}/\sqrt{\mathrm{Hz}}$. The phase of the laser starts fluctuating below 66.3 Hz resulting in a noise equivalent velocity of $NEV_{\mathrm{L}} = 1.58\,\mathrm{\mu m/s}/\sqrt{\mathrm{Hz}}$. The red and the green diamonds the frequency threshold below which the phases of the output signal and the laser vibrometer, respectively, start to fluctuate. The yellow circles indicate the data portions used for the parameter estimation. The yellow square highlights the resonance peak. The constantly decreasing phase of the sensor output and the laser vibrometer could not be completely compensated. Hence, the resulting sensor phase curve still exhibits an additive contribution which increases with frequency.

Chip-	f_{res}	m	m_{d}	c	d	D	Q	Sens	NED	l_{e}	$A_{\mathrm{c,m}}$	u	t
code		$\cdot 10^{-9}$	$\cdot 10^{-9}$			$\cdot 10^{-3}$							
	kHz	kg	kg	N/m	mg/s	1	1	nA/nm	pm/$\sqrt{\mathrm{Hz}}$	mm	mm²	nm	µm
E-12	1.85	240	245	32.2	18.4	3.3	151	109	0.647	34.4	3.02	374[a]	45
J-18	0.774	45	51	1.07	3.38	7.67	65	357	0.173	78	1.88	711	**20**
D-6	0.856	119[b]	294	3.41	22.3[c]	17.5	29	710[d]	0.231	258	2.94	1135	45
M-4	0.196	148[e]	271	0.23	12.5	34.0	15	415	0.674	266	6.1	674	**20**
K-6	1.51	158	176	14.19	21.8	7.27	68	230	0.348	126	2.94	618	45
D-15	0.879	308[f]	308	9.47	29.3	8.58	58	0.186	2.44	126	2.94	791	45

Table 3.5: Comparison of designed parameters with identified parameters. f_{res} is the resonance frequency, m is the estimated mass, m_{d} is the designed value of the mass, c is the estimated stiffness, d is the identified damping coefficient. u is the underetching, t is the device layer thickness. The design specifies $A_{\mathrm{c,m}}$, the chip area of the mass and l_{e} the effective edge length.

---

[a] The different underetching values of the individual structures are due to their particular position on the wafer and the nonuniformities in the fabrication processes.

[b] The deviation between the designed value of $294 \cdot 10^{-9}$ kg and $119 \cdot 10^{-9}$ kg is due to the large number of openings compared to the other sensors. Additionally, the underetching takes the highest value for this chip compared to the others. The value can also be compared to $107 \cdot 10^{-9}$ kg, the mass extracted from FEM simulations.

[c] The damping of D-6 exhibits the highest value compared to other sensors, which is due to the high number of openings and the thickness of the movable aperture.

[d] The chip D-6 has the highest sensitivity in this table, since M-4 is not completely illuminated due to limitations of the measurement set-up such as a small LED emission area.

[e] The deviation from the ideal value of $271 \cdot 10^{-9}$ kg to $148 \cdot 10^{-9}$ kg is due to the large number of underetched openings. The mass predicted by the FEM simulation of the underetched sensor was $142 \cdot 10^{-9}$ kg.

[f] The mass is approximately twice the amount of K-6 although featuring the same chip size. Due to the lack of etched openings, the mass is almost identical with the designed value.

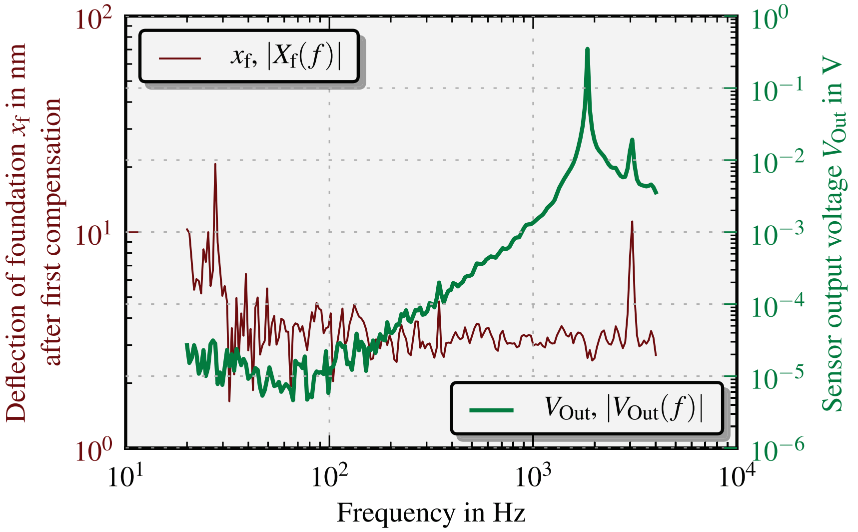

Figure 3.24: Comparison of the chip deflection to the sensor output signal of chip E-12 for the same measurement as presented in Fig. 3.23. After the first magnitude compensation the shaker unit shows an adequate flat transfer function above 50 Hz. The peaks at 350 Hz and 3.1 kHz are present in both curves due to the division $\frac{|V_{\mathrm{Out}}(f)|}{|X_{\mathrm{f}}(f)|}$ in the sensor transfer function. The intensity of the laser is fluctuating below 70 Hz.

the mass and the stiffness obtained by the fit differ from the design.

The first five sensors incorporate the 'conventional' MOEMS sensor approach whereas D-15 is equipped with an infrared opto-electrical readout. The 'conventional' counterpart to D-15 is K-6, exhibiting the same spring design and mass area. All chips were fabricated of a 45 µm thick SOI wafer, except for the two chips J-18 and M-4, which are fabricated of a 20 µm thick device layer. The values for m, c and d were estimated from the measurement data by means of a least squares fit explained subsequently.

3.4.1 Sensor Characteristics

The structures were examined at different deflection amplitudes of the shaker. The amplitude was chosen in a way that allows to determine the sensor noise level at low frequencies (10 Hz to 100 Hz) and that reveals the characteristic resonance peaks needed for parameter extraction at higher frequencies ($f \geq 2\,\mathrm{kHz}$). The mean excitation value is indicated as $\tilde{x}_{\mathrm{f}}$ at the lower left of the corresponding Bode plots (compare with Fig. 3.23). The

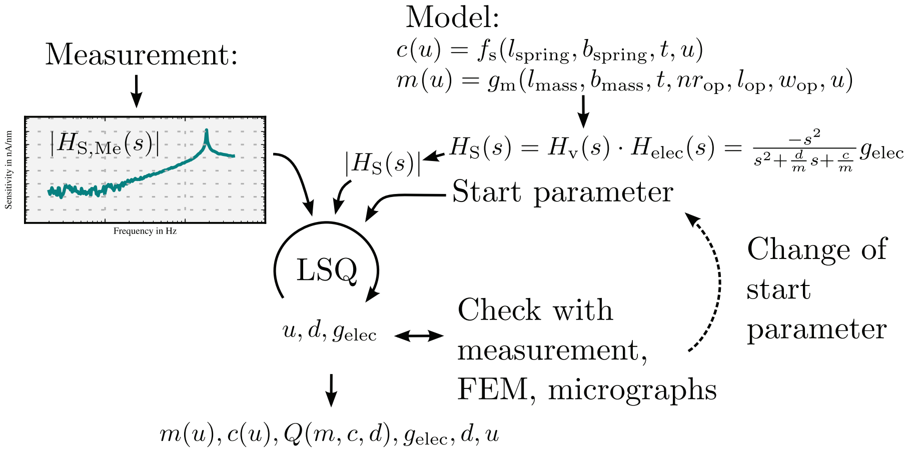

Figure 3.25: Illustration of the procedure to estimate the parameters mass, stiffness, Q-factor and gain of the optoelectrical subsystem using the magnitude response of the sensor from the measurement data and applying an analytical model of the underetching dependent magnitude response $|H_S(f)|$. The stiffness c is a function of the length l_spring, width b_spring and height t of the spring beams. The mass m depends on the length l_mass, width b_mass and height t of the structure, and on the length l_op, width w_op and the number of the openings nr_op.

sensor behavior regarding different input deflections is discussed separately in Sec. 3.4.5 while addressing the linearity of the sensor.

Parameter Extraction

Parameter estimation was done with an iterative least squares algorithm. The damping coefficient d and the underetching u of the MEMS as well as the gain of the opto-electronic readout g_elec were fitted to the magnitude curves of the sensitivity $|H_\mathrm{S}(f)|$. Figure 3.25 overviews the procedure of the parameter estimation including the underetching dependent model for the stiffness c and the mass m. The parameter estimation procedure uses only the part of the $|H_\mathrm{S}(f)|$ data that is indicated by (yellow) circles in Fig. 3.23 in order to avoid artifacts in the magnitude curve originating from shaker resonances (e.g., Fig. 3.29 at 3.1 kHz). The data range for the LSQ identification was selected manually. To identify the shaker resonances, the phase of the laser vibrometer is a valuable aid (run of φ_f at 350 Hz and 3.1 kHz in Fig. 3.23). The estimate of the underetching and, therefore, the values of mass and stiffness is relatively robust. The estimate of the damping coefficient on the other hand, strongly depends on the first estimate of the gain of the electrical subsystem g_{elec}, which could even yield, e.g., a negative value for d. In this case, the first estimate for u, d and g_{elec} has to be readjusted and the fit procedure has to be repeated until the resulting values of the magnitude match the measurements and the parameters fulfill the physical conditions, such as d, c and m having to be greater than zero.

The fitted underetching for the chip E-12 is $u = 374\,\mathrm{nm}$. By means of FEM[2] analysis a modified sensor shape was modeled and simulated considering the underetching u. For E-12 the resulting first natural frequency in x-direction is 1862 Hz. The simulation was performed with an isotropic material with a Young's modulus of $E_x = E_y = 170\,\mathrm{GPa}$ [48]. The measured resonance frequency of 1848 Hz deviates from the simulated result by less than one percent. Based on analytical models the resonance frequency was designed to be 2500 Hz. This value was also cross checked by FEM analysis which delivered a first natural frequency of 2578 Hz and hence a deviation of about three percent. Detailed information about the FEM simulation results can be found in Section 3.4.1. Additionally, the quality factor was computed with the determined parameters f_{res}, m and d, (Tab. 3.5):

$$Q = \frac{f_0}{B} = \frac{\omega_0 m}{d} \approx \frac{\omega_{\mathrm{res}} m}{d} \tag{3.3}$$

(see also Eq. 2.21). The difference between the natural frequency ω_0 and the (damped) resonance frequency ω_{res} is negligible. Due to the small damping ratios ($D_{\mathrm{E-12}} = 3.3 \cdot 10^{-3}$),

$$\omega_{\mathrm{res}} = \omega_0 \sqrt{1 - D^2} \quad , \tag{3.4}$$

the corresponding frequency shift is less than one percent.

Determination of the NED

Figure 3.26 illustrates how to determine the noise equivalent displacement (NED) by the measured transfer function $H_{\mathrm{S}}(f)$ of the sensor, the acquired sensor output voltages $V_{\mathrm{Out}}(f)$, the applied deflection of the foundation x_{f} and the estimated noise floor V_{Noise} of the fully functional sensor device. The frequency range measured with the experimental set-up does not sufficiently exceed the region of resonant enhancement of the sensor transfer function. Thus, signal levels beyond the measurement range ($V_{\mathrm{Out,B}}$) have to be extrapolated according to the transfer characteristic derived of measured signals ($V_{\mathrm{Out,A}}$). For simplicity and due to its low variation with frequency is

---

[2] COMSOL Multiphysics®.

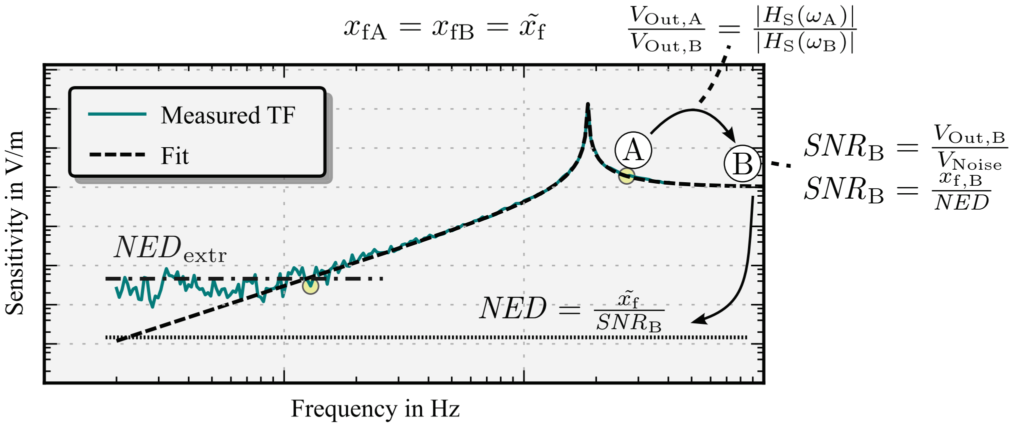

Figure 3.26: Determination of the NED. The first value of the magnitude, that is unaffected by shaker resonances is labeled by an 'A'. The values $V_{\mathrm{Out,B}}$ and SNR_{B} at 20 kHz are indicated by 'B' and calculated by means of the fitted model.

the amplitude of the foundation (after compensation) set to its mean value (compare Fig. 3.21)

$$x_{\mathrm{fA}} = x_{\mathrm{fB}} = \tilde{x}_{\mathrm{f}} \quad . \tag{3.5}$$

For the calculation of the SNR, the noise voltage V_{Noise} is determined by a fully functional opto-electrical subsystem and without the excitation of the shaker. A representative measurement of V_{Noise} of the chip D-6 is depicted in Fig. 3.27. Corresponding measurements were done for each studied sensor and repeated with the LED switched-off. The SNR at frequency f_{B}, is defined herein as ratio of RMS signal to RMS noise values $V_{\mathrm{Out,B}}/V_{\mathrm{Noise}}$ for 1 Hz bandwidth. It can be calculated with

$$\frac{V_{\mathrm{Out,A}}}{V_{\mathrm{Out,B}}} = \frac{|H_{\mathrm{S}}(f_{\mathrm{A}})|}{|H_{\mathrm{S}}(f_{\mathrm{B}})|} \tag{3.6}$$

from

$$SNR_{\mathrm{B}} = \frac{V_{\mathrm{Out,B}}}{V_{\mathrm{Noise}}} = \frac{x_{\mathrm{f,B}}}{NED} = \frac{\tilde{x}_{\mathrm{f}}}{NED} \quad . \tag{3.7}$$

The SNR can be rewritten in terms of the noise equivalent displacement

$$NED = \frac{\tilde{x}_{\mathrm{f}}}{SNR_{\mathrm{B}}} \quad . \tag{3.8}$$

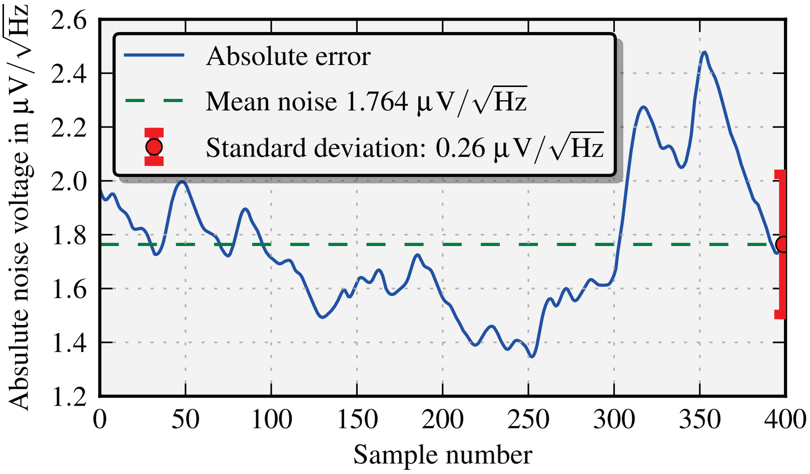

Figure 3.27: Measured RMS noise voltage density at 13372 Hz with the LED switched on and with the D-6 chip at rest. The measurement reveals that the noise level obtained by the lock-in amplifier (SR830) is not constant which was overcome by calculating the mean value of 400 samples acquired in two minutes.

For practical considerations, another definition of the NED in terms of $|H_\mathrm{S}(f)|$ is meaningful as it is shown in Fig. 3.30. Here, the NED is calculated from $\tilde{x}_\mathrm{f} = 2\,\mathrm{nm}$ divided by SNR, the sensitivity ratio of the value at higher frequencies $(710\,\mathrm{nA/nm})$ and the sensitivity at low frequencies $(10\,\mathrm{nA/nm})$ where the sensor phase starts fluctuating. The resulting value of $NED_\mathrm{extr} = 35.2\,\mathrm{pm}/\sqrt{\mathrm{Hz}}$ exceeds enormously the above calculated $NED = 0.647\,\mathrm{pm}/\sqrt{\mathrm{Hz}}$. This larger value is due to the extrinsic, acoustic and mechanical disturbances originating from, e.g., fans inside the measurement equipment (acoustic interferences) or the shaker system during the measurement of the transfer characteristic. The measurement of V_Noise (referred to 1 Hz power bandwidth) is done at a frequency of 13372 Hz which is much greater than the sensor resonance frequencies with the shaker switched off. Therefore, the extrinsic acoustic noise does not significantly affect the value of V_Noise.

Table 3.6 summarizes the noise equivalent displacement determined by noise measurements of V_Out at rest and the estimations of NED_extr of the measured transfer functions $H_\mathrm{S}(f)$. Additionally, the noise equivalent velocity NEV_Laser of the laser vibrometer was calculated from $\tilde{x}_\mathrm{f} \cdot \omega_{NEV}$ where ω_{NEV} is the lowest angular frequency at which the laser phase is sta-

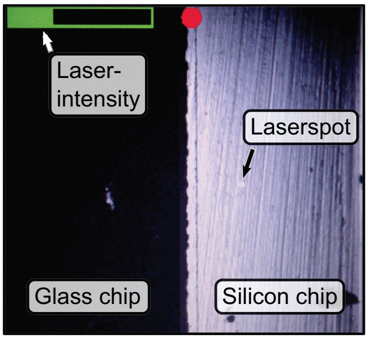

Figure 3.28: Micrograph taken with the MSA microscope showing a side face of the chip and the spot of the laser. The roughness of the chip's side face originates from wafer dicing.

ble (compare Sec. 3.3.1). NEV_{Laser} is crucial for measurements with small excitations of the foundation because the laser signal becomes unstable at relatively low frequencies and the magnitude of the transfer function $|H_{\mathrm{S}}(f)|$ becomes noisy even if the sensor has not reached its NED which is due to the computation of $\frac{|V_{\mathrm{Out}}(f)|}{|X_{\mathrm{f}}(f)|}$. An example of this can exemplarily be seen in the phase plot of Fig. 3.31 where the phase relation of the sensor output φ_{Out}, is still stable at 28 Hz, whereas the phase of the laser φ_{f} fluctuates below 44 Hz. The VD-02 vibrometer controller user manual lists a resolution of $0.15\,\mu\mathrm{m(RMS)}/\mathrm{s}/\sqrt{\mathrm{Hz}}$ resulting in $0.212\,\mu\mathrm{m\,Vpp}/(\mathrm{s}/\sqrt{\mathrm{Hz}})$ under best conditions as ideally reflecting surfaces which are not fulfilled on the side faces of the chip (Fig 3.28) [62].

Chip E-12. The shape of the single apertures of the chip E-12 are quadratic (Fig. 3.3). As described by Eq. 2.37, the signal to noise ratio SNR_{i} related to the photocurrent suggests the use of a high aspect ratio for l_{e}/W_0, resulting in a higher noise level for quadratic aperture shapes. Chip E-12 has 1720 openings of a size of $20\,\mu\mathrm{m}\times 20\,\mu\mathrm{m}$ each in both the silicon device layer and the Cr layer. The size and shape of the aperture result in an effective edge length l_{e} of 34.4 mm. This is the smallest value of l_{e} of all discussed chips. The chip area of $1.74\ \mathrm{mm}\times 1.74\ \mathrm{mm}$, on the other hand, is comparable to the one of D-15, K-6 or D-6, the most sensitive chip. The corresponding transfer characteristic is shown in Fig. 3.23. As stated by Eq. 2.8, the second-order transfer function of the mechanical subsystem H_{v}, exhibits an output signal which grows with at least +40 dB per decade at frequencies below the resonance. At the mechanical resonance at 1.85 kHz, the sensitivity peaks with 13.4 µA/nm. According to the fitted second order high pass the sensor exhibits a sensitivity of 105 nA/nm at 3 kHz which further drops down to 102 nA/nm for higher frequencies (see the 'Fit'-curve in Fig. 3.23). The measured noise level

Chip-code	NED $\mathrm{pm}/\sqrt{\mathrm{Hz}}$	NED_{extr} $\mathrm{pm}/\sqrt{\mathrm{Hz}}$	SNR_{extr} 1	f_{extr} Hz	$\tilde{x}_{\mathrm{f}}$ nm	NED_{Br} $\mathrm{pm}/\sqrt{\mathrm{Hz}}$	$NED_{\mathrm{LED,off}}$ $\mathrm{pm}/\sqrt{\mathrm{Hz}}$	NED_{Res} $\mathrm{pm}/\sqrt{\mathrm{Hz}}$	NEV_{L} $\mathrm{^{\mu m}/_{s}}/\sqrt{\mathrm{Hz}}$	f_{NEV} Hz
E-12	**0.647**	35.2	108	177	4	0.0169	0.0351	0.000607	1.58	66.3
J-18	0.173	28.3	259	48	7	**0.218**	0.00568	0.000115	2.49	53.9
D-6	**0.231**	27.9	80	94.8	2	0.176	0.00724	0.000425	1.88	134
M-4	0.674	122[a]	47.2	28.6	6	**1.9**[b]	0.0146	0.000766	1.61	44.3
K-6	**0.348**	27.3	139	128	4	0.0418	0.00767	0.000293	1.46	61.4
D-15	**2.44**	60	72.5	103	4	0.0727	2.34	0.0718	1.32	48

Table 3.6: Comparison of the different noise equivalent displacement (NED) values. The data is determined by noise measurements with a fully operating opto-electrical system. NED_{extr} is the noise equivalent displacement extracted from distortions in the Bode plots of the measured $|H_{\mathrm{S}}(f)|$. $NED_{\mathrm{LED,off}}$ equals the noise level for the MOEMS with a completely closed aperture at rest estimated by a switched off LED. The maximum and, therefore, relevant value for the measurement resolution of NED, NED_{Br} and $NED_{\mathrm{LED,off}}$ is written in bold. NED_{Res} is calculated by the high sensitivity values at resonance and not by the low sensitivity values far above the resonance. NEV_{L} is the noise equivalent velocity calculated by $\tilde{x}_{\mathrm{f}} \cdot \omega_{NEV}$, where ω_{NEV} is the lowest angular frequency at which the laser phase does not fluctuate. Compare with Fig. 3.23.

---

[a] Only a circular area of a diameter of 2 mm is illuminated inside the sensor mounting device and the aperture array of 2.5 mm×2.5 mm yields a lower sensitivity to noise ratio than at full illumination.

[b] The relatively high thermal Brownian noise level is due to the low stiffness of the structure (compare Eq. 2.26).

V_{Noise} at normal operation and input vibrations above 1.85 kHz yields a noise equivalent displacement $NED = 0.647\,\mathrm{pm}/\sqrt{\mathrm{Hz}}$ which can be expressed as a noise equivalent acceleration $NEA = 8.9\,\mu\mathrm{g}/\sqrt{\mathrm{Hz}}$ ($\mathrm{g} = 9.81\,\mathrm{m/s^2}$).

With the noise voltage of 679 nV/$\sqrt{\mathrm{Hz}}$ for the LED switched off, a theoretical displacement resolution of $NED_{\mathrm{LED,off}} = 0.00351\,\mathrm{pm}/\sqrt{\mathrm{Hz}}$, equivalent to an acceleration of 0.482 $\mu\mathrm{g}/\sqrt{\mathrm{Hz}}$, should be achievable for frequencies above 1.85 kHz. The noise voltage for the switched off LED has to be seen in contrast to the noise voltage at the output of the operational amplifier which is of less than 60 nV/$\sqrt{\mathrm{Hz}}$ [63] if equivalent resistors are used instead of the receiver. $NED_{\mathrm{LED,off}}$ is the theoretical noise estimate of the MOEMS for a completely opaque aperture at rest leaving the dark-current noise of the opto-electrical receiver as single noise source. $NED_{\mathrm{LED,off}}$ has to be seen in relation to NED and NED_{Br} the theoretical noise limit of the mechanical subsystem. In the case of chip E-12 this is $NED = 0.647\,\mathrm{pm}/\sqrt{\mathrm{Hz}}$. An overview of all determined noise equivalent displacement values is given in Tab. 3.6.

The extraordinarily low values of NED_{Res} have to be seen in contrast to NED_{Br}. Therefore, is NED_{Res} only relevant if the sensor is operated in vacuum. Hence, the maximum value of NED_{Br}, NED_{Res} and NED finally defines the value relevant for the measurement resolution of the sensor. This maximum value is highlighted by bold numbers in Table 3.6 for each sensor.

Chip J-18. The seismic mass of this type requires few chip space and is supported by folded springs (Fig. 3.4). J-18 features 782 apertures of $10\,\mu\mathrm{m} \times 100\,\mu\mathrm{m}$ on a 1.88 mm² large and 20 µm thick seismic mass. Due to the small dimensions of the mass, the small number of openings and the height of the device layer of 20 µm, J-18 exhibits the lowest damping coefficient d of $3.38\,\mathrm{mg/s}$ of all chip types (Table 3.5). Both, damping and soft springs contribute to the noise equivalent deflection $NED_{\mathrm{Br}} = 0.218\,\mathrm{pm}/\sqrt{\mathrm{Hz}}$ (compare Eq. 2.26), also representing the resolution limit for this sensor. This small sensor exhibits a remarkably high sensitivity of 357 nA/nm which is due to the good illumination of the grating arrays ($x \cdot y =$1 mm×2 mm). One constraint regarding the illumination is the 2 mm diameter of the reflector inside the LED and the phototransistor sensors resulting in an only partially illuminated grating array.

Chip D-6. Type D-6 features the narrowest openings with a size of $5\,\mu\mathrm{m} \times 100\,\mu\mathrm{m}$ on an area of $1.76\,\mathrm{mm} \times 1.68\,\mathrm{mm}$ which is approximately equal to

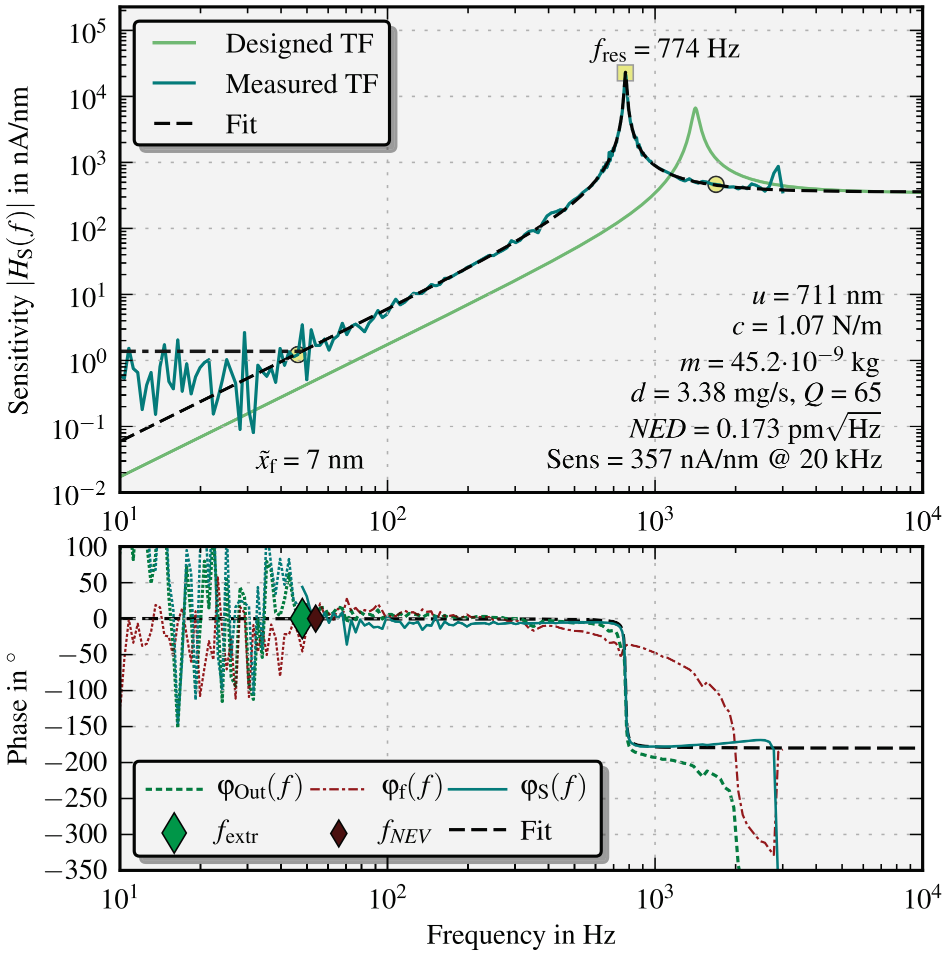

Figure 3.29: Designed and measured sensor transfer function (TF) of chip J-18. The magnitude plot $|H_\mathrm{S}(f)|$ represents the frequency dependent displacement sensitivity of the sensor. All fitting parameters of the MEMS device are listed inside the plot. The uncertainties of the measured sensor signal's phase and the vibrometer signal's phase reveal the transition region where the SNR approximates unity. For J-18 this frequency is $f_\mathrm{extr} = 48\,\mathrm{Hz}$ resulting in $SNR_\mathrm{extr} = 357/1.38 = 259$ at $20\,\mathrm{kHz}$ and a $NED_\mathrm{extr} = 28.3\,\mathrm{pm}/\sqrt{\mathrm{Hz}}$. The phase of the laser starts fluctuating below 53.9 Hz resulting in a noise equivalent velocity of $NEV_\mathrm{L} = 2.49\,\mu\mathrm{m/s}/\sqrt{\mathrm{Hz}}$. The red and the green diamonds indicate the frequency threshold below which the phases of the output signal and the laser vibrometer, respectively, start to fluctuate. The yellow circles indicate the data portions used for the parameter estimation. The yellow square highlights the resonance peak. The constantly decreasing phase of the sensor output and the laser vibrometer could not be completely compensated. Hence, the resulting sensor phase curve still exhibits an additive contribution which increases with frequency.

the chip area of type E-12. The large number of openings $nr_{\mathrm{op}} = 2580$ and the resulting value of $l_{\mathrm{e}} = 258\,\mathrm{mm}$ contributes to the highest sensitivity of 710 nA/nm among the characterized sensors. Due to Eq. 2.38, the high ratio of W_0/l_{e} leads to a low NED of $0.231\,\mathrm{pm}/\sqrt{\mathrm{Hz}}$ but simultaneously limits the dynamic range (Eq. 2.39) to $DR = 20\,\log_{10}\left(\frac{2W_0}{NED}\right) = 153\,\mathrm{dB}$. Chip D-6 exhibits the second highest damping ratio. Due to the lack of an appropriate damping model this can not be clearly assigned to the large number of openings. A more detailed discussion about the damping behavior can be found in Sec. 3.4.3.

Chip M-4. This sensor chip is characterized by two specific features. First, a large mass and aperture area and second, low stiffness of the meander springs. Hence, chip M-4 features the lowest resonance frequency, 196 Hz, among the presented sensors. This design demonstrates the benefits of the freely moving inertial mass, the soft springs and the resulting low resonance frequencies.

In the given set-up and with the applied optoelectrical components, the oscillating mass of M-4 (2.5x2.5 mm²) is only partially illuminated by the LED. Hence, the resulting sensitivity of M-4 is lower than the one of D-6, although, M-4 exhibits the higher effective edge length (compare Table 3.5). The two reasons for the incomplete illumination are imperfections of the chip fixation inside the mounting device and the optical set-up of the LED and phototransistor. An inserted aperture inside the chip fixation with a diameter of 2.5 mm limits the optical path. It defines the maximum possible area illuminated on the phototransistor chip while the reflector of the LED and the phototransistor have a diameter of 2 mm. Hence, only 50 to 78.5 % of the relatively large M-4 chip area can be uniformly illuminated due to these limitations of the set-up. Taking this ratios into account, the sensitivity of M-4 can reach 528 to 830 nA/nm if the intensity at the center of the aperture array can be maintained throughout the complete array.

In terms of noise equivalent displacement, M-4 shows the highest value of $1.9\,\mathrm{pm}/\sqrt{\mathrm{Hz}}$, which originates from thermo-mechanical Brownian noise (Table 3.6). The large Brownian deflection is due to the low stiffness of $0.23\,\mathrm{N/m}$ (compare Eq. 2.26).

Additional information related to the measurement results is summarized in Fig. 3.31.

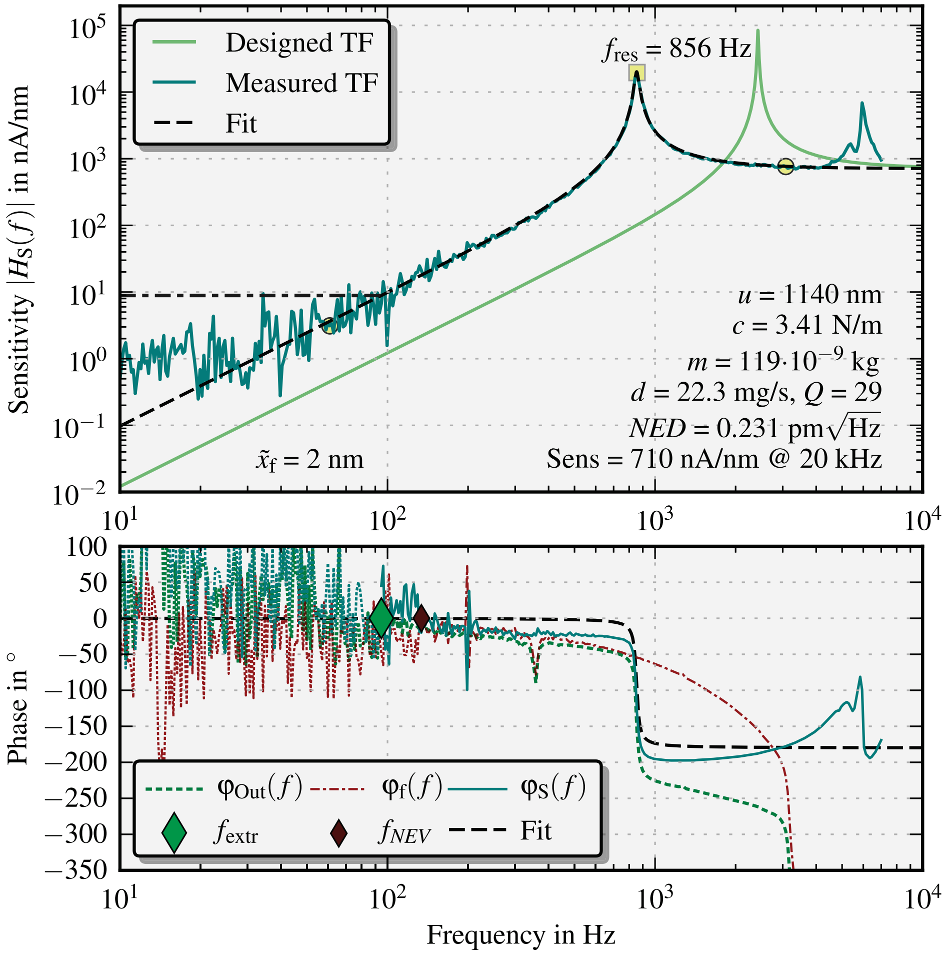

Figure 3.30: Sensor transfer function (TF) of chip D-6. The magnitude plot $|H_\mathrm{S}(f)|$ represents the frequency dependent displacement sensitivity of the sensor. All fitting parameters of the MEMS device are listed inside the plot. The uncertainties of the measured sensor signal's phase and the vibrometer signal's phase reveal the transition region where the SNR approximates unity. For D-6 the transition appears at $f_\mathrm{extr} = 94.8\,\mathrm{Hz}$ resulting in $SNR_\mathrm{extr} = 710/8.87 = 80$ at $20\,\mathrm{kHz}$ and a $NED_\mathrm{extr} = 27.9\,\mathrm{pm}/\sqrt{\mathrm{Hz}}$. The phase of the laser starts fluctuating below 134 Hz resulting in a noise equivalent velocity of $NEV_\mathrm{L} = 1.88\,\mu\mathrm{m/s}/\sqrt{\mathrm{Hz}}$. The red and the green diamonds indicate the frequency threshold below which the phases of the output signal and the laser vibrometer, respectively, start to fluctuate. The yellow circles indicate the data portions used for the parameter estimation. The yellow square highlights the resonance peak. The constantly decreasing phase of the sensor output and the laser vibrometer could not be completely compensated. Hence, the resulting sensor phase curve still exhibits an additive contribution which increases with frequency.

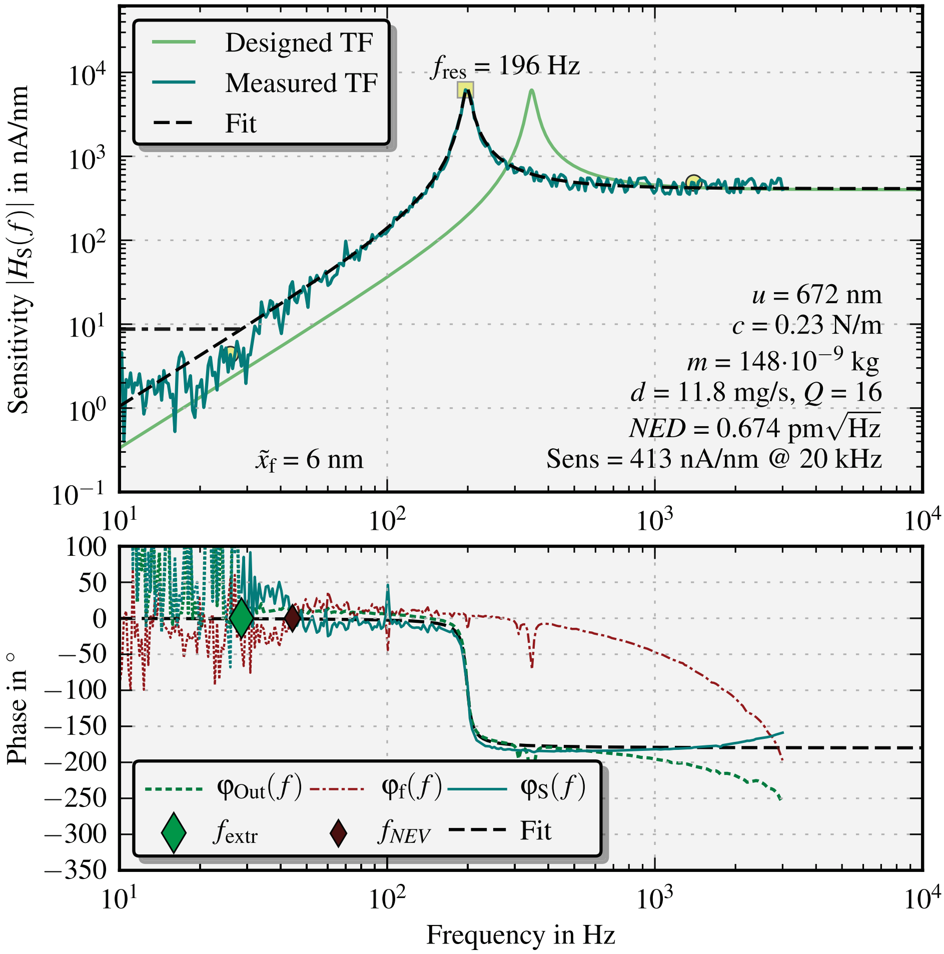

Figure 3.31: Sensor transfer function (TF) of chip M-4. The magnitude plot $|H_{\text{S}}(f)|$ represents the frequency dependent displacement sensitivity of the sensor. All fitting parameters of the MEMS device are listed inside the plot. The uncertainties of the measured sensor signal's phase and the vibrometer signal's phase reveal the transition region where the SNR approximates unity. For M-4 the transition appears at $f_{\text{extr}} = 28.6\,\text{Hz}$ resulting in $SNR_{\text{extr}} = 413/8.74 = 47.2$ at $20\,\text{kHz}$ and a $NED_{\text{extr}} = 122\,\text{pm}/\sqrt{\text{Hz}}$. The phase of the laser starts fluctuating below 44.3 Hz resulting in a noise equivalent velocity of $NEV_{\text{L}} = 1.61\,\mu\text{m/s}/\sqrt{\text{Hz}}$. The red and the green diamonds indicate the frequency threshold below which the phases of the output signal and the laser vibrometer, respectively, start to fluctuate. The yellow circles indicate the data portions used for the parameter estimation. The yellow square highlights the resonance peak. The constantly decreasing phase of the sensor output and the laser vibrometer could not be completely compensated. Hence, the resulting sensor phase curve still exhibits an additive contribution which increases with frequency.

FEM simulation

The FEM simulations were done with $\mathrm{COMSOL\,Multiphysics}^{®}$. Therefore, the analytical MEMS model and least squares fits for parameters could be evaluated during the design period and while the sensor characterization. FEM analysis was used to test the MEMS layout regarding the analytically determined eigenfrequencies. The FEM simulations were computed without damping yielding the natural frequencies of the system. Moreover, the evaluation of eigenmodes, especially the rotatory ones of designs with e.g. complex spring layouts is not possible without the help of FEM. The simulations additionally offer the possibility to analyze the stiffnesses of the movable aperture in z- or y-direction and to obtain the corresponding eigenfrequencies. The stiffness in z-direction (out-of-plane) has to be chosen as high as possible to avoid contact between the deflectable aperture array and the glass wafer.

Analog FEM models were set up to study the influence of the underetching stemming from the anisotropic etching process of the device layer. The shape of the micro-mechanical components was modified (section 3.2.2) leading to a FEM model that considers the underetched parts of the MEMS. The good agreement between the resonance frequencies and the eigenfrequencies suggests a negligible intrinsic stress in the device layer. The fit-procedure does not include Intrinsic stress. Hence, a change in stiffness originating from the intrinsic stress would distort the estimate of the underetching u. The micrographs of the top and bottom side of the movable aperture agree with the estimated underetching.

The eigenfrequencies of the FEM model with underetched MEMS shapes fit the resonance frequencies very well as depicted in Fig. 3.32 and 3.33. This verifies the validity of the parameter estimation. The corresponding results for the structures E-12 and M-4 are discussed in detail in the following section.

Eigenfrequencies of E-12. The shape of E-12 was generated by means of an analytical model, aiming for a natural frequency of 2500 Hz. The FEM model for E-12 without underetching yields an eigenfrequency of 2578 Hz. The deviation of the eigenfrequency is equivalent to an error of 3$\%$.

The simulation of the underetched structure results in a first eigenfrequency of 1862 Hz for an estimated underetching of $u = 374\,\mathrm{nm}$ (see Fig. 3.32). This value is consistent with the obtained resonance frequency of 1848 Hz (Fig. 3.23) revealing an error of less than 1$\%$.

A 2D and a 3D simulation model were set up in order to compute the eigenfrequency in y-direction and z-direction. The lowest eigenfrequency in z-direction was calculated to be 18 kHz, the one in y-direction 177 kHz. The ratio between the eigenfrequencies in x- and z-direction is approximately ten, guaranteeing a high suppression of other modes when the sensor is excited along the x-axis. These two values exemplify the main advantage of straight springs over folded beams, which is a higher stiffness and, therefore, higher eigenfrequencies.

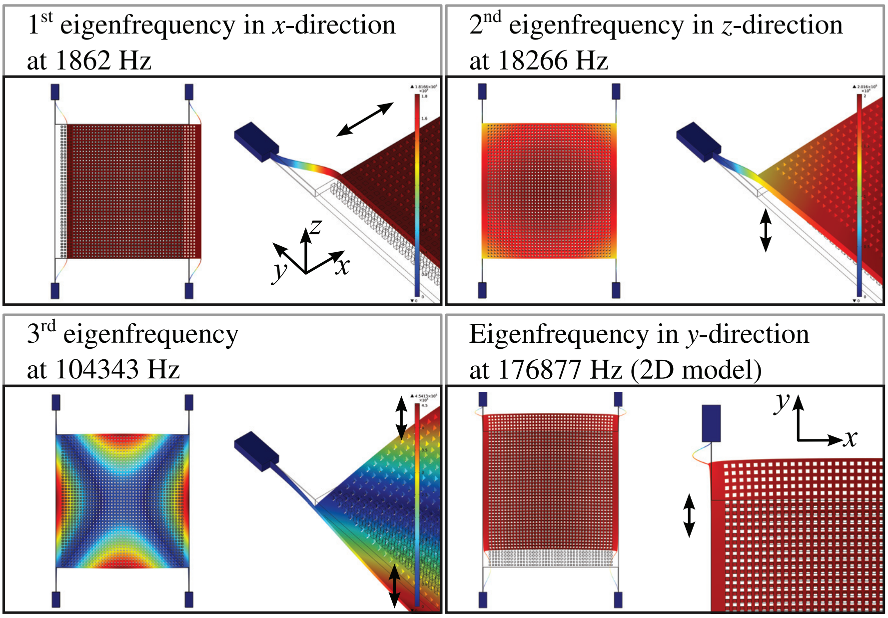

Figure 3.32: Four significant eigenfrequencies obtained by FEM simulation for E-12 with underetching. The height of the Si structure is 45 µm and $u = 374\,\mathrm{nm}$. The second eigenfrequency is by roughly a factor of ten greater than the first one and is related to a vibration in z-direction. The eigenmode in the y-direction (lower right) to 177 kHz is by a factor of approximately 95 greater than the first one.

Eigenfrequencies of M-4. The chip M-4 exhibits a resonance frequency of 196 Hz while it was designed to resonate at 500 Hz. Two models with underetched shapes were set up: Model I has an underetching $u = 674\,\mathrm{nm}$ obtained by a fit to the actual resonance frequency measurements. Model II, on the other hand, has an underetching determined by the micrographs

$u_{\mathrm{mic}} = 583\,\mathrm{nm}$; compare 3.14, top-side: $527\,\mathrm{nm} \pm 372\,\mathrm{nm}$, bottom-side: $640\,\mathrm{nm} \pm 200\,\mathrm{nm}$. Both models exhibit the same eigenmodes but slightly different eigenfrequencies.

Model I exhibits a first eigenfrequency of 203 Hz. The first eigenmode is a vibration in x-direction, which is depicted in Fig. 3.33. The second and third eigenfrequencies at 1472 Hz and 1594 Hz, respectively, are coupled to vibration modes in in y- and z- direction. The relatively low ratio between the frequencies of the eigenmodes in x- and y- direction is a drawback of the meander spring which has to be considered when designing soft springs. However, the ratio of approximately eight between the x- and the z- eigenfrequency is comparable to the straight spring design. A high stiffness in z- direction is also required to prevent contact between the movable and the fixed gratings array. Concerning the sensitivity of the sensor with respect to motions in the y-direction, extremely large aspect ratios of the apertures allow for an efficient suppression of the related vibration signal.

The FEM simulation which was modeled with the underetching determined by micrographs yields the lowest eigenmodes in x-, y- and z-direction at 222 Hz, 1545 Hz and 1715 Hz, respectively. The eigenfrequencies differ less than 15 % from the measurement which is reasonable when one considers the relatively high uncertainty of u_{mic} of up to 70% (Fig. 3.14).

The eigenfrequencies determined by FEM simulation are in good agreement with the resonance frequency. This suggests the validity of the parameter estimated by the least square fit.

3.4.2 Structures for the Modulation of Infrared Light

The performance of the infrared MOEMS readout was studied with two chips with identical spring, equivalent mass areas but different types of apertures. A illustration of the two MOEMS, one with etched openings and the other with a metal aperture, can be seen in Fig. 3.1. The chip working with visible light is K-6 and its infrared equivalent is D-15. A micrograph of D-15 and, in more detail, its apertures can be seen in Fig. 3.34 together with the apertures of K-6. “In contrast to the standard configuration for the sensors operating with visible light [64], was the infrared MOEMS characterized with an inverting operational amplifier that was placed at the output of the transimpedance amplifier. The current through the PIN-diode was computed from the output of the amplifier chain considering the additional voltage gain of the second amplifier of 33.3 and the resulting phase shift of -180°. This inverting amplifier is needed due to the lack of an internal gain of the PIN-

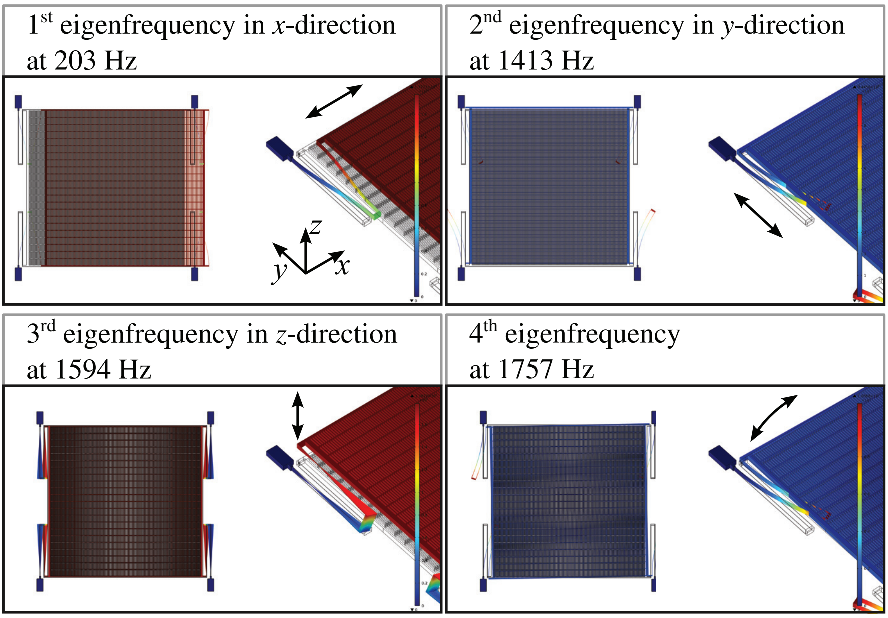

Figure 3.33: The first four eigenfrequencies of the underetched structure M-4 obtained by FEM simulation. The height of the device layer is 45 µm and the underetching $u = 674\,\mathrm{nm}$. The second eigenfrequency is coupled to the eigenmode in y-direction and is approximately by a factor of seven greater than the first one. The eigenmode in z-direction and the rotation around the z-axis corresponds to frequencies of 1594 Hz and 1757 Hz, respectively.

diode (LAPD-1-09-17-TO46) compared to the phototransistor (SFH-3600). Furthermore, the output of the sensor depends on the optical power of the LED and the spectral coupling efficiency between the optical transmitter and the receiver [65]. Corresponding measurement results are discussed subsequently. Firstly, several important characteristics are extracted from the transfer functions of both sensors, although the opto-electrical transmitter-receiver pairs differ in various properties. Secondly, the transfer losses were estimated, considering the transmission through the chips, and the reflections at silicon and/or glass borders."[52]

Chip K-6. "It features a robust and easy to fabricate layout with 1260 openings (10 µm × 100 µm) and four straight springs of a width of 4 µm. The sensor transfer characteristic is depicted in Fig. 3.35, listing also the identified mechanical parameters. The two most relevant parameters in relation to the

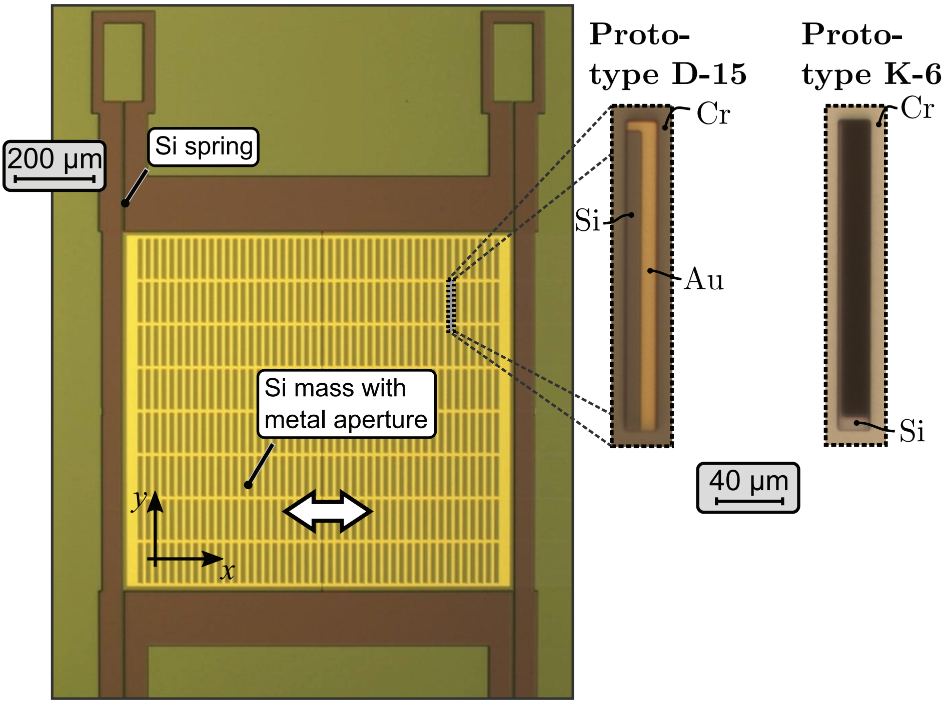

Figure 3.34: Micrograph taken during the fabricating of the silicon structure of a MOEMS operating with infrared light above a wavelength of 1.1 µm. The zoom shows single apertures of D-15 and K-6. Due to misalignment, is the aperture of K-6 almost completely open resulting in a higher noise at the phototransistor and, therefore, a higher *NED* compared to D-6 (see Table 3.5). [52]

infrared sensor are the damping coefficient $d = 21.8\,\mathrm{mg/s}$ and the seismic mass of $158 \cdot 10^{-9}$ kg."[52]

Chip D-15. "Its seismic mass of $308 \cdot 10^{-9}$ kg is approximately twice as large as the one of [K-6]. The higher damping [of 29.3 mg/s] is most probably due to the increased surface area on the top and the bottom side of the mass. Together with a lower resonance frequency, this leads to a smaller Q-factor of the MEMS. Nevertheless, at the time of writing this [thesis] the damping components originating from the openings, the top and bottom face and from side walls are not completely identified and understood. The additive phase shift [by the] second non-inverting amplifier of -180° was corrected in the transfer function in Fig. 3.36."[52]

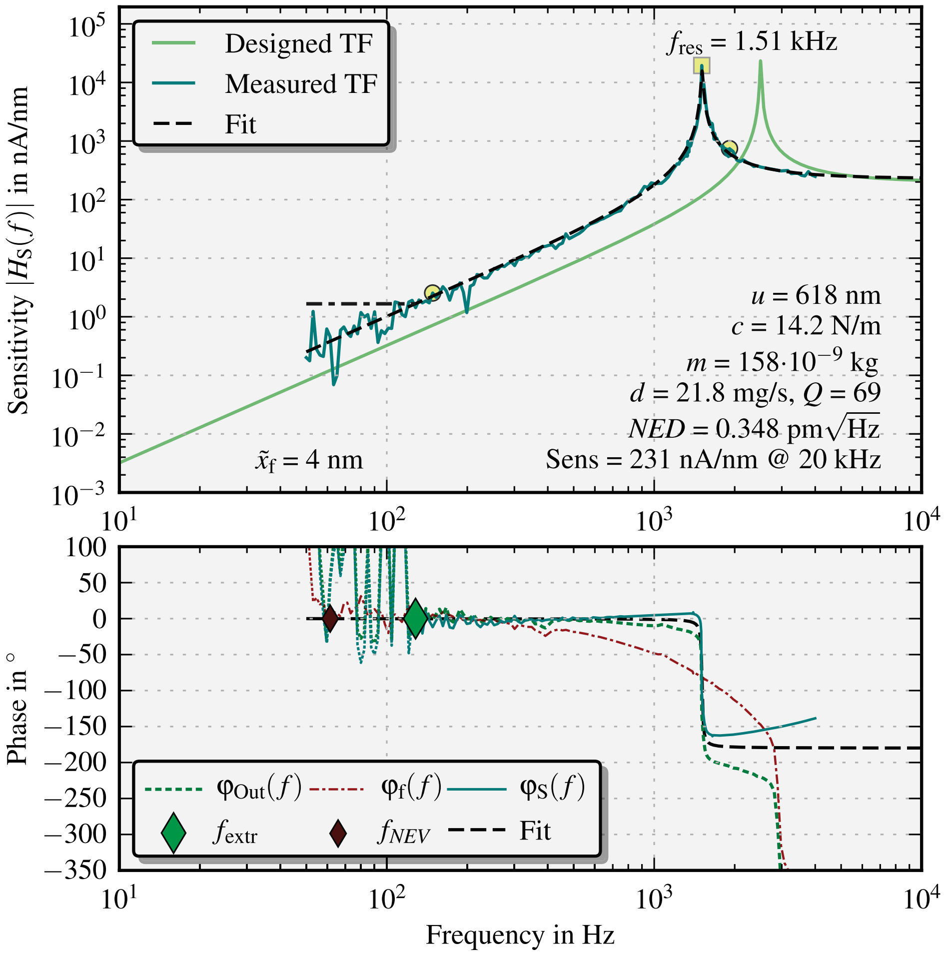

Figure 3.35: Sensor transfer function (TF) of chip K-6. The magnitude plot $|H_{\mathrm{S}}(f)|$ represents the frequency dependent displacement sensitivity of the sensor. All fitting parameters of the MEMS device are listed inside the plot. The uncertainties of the measured sensor signal's phase and the vibrometer signal's phase reveal the transition region where the SNR approximates unity. For K-6 the transition appears at $f_{\mathrm{extr}} = 128\,\mathrm{Hz}$ resulting in $SNR_{\mathrm{extr}} = 231/1.66 = 139$ at $20\,\mathrm{kHz}$ and a $NED_{\mathrm{extr}} = 60.2\,\mathrm{pm}/\sqrt{\mathrm{Hz}}$. The phase of the laser starts fluctuating below 61.4 Hz resulting in a noise equivalent velocity of $NEV_{\mathrm{L}} = 1.32\,\mathrm{\mu m/s}/\sqrt{\mathrm{Hz}}$. The red and the green diamonds indicate the frequency threshold below which the phases of the output signal and the laser vibrometer, respectively, start to fluctuate. The yellow circles indicate the data portions used for the parameter estimation. The yellow square highlights the resonance peak. The constantly decreasing phase of the sensor output and the laser vibrometer could not be completely compensated. Hence, the resulting sensor phase curve still exhibits an additive contribution which increases with frequency.

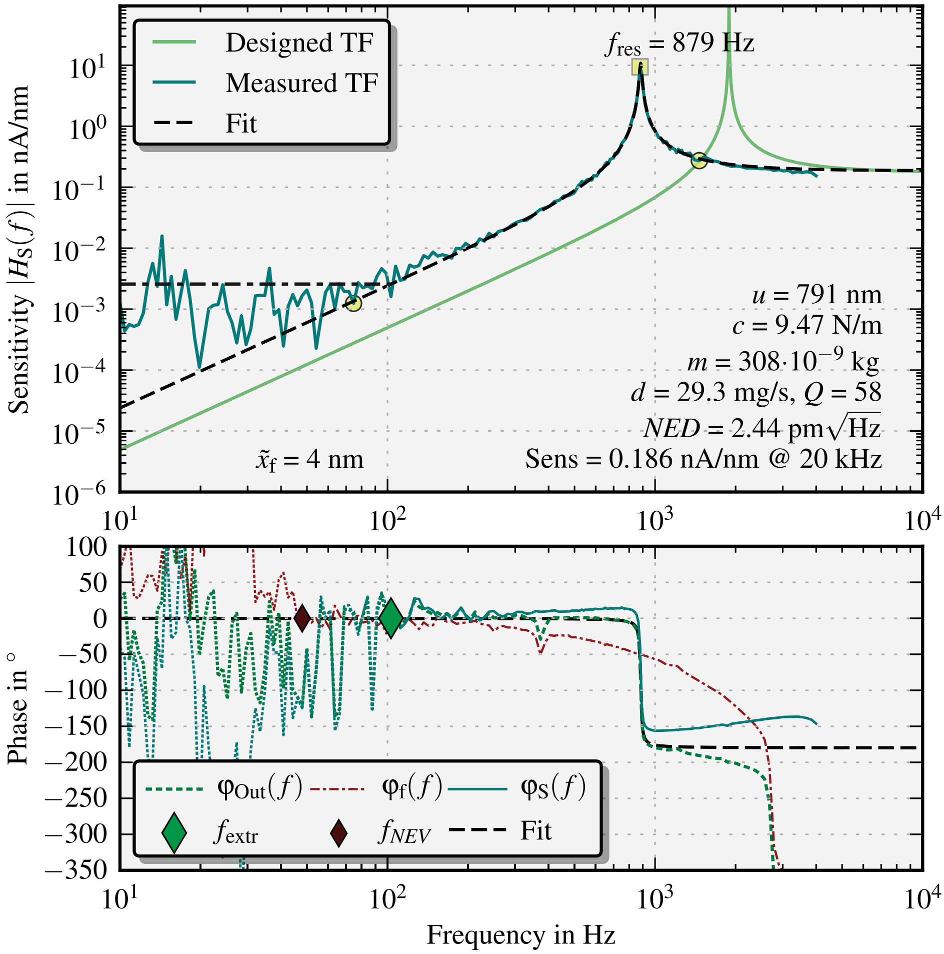

Figure 3.36: Sensor transfer function (TF) of chip D-15. The magnitude plot $|H_{\mathrm{S}}(f)|$ represents the frequency dependent displacement sensitivity of the sensor. All fitting parameters of the MEMS device are listed inside the plot. The uncertainties of the measured sensor signal's phase and the vibrometer signal's phase reveal the transition region where the SNR approximates unity. For D-15 the transition appears at $f_{\mathrm{extr}} = 103\,\mathrm{Hz}$ resulting in $SNR_{\mathrm{extr}} = 0.186/0.00257 = 72.5$ at $20\,\mathrm{kHz}$ and a $NED_{\mathrm{extr}} = 60.2\,\mathrm{pm}/\sqrt{\mathrm{Hz}}$. The phase of the laser starts fluctuating below 48 Hz resulting in a noise equivalent velocity of $NEV_{\mathrm{L}} = 1.32\,\mu\mathrm{m/s}/\sqrt{\mathrm{Hz}}$. The red and the green diamonds indicate the frequency threshold below which the phases of the output signal and the laser vibrometer, respectively, start to fluctuate. The yellow circles indicate the data portions used for the parameter estimation. The yellow square highlights the resonance peak. The constantly decreasing phase of the sensor output and the laser vibrometer could not be completely compensated. Hence, the resulting sensor phase curve still exhibits an additive contribution which increases with frequency.

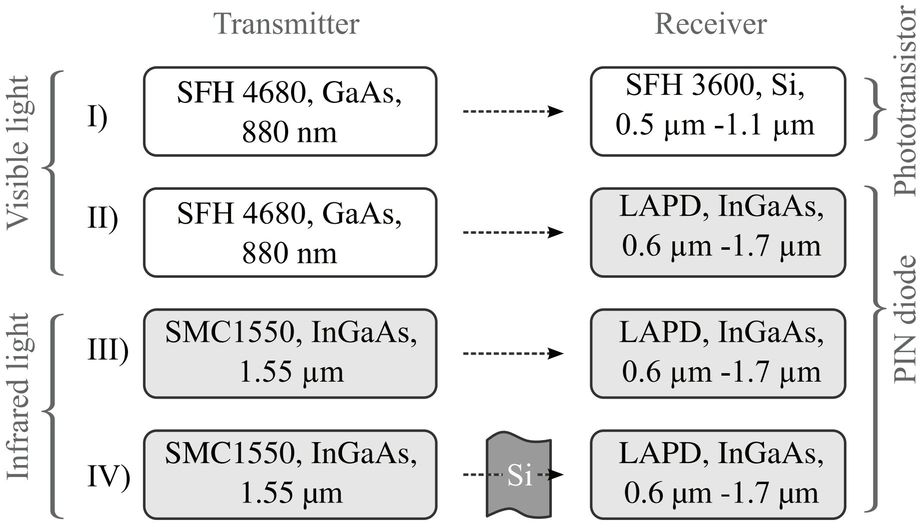

Figure 3.37: Overview of the measurements with different opto-electrical transmitter-receiver pairs.

Coupling Efficiency. “The differing efficiencies of the MOEMS modulators of D-15 and K-6 are not only due to the different characteristics of the optoelectronic devices. Therefore, they can not be estimated directly from the transfer functions [alone]. Hence, additional measurements with different transmitter-receiver configurations were performed with a removed MEMS chip (Fig. 3.37).

The series resistor of the LED, R_{LED}, was set to $8.25\,\mathrm{k}\Omega$ to avoid any saturation of the transimpedance amplifier by lowering the forward current through the LED and, therefore, its [emmission]. The PIN-diode of the infrared approach features a reasonable responsivity of 0.2 A/W or 0.95 A/W when using it in combination with LEDs emitting at 880 nm and 1550 nm, respectively. This allows the direct comparison of the emitters and an indirect comparison of the receivers. The corresponding results in terms of output voltages and the offset voltage at the output of the transimpedance amplifier are listed in Table 3.7.

Case I) and III) in Fig. 3.37 correspond to combinations of transmitter, modulator and receiver used for the measurements. Case II) and III) were performed to get qualitative measures in comparing the transmittance of the infrared and the optical set-up, respectively. Measurement II) and III) exhibit a higher dissipated optical power from SFH 4680 of factor 5 including the lower responsivity of 0.2 A/W at 880 nm compared to 0.95 A/W at 1550 nm

	Output voltage	Output ratio to I)	Detector responsivity	Output ratio to II) incl. responsivity
I)	4.72 V	1	96 A/W	/
II)	11.1 mV	0.00235	0.2 A/W	1
III)	10.5 mV	0.00222	0.95 A/W	0.2
IV)	4.55 mV	0.00098	0.95 A/W	0.0885

Table 3.7: Overview of all measurements were made with a series resistor R_{LED} of $8.25\,\mathrm{k}\Omega$ instead of $660\,\Omega$ to avoid a saturation of the transimpedance amplifier. The listed output voltage is the difference voltage when the LED is switched on and off.

[66, 67, 68]. The comparison of I) and II) reveals a responsivity of SFH 3600 at 880 nm that is by a factor of 0.00235 lower than the one of the infrared PIN-diode receiver. To estimate the reflection losses caused by the Si-mass, case III) and IV) have to be compared."[52]

Transmission Ratio. "The transmission ratio for perpendicularly incident light hitting the boundaries of a transparent slice in air (glass or a silicon chip) can be calculated by

$$\tau = \frac{2n_{\mathrm{rel}}}{n_{\mathrm{rel}}^2 + 1} \quad , \tag{3.9}$$

where $n_{\mathrm{rel}} = n_2/n_1$ is the relative refraction index, n_1 and n_2 are the refraction indices for the slice and air, respectively [69]. Equation 3.9 considers multiple internal reflections inside the chips. The refraction index for silicon at 880 nm is $n_{\mathrm{Si}} = 3.64$ and $n_{\mathrm{Si}} = 3.47$ for 1550 nm [70]. For borosilicate glass is $n_{\mathrm{Gl}} = 1.51$ at 880 nm and 1.5 at 1550 nm [71].

Cases III) and IV) enable an estimate for the transmission ratio of a bare silicon chip. According to Table 3.7, the measured ratio is 44.3 %. This value compares to 53.2 % obtained by Eq. 3.9.

[Considering] the transmission ratio of a glass chip to the ratio between I) and IV) yields a [total] ratio of 1100. The ratio between the sensitivities of D-15 and K-6 is 0.000805 (compare Fig. 3.36 and Fig. 3.35). The difference between the two values of less than 12 % is due to the slight misalignment of the transmitter-receiver pairs.

The prototype MOEMS incorporates a glass chip additionally to the silicon chip, resulting in a transmission ratio of the MEMS components of

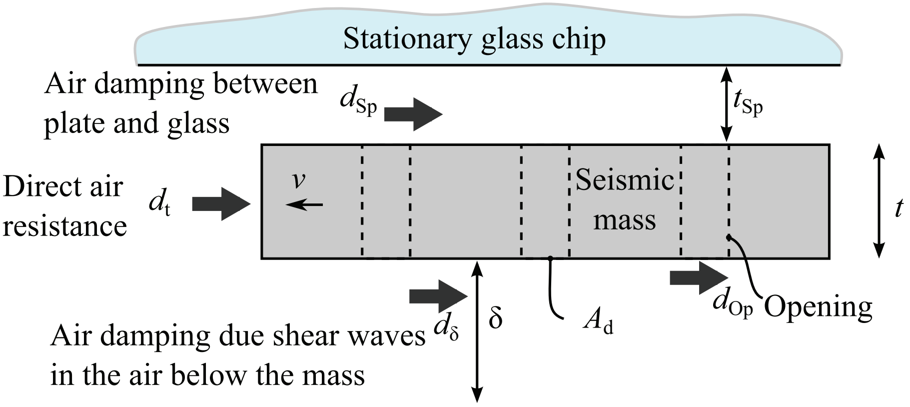

Figure 3.38: Schematic of the contributing damping components for the MOEMS.

49.1 %. Two methods are at hand in order to avoid transmission losses for future sensors. First, the fixed aperture could be fabricated on top of the transmitter making the glass chip obsolete. Second, the fabrication of anti-reflection coatings on both the silicon and glass wafer can increase the transmission ratio up to more than 98 % for 1550 nm [72, 73].”[52]

3.4.3 Damping

In general, damping a process of energy dissipation. A sensor with low damping features a high Q-factor and, in the proximity of its fundamental resonance frequency, a significant overshoot. Consequently, vibrational input near the resonance becomes strongly amplified. Considering transient excitation signals, this results, in principle, in unwanted overshooting. Additionally, lowly damped sensors exhibit intense ringing and a relatively long settling period. For most sensor applications it is essential to determine the damping of the sensor and, therefore, to predict its behavior and to design the structure to exhibit the desired damping performance.

To the best knowledge of the author, the air damping of the MOEMS can be attributed to the three components (Fig. 3.38). However, the damping ratios of the sensors in Table 3.5 reveal a substantial design potential of their damping. Hence, suggestions to design the damping can be stated following:

- The surface on top of the MEMS introduces Couette laminar flow in the gap when it moves relative to the glass substrate (d_{Sp}). The surface

on the bottom side of the MEMS mass induces shear waves into the air underneath (d_δ). Both surfaces depend on the number and size of openings inside the silicon structure. Hence, due to the lack of openings the estimated damping ratio for the infrared MOEMS D-15 is somewhat higher than the one for K-6.
The following design rules do result from the above:

  - The damping by the laminar flow can be modified by changing the spacer distance t_{Sp}.
  - The area of the seismic mass contributes to the laminar flow and the shear waves can be modified by choosing the chip area of the mass and the number of openings.

- The thickness of the MEMS mass affects the damping at the sidewalls perpendicular to the deflection of the mass d_{t}. However, the data listed in Table 3.5 suggests that this contribution is negligible. The MEMS fabricated into a 20 µm device layer (J-18 and M-4) do not feature extraordinary lower damping ratios than the one in 45 µm (e.g. E-12 or K-6). However, the 20 µm thick MEMS also exhibits a higher spacer, which reduces the laminar flow and makes an interpretation of the available data extraordinarily difficult.

  - The damping on the sidewalls of the MEMS can easily be reduced by lowering the thickness of the seismic mass.

- The openings contribute to the damping; it depends on the number and shape of the openings. If the opening in-plane cross-section is large compared to the thickness t of the device layer, then the sidewalls inside the opening act comparable to the outer mass sidewalls (see above) and the viscous damping between the plate and the glass surface is significantly reduced. If the size of the opening is small compared to t, then the air inside the openings is moved together with the seismic mass. Hence, the existence of openings cause only a negligible reduction of the damping d_{Sp}.

  - The damping contribution of the openings is the most difficult one to calculate because it is additionally dependent on the shape of the opening which has up to now not been discussed in literature.

The damping of a certain sensor can be set not only by changing the pressure inside the MEMS housing, but also by inserting openings in the mass or additional arms attached to the mass and by varying the spacer distance to the fixed aperture. The arms can also serve as optical apertures and, therefore, additionally enhance the sensitivity of the sensor. However, further research is needed on this topic to be able to design sensors with, e.g., a critical damping ratio to avoid overshooting and ringing.

3.4.4 Noise Considerations regarding Aperture Shape

The design rule given by Eq. 2.38 was evaluated with the three sensor prototypes E-12, K-6 and D-6. “The opto-electro-mechanical conversion of the examined MOEMS is expected to follow [47]

$$i_{\mathrm{x}} \propto x_{\mathrm{d}} l\, I \qquad , \tag{3.10}$$

where i_{x} is the displacement related photo-current change, I the illumination of the MOEMS, l_{e} the total length of the moving edge and x_{d} is the relative displacement of the seismic mass. The displacement resolution $x_{\mathrm{d,R}}$ is inversely proportional to the square root of l_{e} [47],

$$x_{\mathrm{d,R}} = NED \propto \sqrt{\frac{W_0}{l_{\mathrm{e}}\, I}} \quad . \tag{3.11}$$

where W_0 denotes the width of the apertures. The above discussed relation for the three examined sensors is depicted in Fig. 3.39.”[64] The different misalignment for each sensor chip was taken into account by using W_0 and l_{e} values determined by micrographs. The intersection of the prolonged curve with the abscissa is the *NED* caused by stray light when the aperture is closed. This noise can be reduced by a decreased spacer height and by adopting the aperture shape.

3.4.5 Linearity

For all presented sensor prototypes the transfer functions were determined at several different excitation levels. The transfer characteristic regarding mean input deflection and output signal can be obtained by the corresponding signals at a specific frequency. Figure 3.40 depicts the almost perfectly linear dependency of the receiver current on the deflection of the sensor’s foundation. The chip K-6 with its rectangular apertures was excited at 500 Hz.

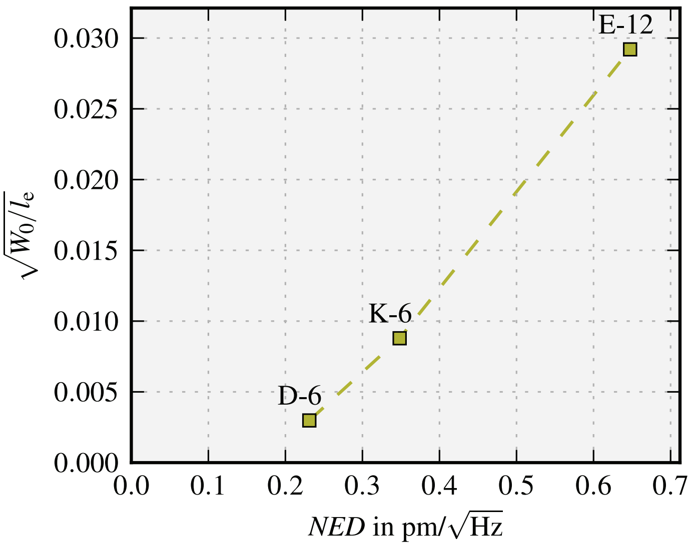

Figure 3.39: The measurement confirms the proportionality between NED and the square root of the geometric parameters.[64]

With the linear fit the system's sensitivity was estimated to be 0.103 µA/nm (at 500 Hz) [64]. For input deflections above 4 nm the mean linearity error is below 0.5 %, but the linearity error increases to more than 10 % at input deflections below 1 nm.

"The linearity of the complete sensor depends primarily on the linearity of the phototransistor. The MEMS part and the operational amplifier operate linearly over several decades of deflection and input current. Due to the dependency of the DC gain (h_{FE}) on the collector current i_{pc}, the phototransistor is only linear over three to four decades of illumination. This disadvantage is not present when using a photodiode whose output is linear in respect of incident light [17, 37]. However, a nonlinear characteristic of the phototransistor on the incident light can be compensated [by an] appropriate design of the apertures. The operation point of the phototransistor can be chosen by the amount of incident light and can be controlled via the LED current. To avoid [a saturation of the operational amplifier], the gain of the current [to] voltage conversion stage has to be adjusted."[27]

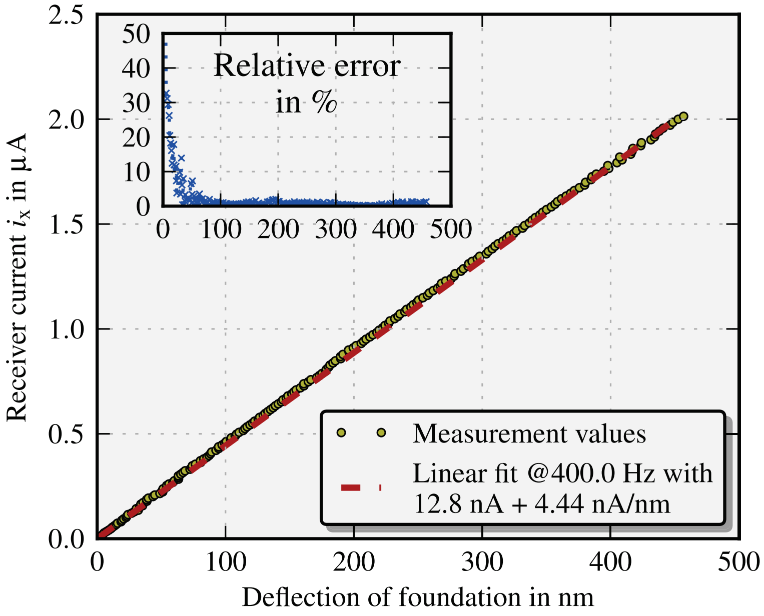

Figure 3.40: Linearity plot of the sensor chip K-6. The receiver output current in respect to the displacement of the foundation at 500 Hz shows good agreement with the linear fit. The inset depicts the deviation from the linear fit. For input deflections above 100 nm the relative linearity error is below 2 %, but the error dramatically increases to more than 400 % for input deflections below 1.5 nm.

3.5 Combdrive-actuated MOEMS

Combdrive-actuated MOEMS have been used to determine the noise dependency on the shape of the apertures (Sec. 2.3.2). The incorporated combdrive allows self-testing, the feed-in of an external signal or an electro-mechanical feed-back. The structures in Fig. 3.41 have two combdrives to deflect the apertures in both directions along the x-axis. Both combdrives operate with up to 35 V, resulting in a deflection range of ±20 µm.

3.5.1 Measurement Set-up

“[The MOEMS] dies were glued to a printed circuit board (PCB) which also establishes the electrical connections to the combdrives. The PCB, together with the LED and the phototransistor was placed inside a mounting device which is depicted in Fig. 3.42. The sensor mounting device allows the recur-

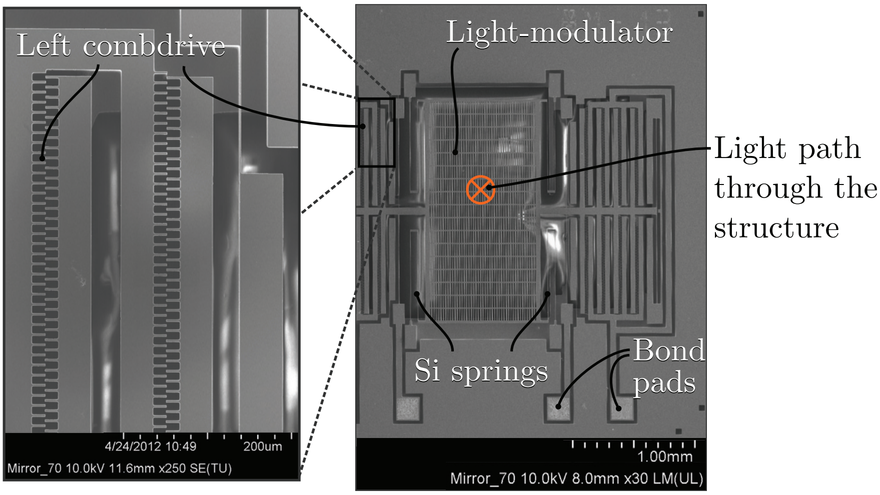

Figure 3.41: Scanning electron micrographs of a typical combdrive structure. The white areas are caused by electrostatic charges from the scanning electron microscope at the glass below the silicon wafer.

rent assembly of all subparts of the MOEMS sensor with sufficient accuracy. Removing the LED from the described set-up enables in situ investigation of the micromachined structures and their deflection according to the applied voltage at the combdrives (see Fig. 3.42 (a)). The noise level of the output voltage signal V_{Out} was recorded utilizing a Stanford Research Lock-In amplifier of type SR830. The mean value of the output voltage itself was measured with the use of a Tektronix oscilloscope TDS2014. The micrographs in Fig. 3.43 show the increasing aperture opening for rising voltage at the combdrive CD-Left which can be seen in Fig. 3.41. The width W_{open} and length $l_{\mathrm{e}}/nr_{\mathrm{op}}$ of the open area of the array elements were measured with a microscope. The light flux through the apertures of total area A_{eff} introduces a photocurrent at the phototransistor which is amplified and converted to a voltage. The resulting output voltage V_{Out} is recorded together with the noise level V_0.

In conjunction with (Eq. 2.32) this relationship is also apparent in the measurement data depicted in Fig. 3.44. Due to stray light and diffraction phenomena the value of the collector current $i_{\mathrm{pc},0}$ does not start with zero at $A_{\mathrm{eff}} = 0$ where the aperture cross section area is completely shut. This is mainly caused by the pattern separation with the relatively high SU-8 spacer of more than [4 µm]. Additionally, the use of the same dimensions for the

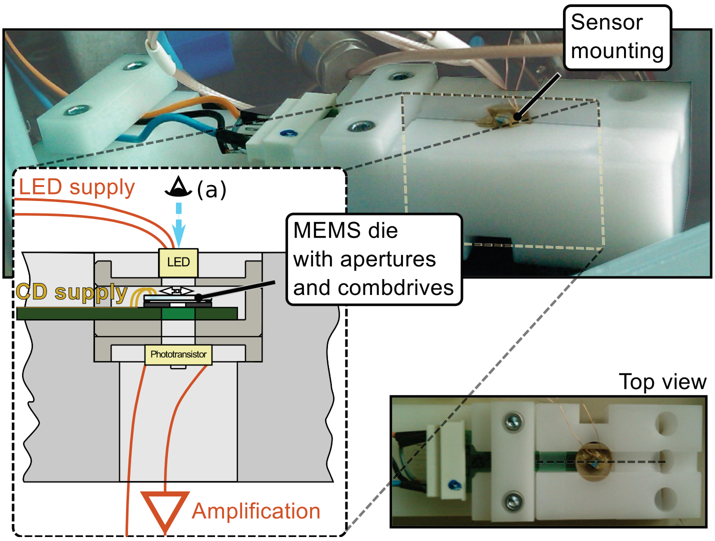

Figure 3.42: Measurement set-up with seperatly mounted LED, phototransistor and MEMS (a) allowing also in situ inspection of the micromachined structures when the LED is absent. The deflection of the MEMS parts is controlled by the voltage at the combdrives.[47]

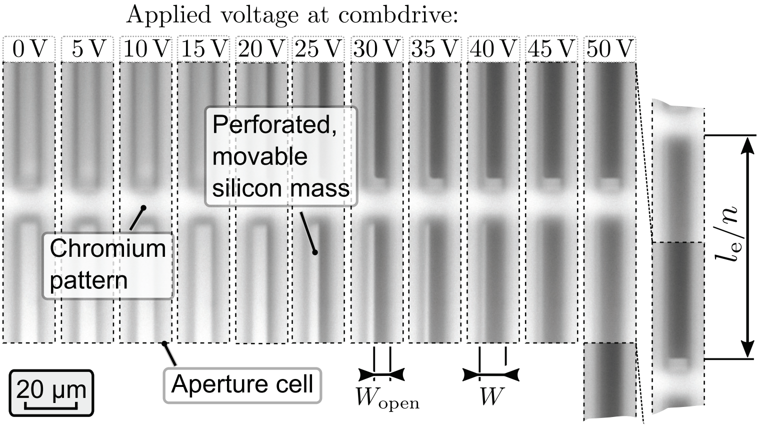

Figure 3.43: Micrographs of an aperture cell with increasing transparent area from left to right defined by $A_{\text{eff}} = l_e \cdot W_{\text{open}}$. The investigated MOEMS sensor features $nr_{\text{op}} = 782$ of these aperture cells with a size of 20 µm × 100 µm.[47]

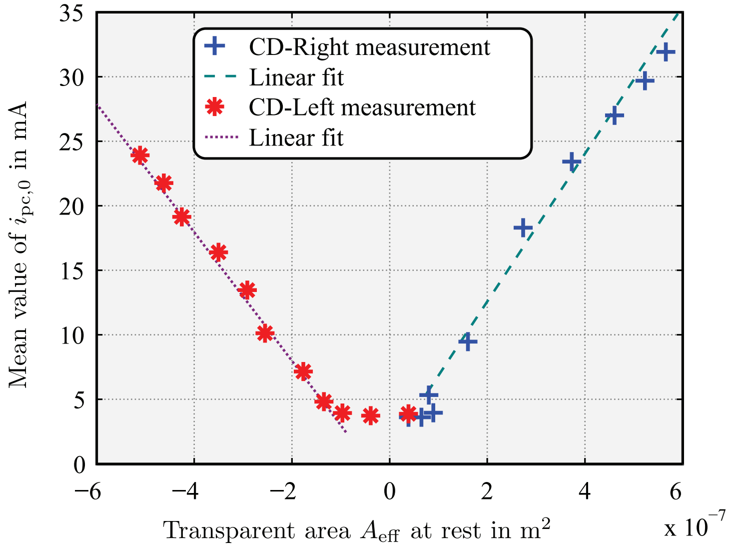

Figure 3.44: Collector current of a phototransistor $i_{pc,0}$ versus the effective aperture cross section area A_{eff}. Negative area values indicate the use of the combdrive 'CD-Left'. The slight asymmetry of the curve to negative values of A_{eff} is due to a slight miss-alignment of the apertures.[47]

aperture in chromium and the one in silicon and slight misalignment also causes this deviations.

According to the phototransistors datasheet the dark current is in the range of $1\,\mathrm{nA}$ and, therefore, orders of magnitude smaller than practical $i_{pc,0}$ values. Hence, the photocurrent shot noise $\overline{i_0^2}$ linearly increases with $F(\nu)A_b$, the input photon flux. The photocurrent noise levels were converted with G = 10^4 V/A to the measured voltage signal V_0, yielding a noise voltage power spectral density (PSD) $S_V = \overline{V_0^2}/\Delta f = G^2 \cdot S_i$ where Δf is the bandwidth of the system and S_i is the current noise power spectral density. Fig. 3.45 reveals the noise voltage power spectral denisty values calculated out of [noise measurements with a lock-in amplifier]of the sensor's output relative to the generated photocurrent.

Furthermore, the current noise power spectral density can be expressed as $S_i = \overline{i_0^2}/\Delta f$ resulting in the photocurrent noise $\overline{i_0^2} = \overline{V_0^2}/G^2$ [74].

Fig. 3.46 shows the noise measurement in relation to the transparent aperture cross section area A_{eff}. The deviation at smaller values of A_{eff} is again primarily due to stray light, diffraction and pattern separation. The calculated [fit] exhibits the predicted noise [characteristic] proportional to A_{eff}."[47]

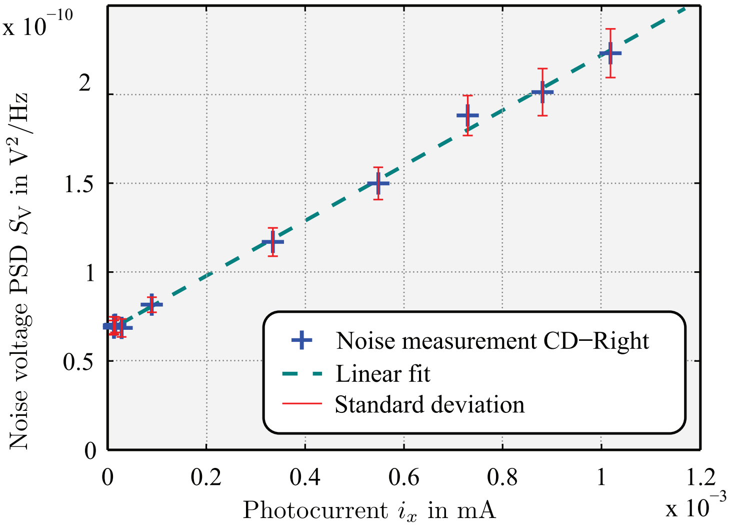

Figure 3.45: Noise measurement results over the photocurrent i_x resulting from the increasing voltage at combdrive CD-Right. The data reveals a predominant photocurrent noise. The error bars represent the standard deviation of the measured noise values.[47]

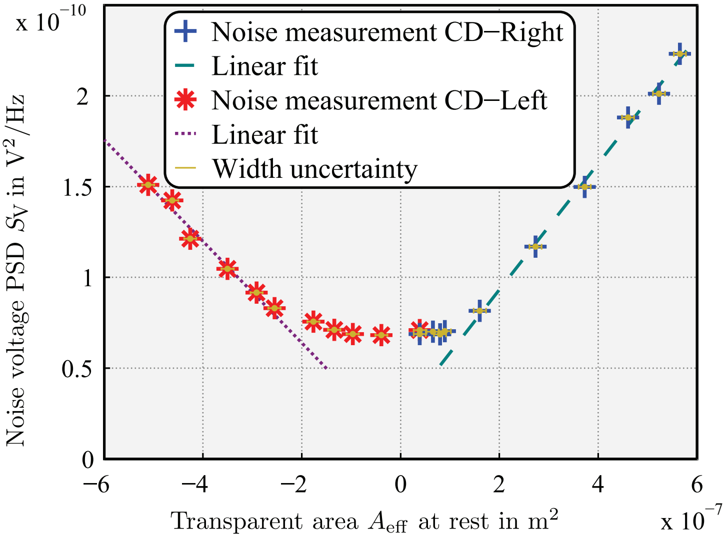

Figure 3.46: Noise voltage PSD over A_{eff} at rest deviates for small values of A_{eff} from the prediction deduced from Eq. 2.32 and Eq. 2.34 primarily due to stray light, diffraction and pattern separation. Negative area values indicate the use of the combdrive 'CD-Left'. The error bars represent the uncertainty of the aperture dimension estimates.[47]

3.6 Summary

In this chapter the MOEMS sensor design, its fabrication and the resulting sensor characteristics discussed. Solutions for the aperture misalignment errors caused by the wafer bonding process and the influence of the underetching on the sensor transfer characteristics was discussed. Additional simplification of the fabrication can be achieved by using infrared light and metal apertures without etching openings into silicon. This approach was exemplified by prototype measurements revealing a larger scope for the design of the seismic mass and the damping behavior of the MOEMS sensors.

A variety of sensors with different sensitivities and a variation of resonance frequencies were discussed together with the impact of the sensor- and aperture-shape on the noise equivalent displacement and the damping. It was shown, that with the MOEMS sensor design it is easily possible to reach the thermo-mechanical noise floor. The results show an outstanding sensor performance regarding displacement sensitivity with a resolution of sub-picometer. The limitations regarding nonuniform illumination, a result from the hybrid sensor set-up, utilizing SMD opto-electronics were also pointed out.

Chapter 4

Aperture Design Based on Deconvolution

This chapter addresses various analytical and numerical methods for calculating the output transfer function of a pair of apertures. Moreover, it describes methods for designing aperture shapes that provide desired transfer characteristics. To start, the fabrication limitations for aperture design in microtechnology and some new approaches utilizing display and CCD-chip technology are discussed. Next, the computation of the output transfer function regarding the in-plane deflection of the apertures in 1D and 2D are discussed. A 1D transfer characteristics must be selected and designed if the vibration sensor should be sensitive in only one axis. Subsequently the shape of the aperture is called form function or aperture shape function in the context of their mathematical treatment.

All apertures designed for a 1D transfer function also feature a 2D aspect. One dimension is due to the deflection dependency and the second determines the magnitude at a certain deflection. A 2D transfer characteristic on the other hand is based on 2D aperture shapes which will generally appear different from the 1D approach. This is due to a true dependence on both axes positions. When considering multiple, semitransparent layers for fabricating the apertures or openings it is also possible to further extend the design scope.

The first approach for computing the output transfer function utilizes the analytical convolution operation [75, 76] which is (for the envisioned application) only valid for normalized and non-negative aperture form functions. Normally, the convolution-operation is computed for time dependent signals, which were also examined in frequency-domain with the Fourier transform. Two examples of analytical convolution are explained in detail to demonstrate the difficulties in finding closed-form solutions. In the discussed deflection related aperture design, equivalent transformations are used to convert functions from the 'deflection dependent' domain into the 'spatial frequency' domain and vice versa. The limitations of this approach are analytically exemplified.

The second approach is much more helpful for the design process. It utilizes a custom numerical calculation which also enables the computation of the 'inverse' problem of designing the aperture shape starting with the transfer characteristic as input information. Three examples are shown where one form function is computed from the transfer characteristic and the defined second form function.

Finally, examples of the 2D convolution and solving the inverse problem (deconvolution) are also discussed, stating the restrictions and limitations of the aperture calculation. Additionally, the influence on the time-dependent in- and output signals will be demonstrated by the calculated deflection dependent output characteristic.

Parts of this chapter were already discussed in [41] and are in quotation marks.

4.1 Fabrication Limitations for Micromechanical Apertures

This subsection deals with the constraints for the aperture design arising from the fabrication processes. Corners and kinks in the shape of the apertures can arise during the design process, which is usually done using analytical methods or computer aided design tools. Such discontinuous form functions will be avoided later on, although it is possible to calculate or process them analytically. Each kink in the shape will become rounded after being processed in microfabrication. This is due to limitations of the lithographical shape mapping into the resist and also the shape transfer limitations of the etching processes. Manufacturing the geometries in other microtechnology processes like lift-off [19] provides much better contour accuracy but still do not allow sharp corners in the shape because of the above mentioned shape transfer restrictions. Examples of both fabrication techniques can be seen in Fig. 4.1. The processed structures should be as rigid as possible and feature details should not be smaller than the a critical size. Otherwise, the geometries will not be mapped on the MEMS structures. When fabricating the apertures as openings inside a silicon layer, the thickness of the layer also has an effect on the resulting radius of the roundings. In general, a thick silicon layer leads to increased roundings.

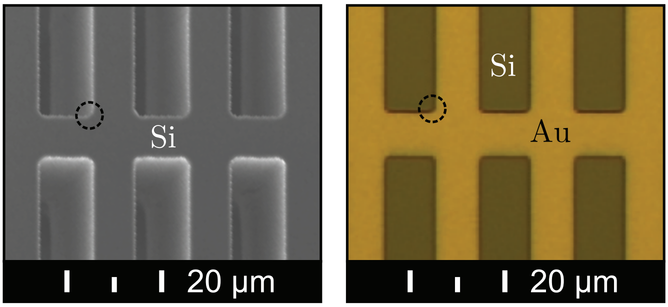

(a) **(b)**

Figure 4.1: A SEM micrograph and a conventional micrograph of two microstructures with a) openings etched into silicon and b) a metal lift-off layer on top of silicon. Exemplary roundings are highlighted in the corners due to limitations of the lithography and fabrication.

When fabricating the apertures in microtechnology, further constraints arising from processing the MEMS have to be considered. Inside a silicon layer, apertures can only be fabricated as openings (Fig. 4.1 a). Metal layers on glass or silicon on the other side can feature more than one layer but their shape is limited to the surface of the substrate. Therefore, the metal layer on a movable mass can't become larger than the mass itself. An example of a metal layer on top of silicon can be seen in Fig. 4.1 b.

4.1.1 Grayscale Apertures and Multi Wavelength Measurement

Different metal layers which vary in thickness and shape yield to a third degree of freedom for designing the apertures. This type of aperture still can be computed using the two dimensional convolution operation which is discussed in detail in section 4.5. The light flux through two partially 'gray'-shaded apertures is calculated by multiplying the pixel area with the 'gray'-value. An exemplary aperture with at least two layers of different transparency is depicted in Fig. 4.2 in the lower right part of the figure. When computing the 2D convolution, semi-transparent areas must be properly weighted. The exemplary corresponding values are also listed.

In general it would also be possible to apply different optical filters for light with different wavelengths. This would provide more than one output transfer characteristic at the same time but with a single aperture design

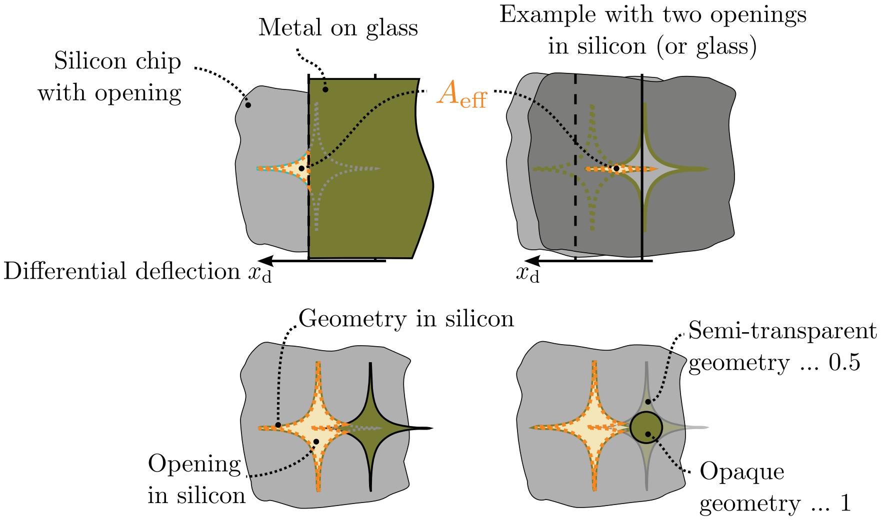

Figure 4.2: Aperture form examples: In the upper left, one aperture is fabricated as an opening into silicon and the second as an opaque layer on a transparent wafer (e.g., gold on glass). The upper right graphic illustrates a hole hole pair. The lower two figures depict the capability of giving both apertures arbitrary shapes and additional (lower right) use several semi-transparent metal layers to offer additionally design space. The exemplary corresponding values for 2D convolution are also listed.

on the moving mass. This would imply several receiver for different wavelengths at a certain area which could be achieved for instance with a color CCD chip. Recent pixel sizes of a commercial phone camera decreased to 1.12 µm [77, 78] indicating the possible spatial resolution for a shape function.

Furthermore, replacing the light source and the fixed aperture by a light emitter with a well defined shape as demonstrated in [79] or utilizing a display technology [80] to dynamically adopt one of the apertures would increase the degrees of freedom extraordinarily. Display technology would give access to light of different wavelengths which could be specified separately for each pixel. This is comparable with implementing several dynamic apertures around one static MEMS-aperture.

In this work only the basic aperture design rules were discussed because for more than one pair of apertures or dynamically modified apertures the same methods have to be applied but treated separately.

4.2 Computation of 1D Convolution

"Considering the case of two apertures with a maximum elongation in positive y-direction of 1 (Fig. 4.3) where each form-function is exactly 1 over the complete deflection range in x. The overlapping area A_{ol} of both apertures can [then] be calculated by a 1D convolution

$$A_{\mathrm{ol}}(x) = h(x) = 2\cdot(f_{\mathrm{Cr}}(x) * g_{\mathrm{Si}}(x)) = 2\cdot \int\limits_{-\infty}^{+\infty} f_{\mathrm{Cr}}(\xi)\cdot g_{\mathrm{Si}}(x-\xi)\mathrm{d}\xi, \quad (4.1)$$

where $f_{\mathrm{Cr}}(x)$ and $g_{\mathrm{Si}}(x)$ are the aperture related form functions, describing their geometrical change in the y-direction along the x-axis. Examples of typical form functions are shown in the upper right Fig. 4.3. Due to the symmetry of the considered geometries with respect to the x-axis, the form functions characterize just the part of the aperture where the spatially coordinate y is positive. The factor 2 in Eq. 4.1 arises from calculating the complete areas, including the negative part of the y-axis (see lower left part of Fig. 4.3). The approach [presented] is only valid if the geometries are mirror-symmetrical to the x-axis. Additional examples of aperture [pair combinations] and their resulting output transfer function can be found in Fig. 4.2."[41]

The main limitation concerning the correctness of the calculation is that the convolution integrates the product of both form functions. Let us con-

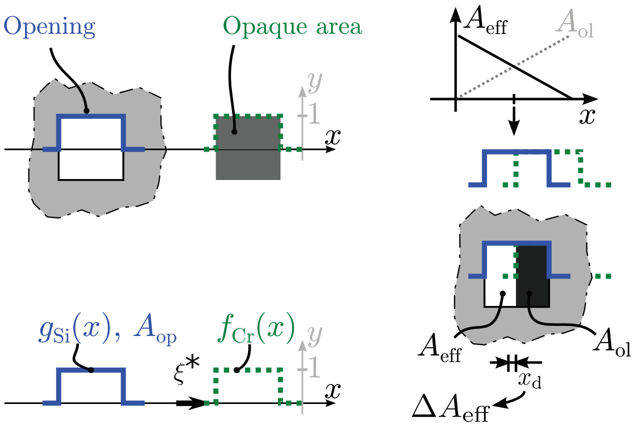

Figure 4.3: Schematic of the convolution process and definition of all representative areas affecting the output characteristics. As an example, an opening geometry fabricated into silicon and a metal geometry vapor deposited are depicted. Filled sections represent areas which are intransparent.

sider two openings at a certain point x. Only the smaller value of both form functions counts for the calculation (see left part of Fig. 4.4). Therefore, the 1D convolution operation is only correct as long as one aperture is always normalized with values 1 and the other is smaller than 1. Another constraint related to the convolution operation is that the form-function values of f_{Cr} and g_{Si} are for the usage as form functions not allowed to be negative. Never the less, the 1D convolution operation is a true aid for dealing with simple aperture design problems.

A special case for the design arises when both parallel aligned apertures are rectangularly shaped and the effective edge length $l_{\mathrm{e}} = g(x) = f(x)$ remains constant across the whole deflection range. Then, the change in effective (open) area can be calculated by $\Delta A_{\mathrm{eff}} = x_{\mathrm{d}} \cdot l_{\mathrm{e}}$ (Fig. 4.3) where x_{d} is the differential deflection between the apertures in x. "This is not generally valid for arbitrarily shaped grating pairs, where the effective area of the apertures can be obtained from

$$A_{\mathrm{eff}}(x) = A_{\mathrm{op}} - A_{\mathrm{ol}}(x) \quad . \tag{4.2}$$

where A_{op} is the area of the opening, e.g., manufactured in silicon and A_{ol} is the overlapping area of the appropriate apertures. If the Cr aperture is also

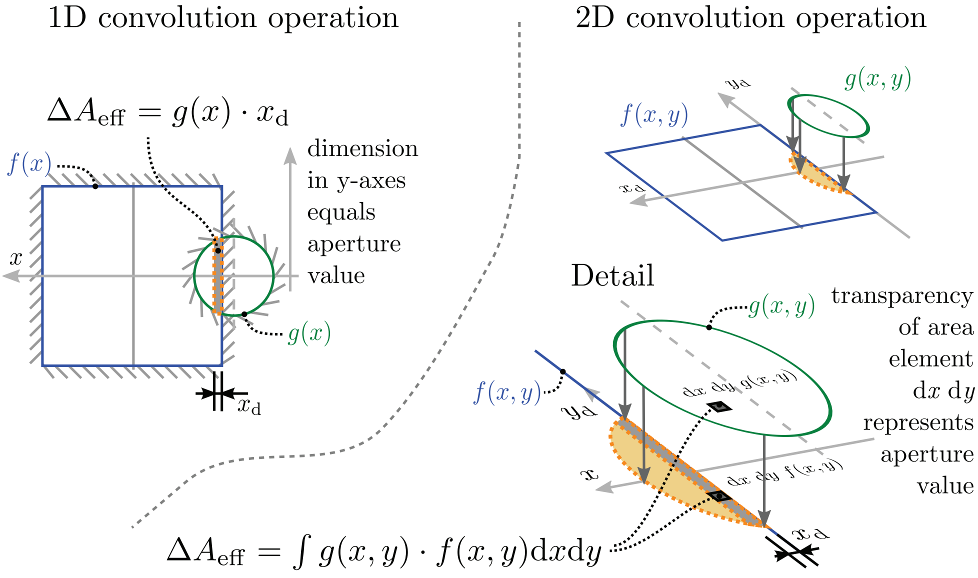

Figure 4.4: Illustration of the principal differences between 1D and 2D convolution with the calculation of the differential change in effective transparent area ΔA_{eff}. The form functions shown describe openings in an otherwise transparent layer and are therefore, only partially transparent inside.

fabricated in the form of an optical transparent opening (compare upper right of Fig. 4.2), the subtraction is not necessary and $A_{\text{eff}} = A_{\text{ol}}$."[41]

4.2.1 Examples for Analytical Convolution Calculation

The following subsection deals with computation examples for convolution of predefined shape functions like $\text{rect}(x)$ and $\exp(x)$. This should also demonstrate the emerging effort for basic shape functions which are still computed without roundings which would increase the order of complexity. In the subsequent calculations, the constant factor of 2 from the prior symmetry considerations is dropped because we concentrate on the basic analytical convolution operation of the upper half plane.

Triangle-transfer-function

Assuming that $g(\xi) = \text{rect}(\frac{\xi}{l})$ and $f(\xi) = \text{rect}(\frac{\xi}{l})$, the output transfer function $h(x)$ has to be calculated for different regions of x. A schematic of the convolution operation can be seen in Fig. 4.5.

First region: $x + {}^{l}\!/\!{}_{2} \leq -{}^{l}\!/\!{}_{2} \rightarrow \qquad x \leq -l$

$$h(x) = 0 \tag{4.3}$$

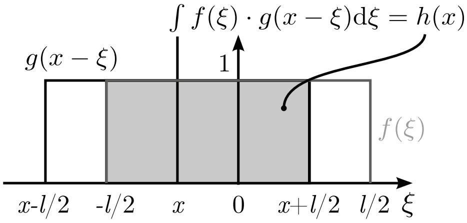

Figure 4.5: Illustration of both form functions in the second subregion and the overlapping area computed the convolution.

Second region: $x + {}^{l}\!/\!{}_{2} \leq {}^{l}\!/\!{}_{2} \rightarrow \qquad -l \leq x \leq 0$

$$h(x) = \int_{-l/2}^{x+l/2} \mathrm{d}\xi = \xi\Big|_{-l/2}^{x+l/2} = x + {}^{l}\!/\!{}_{2} + {}^{l}\!/\!{}_{2} = x + l \tag{4.4}$$

This result can be proven for $x = -l \rightarrow h(x) = 0$ and for $x = 0 \rightarrow A(x) = l$.

Third region: $x - {}^{l}\!/\!{}_{2} \leq {}^{l}\!/\!{}_{2} \rightarrow \qquad 0 \leq x \leq l$

$$h(x) = \int_{x-l/2}^{l/2} \mathrm{d}\xi = \xi\Big|_{x-l/2}^{l/2} = {}^{l}\!/\!{}_{2} - (x - {}^{l}\!/\!{}_{2}) = l - x \tag{4.5}$$

This result can be proven for $x = 0 \rightarrow h(x) = l$ and for $x = l \rightarrow h(x) = 0$.

Forth region: $x - {}^{l}\!/\!{}_{2} \geq {}^{l}\!/\!{}_{2} \rightarrow \qquad x \geq l$

$$h(x) = 0 \tag{4.6}$$

The above can be summarized as

$$h(x) = \begin{cases} 0 & , x \leq -l \\ l + x & , -l \leq x \leq 0 \\ l - x & , 0 \leq x \leq l \\ 0 & , x \geq l \end{cases} \tag{4.7}$$

and with the help of the rect function the output transfer function can be written as $h(x) = (l - |x|)\,\mathrm{rect}(\frac{x}{2l})$.

Exponential-function

Assuming that $g(\xi) = \mathrm{rect}(\frac{\xi}{l})$ and $f(\xi) = e^{-\alpha|\xi|}\mathrm{rect}(\frac{\xi}{l})$ the output transfer function $h(x)$ has to be calculated for different value regions of x. A schematic of the convolution operation can be seen in Fig. 4.6.

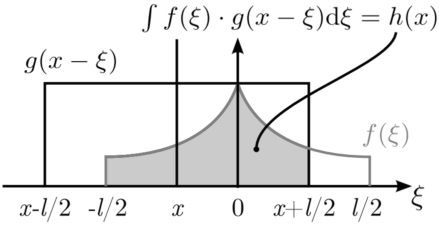

Figure 4.6: Illustration of both form functions in the first subregion and the overlapping area computed during the convolution.

First region: $0 \leq |x| \leq l/2$

$$h(x) = \int_{x-l/2}^{x} e^{\alpha\xi}\,\mathrm{d}\xi + \int_{x}^{l/2} e^{-\alpha\xi}\,\mathrm{d}\xi = \left.\frac{e^{\alpha\xi}}{\alpha}\right|_{x-l/2}^{x} + \left.\frac{e^{-\alpha\xi}}{-\alpha}\right|_{x}^{l/2} =$$

$$= \frac{e^{\alpha x} - e^{\alpha(x-l/2)}}{\alpha} + \frac{e^{-\alpha x} - e^{-\alpha l/2}}{\alpha} \tag{4.8}$$

Second region: $x_g - l/2 < l/2 \rightarrow x \leq l \rightarrow \qquad l/2 \leq x \leq l$

$$h(x) = \int_{x-l/2}^{l/2} e^{\alpha\xi}\,\mathrm{d}\xi = \left.\frac{e^{\alpha\xi}}{\alpha}\right|_{x-l/2}^{l/2} = \frac{e^{\alpha l/2} - e^{\alpha(x-l/2)}}{\alpha} \tag{4.9}$$

Third region: $x_g - l/2 \geq l/2 \rightarrow x_g \geq l \rightarrow \qquad x \geq l$ (no overlapping)

$$h(x) = 0 \tag{4.10}$$

The above can be summarized as

$$h(x) = \begin{cases} \frac{e^{\alpha|x|} - e^{\alpha(|x|-l/2)} + e^{-\alpha|x|} - e^{-\alpha l/2}}{\alpha} & , 0 \leq |x| \leq l/2 \\ \frac{e^{\alpha l/2} - e^{\alpha(|x|-l/2)}}{\alpha} & , l/2 \leq |x| \leq l \\ 0 & , |x| \geq l \end{cases} \tag{4.11}$$

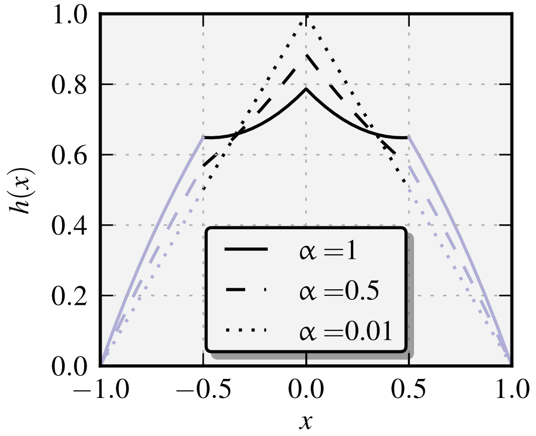

Figure 4.7: Illustration of the found result $h(x)$ for different values of α and $l = 1$. For small values of $\alpha \rightarrow 0$ the result changes over to the case of two $\mathrm{rect}(\frac{\xi}{l})$ with length of 1. The different colors indicate the two regions of the analytically derived solution $0 \leq |x| \leq {}^{l}\!/_{2}$ and ${}^{l}\!/_{2} \leq |x| \leq l$.

This overview demonstrates by means of the example of an exponential function as input it is not easily possible to give a closed-form expression. Therefore, the deconvolution operation becomes more ambitious because of the different regions to consider.

4.3 One Dimensional Deconvolution Examples and Limitations

4.3.1 Fredholm Integral Theory

For partially continuous form- and output transfer functions, it is possible to solve the inverse problem starting with the transfer characteristics and compute one of the two form-functions. The necessary analytical theory is known as Fredholm theory, [75] which will be discussed briefly. This theory covers in general all integral equations like Fourier- or Laplace-integral equations which only differ in the form of their kernel function $K(x, s)$. The inhomogeneous Fredholm integral equation of first kind can be generally written as

$$h(x) = \int_a^b K(x, s)\, g(s)\, \mathrm{d}s \quad . \tag{4.12}$$

Here is $g(x)$ the given output transfer function. The kernel function $K(x, s)$ which can be substituted with $f(s)$ represents the unknown form function. If the limits of the integration are ±∞ and $K(x, s) = K(x - s) = f(x - s)$ then a solution for f can be expressed as

$$f(x) = \mathcal{F}_{\omega}^{-1}\left[\frac{\mathcal{F}_x\left[h(x)\right](\omega)}{\mathcal{F}_x\left[g(x)\right](\omega)}\right] = \int_{-\infty}^{\infty}\frac{\mathcal{F}_x\left[h(x)\right](\omega)}{\mathcal{F}_x\left[g(x)\right](\omega)}e^{2\pi i\omega x}\mathrm{d}\omega \quad , \tag{4.13}$$

where $\mathcal{F}_x$ and $\mathcal{F}_{\omega}^{-1}$are the direct and inverse Fourier transforms, respectively. Basically, the described operation is an inverse transformation after dividing the computed dependencies in the spatial frequency domain. For precise definitions of the terms used see [75].

Finding the above described solution analytically for a piecewise continuous function can be extraordinarily complex or even impossible. Examples for the above described division of spectra in frequency domain can be found in section 4.3.4. Therefore, the usage of numerical methods for solving the inverse problem, respectively calculating one or both form-function out of the desired transfer characteristic is a more promising and comfortable alternative.

The subsequently used mathematical methods are in general known as deconvolution, the process to reverse the effects of convolution. For more precise definitions of the terms used see [75, 81, 82].

For the following considerations, it is assumed that the requested output transfer function $h(x) = A_{\mathrm{eff}}(x)$ is given. Two different methods to determine one or both shape functions $g(x)$ and $f(x)$ are discussed. These methods will be referred to as division-method and sqrt-method, respectively. Both approaches use the convolution theorem as starting point whereby the convolution operation in ’deflection’-domain results in a frequency domain multiplication of the Fourier-transfered spectra which can be expressed as follows

$$\begin{aligned} f(x) * g(x) &= h(x) \\ \mathcal{F}_t\left\{f(x) * g(x)\right\} &= \mathcal{F}_t\left\{h(x)\right\} \\ F(\omega)\cdot G(\omega) &= H(\omega) \quad . \end{aligned} \tag{4.14}$$

With this representation it is possible to compute $f(x)$ and/or $g(x)$ as described in the following two subsections.

4.3.2 Division in the Frequency Domain

In the case of one given aperture shape function, for instance $g(x)$, the second one can be computed using the following operation

$$f_{div}(x) = f(x) = \mathcal{F}_\omega^{-1}\left\{F(\omega)\right\} = \mathcal{F}_\omega^{-1}\left\{H(\omega)/G(\omega)\right\} \quad . \tag{4.15}$$

The spectra of the requested transfer function and $g(x)$ are divided in frequency domain and inverse Fourier-transfered. This operation is possible as long as $G(\omega)$ does not contain any zero value hence no division by zero occurs. Examples of this operation on different output and aperture form functions are depicted in the left part of Fig. 4.8, 4.9 and 4.10. For all three examples $g(x)$ was predefined as a rectangular shaped form function. The output transfer function is always depicted in the lower right of the figures. The examples are discussed in detail in section 4.3.4 after presenting the Fourier transform related deconvolution operation.

4.3.3 Square Root in Frequency Domain

If neither of the two form functions is known, then by symmetrical assumption $f(x)$ can be computed by calculating the square root in the frequency domain as obtained from Eq. 4.16 yielding $f_{\mathrm{sqrt}}(x)$ after inverse Fourier transformation. This method will be referred to as sqrt-method.

$$\begin{aligned} f_{\mathrm{sqrt}}(x) * f_{\mathrm{sqrt}}(x) &= h(x) \\ \mathcal{F}_\omega^{-1}\left\{F_{\mathrm{sqrt}}(\omega)^2\right\} &= \mathcal{F}_\omega^{-1}\left\{H(\omega)\right\} \\ f_{\mathrm{sqrt}}(x) &= \mathcal{F}_\omega^{-1}\left\{|F(\omega)|\right\} = \mathcal{F}_\omega^{-1}\left\{\sqrt{H(\omega)}\right\} \end{aligned} \tag{4.16}$$

In the following subsection three examples (Fig. 4.8, 4.9 and 4.10) are discussed demonstrating advantages as well as limitations of both methods.

4.3.4 Examples of Deconvolution in Frequency Domain

Three different output transfer functions will be identified with the previous described division and sqrt-method. All three output functions in the chosen examples are even functions but they do not have to be in general.

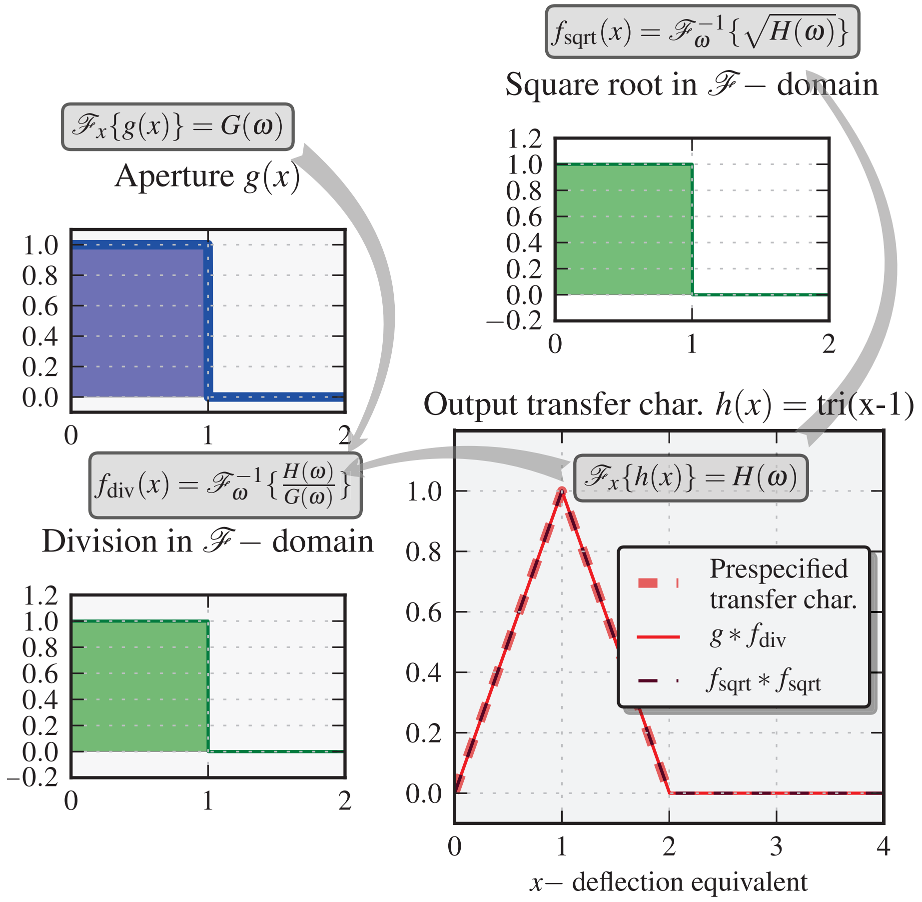

Figure 4.8: Deconvolution by division (left half) or square root extraction in frequency domain on the example of a triangular shaped output transfer function. Both methods compute the correct form function $\text{rect}(x)$. Filled areas correspond with positive function values which represent transparent areas.

As Fig. 4.8 illustrates, the sqrt-method works well for simple output functions like the shown triangular shaped output transfer function $\text{tri}(x-1)$. The output transfer function reaches 1 at a $x-$deflection of 1 which is the result of the convolution integral of 1 $x-$steps with the function value of 1. The division method can be applied here as well since the Fourier transform of a triangle is a squared $\text{sinc}(f) = \sin(f)/f$ function with periodic zero values at multiples of $^{\pi}/_{2}$ which are also valid for the transformed rectangular-function represented by an ordinary $\text{sinc}(f)$. The division yields a $\text{sinc}(f)$

which results in a rectangular function when the inverse Fourier transfers it into the 'deflection' domain.

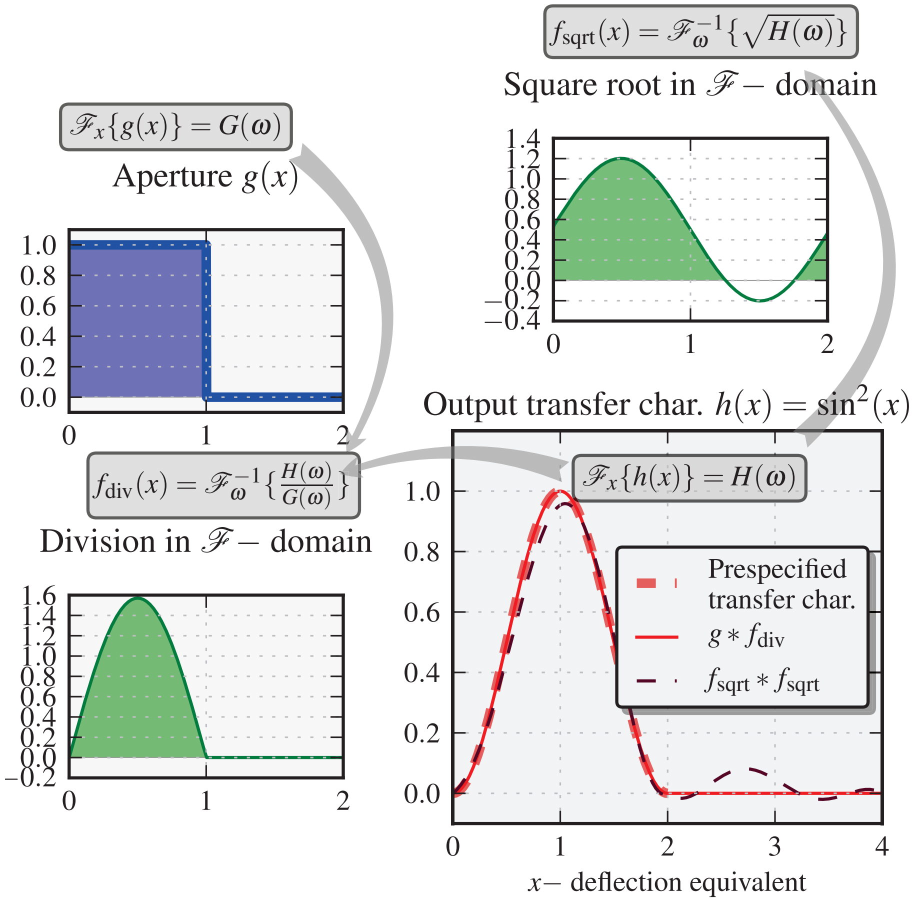

Figure 4.9: Deconvolution by division (left half part of the figure) or square root extraction in frequency domain on the example of a $\sin^2(x)$ shaped output transfer function. The division method computes the correct form function. The sqrt-approach yield negative values in the form function f_{sqrt} and the convolution result does even with negative values not match the desired output function. Filled areas correspond with positive function values which represent transparent areas.

The two procedures are discussed with the help of diagrams as like that in Fig. 4.8. The diagram in the lower right part of the figure shows the desired output transfer function $h(x)$ as well as the validated convolution result after computing the determined aperture form functions. The left part of the figure illustrates the division method utilizing a prespecified aperture shape function $g(x)$. The result of the sqrt-method is finally illustrated in the upper right part of the figure. All three examples are computed numerically resulting in the introduction of a discretization of the x-axis. Figure 4.9 depicts the equivalent example for an output function of $\sin^2(x) = 1 - {}^1\!/_2 \cos(2\,x)$.

The zero values of the Fourier transformed rect-function $G(\omega)$ lead to a division by zero thus finding a solution is not possible in the first run. To overcome this problem small even by randomly distributed values are added to the spectrum of $g(x)$. Hence, the computation of the second form function $f_{\text{div}}(x)$ is possible. The result can be seen in the lower left of Fig. 4.9.

In case of calculating the square root of the output transfer function in frequency domain the resulting shape function differs from the first approach. The form function f_{div} also exhibits negative values. When testing the computed result and convolving $f_{\text{sqrt}} * f_{\text{sqrt}}$ the outcome does not fit the requested output function perfectly, which is again due to loss of phase information during the square root calculation.

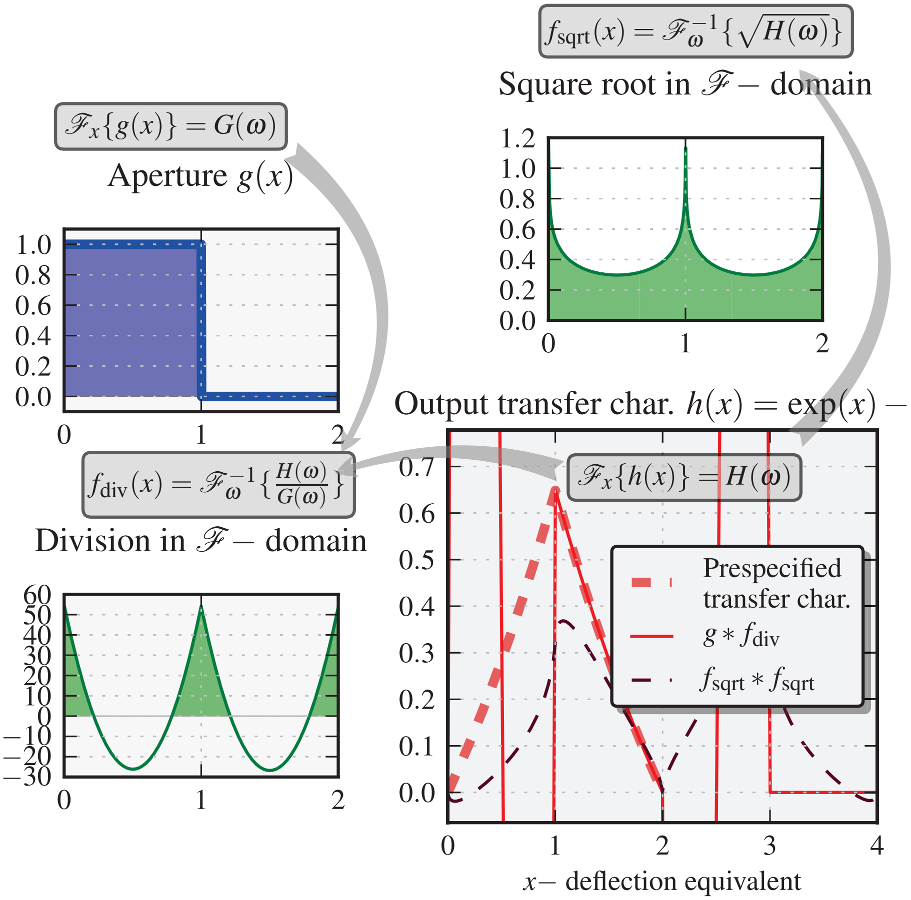

Figure 4.10: Deconvolution by division (left half part of the figure) or square root extraction in frequency domain on the example of a symmetric $\exp(x) - 1$ shaped output transfer function. The division-methods computes a partially negative form function which produces the requested output transfer function only in a short deflection range of x between 1 and 2. Outside of this region the deviations are significant and not negligible. The sqrt-approach and the div-approach yield completely inappropriate results. Shaded areas correspond with positive function values which represent transparent areas.

4.4 Custom Numerical Computation for 1D Problems

With the subsequently presented numerical approach it is possible to calculate the form of the aperture pairs from an arbitrary prespecified transfer characteristic. The output function is not restricted to symmetry or continuity. The discussed procedure takes into account that the smaller transparent aperture dimension influences the output signal. Furthermore, it is much easier to calculate the characteristics of discontinuous form functions which is in principle analytically possible but would lead to several more difficult sub-problems. An other strength of the numerical approach is the possibility to alter both aperture geometries to achieve the desired output transfer characteristic.

The complete calculation is done in the deflection-domain. It is run through a loop which gradually calculates the unknown form function values. The output transfer function and one form function $g(x)$ have to be predefined.

Algorithmus 1 The simplified first steps of the numerical procedure for calculating the second form function. Assuming that the first form function is always greater.

```
r = ( h(2) - h(1) ) / x_step      # calculating first differential value
if r > 0 then                     # r is positive
  f(1) = r                        # setting first value of f
else                              # r is negative
  g(1) = g(1) + r                 # subtracting negative r of first g value
r = ( h(3) - h(2) ) /x_step       # calculating second differential value
if r > 0 then                     # r is positive
  f(2)= r                         # setting second value of f
else                              # r is negative
  g(2) = g(2) + r                 # subtracting negative r of second g value
...
```

If necessary, the predefined form function $g(x)$ is also modified due to resulting negative values for $f(x)$. As long as the second aperture does not have to be modified the resulting operation is equal to a differentiation of $h(x)$. Which can be easily seen on the example in Fig. 4.11 where $h(x) = \exp(x) - 1$ and the resulting $f_{\text{calc}} = \exp(x)$. The figure also contains a plot where both form-functions feature rounded edges to be representative for fabricable geometries. The outcome of the aperture shift operation $h_{\text{calc}}(x)$ is also shown next to the prespecified output transfer function. The deviations are due to the missing area cut away from the inserted rounding at $x = 0$. Figure 4.12 depicts results for a logarithmic output transfer func-

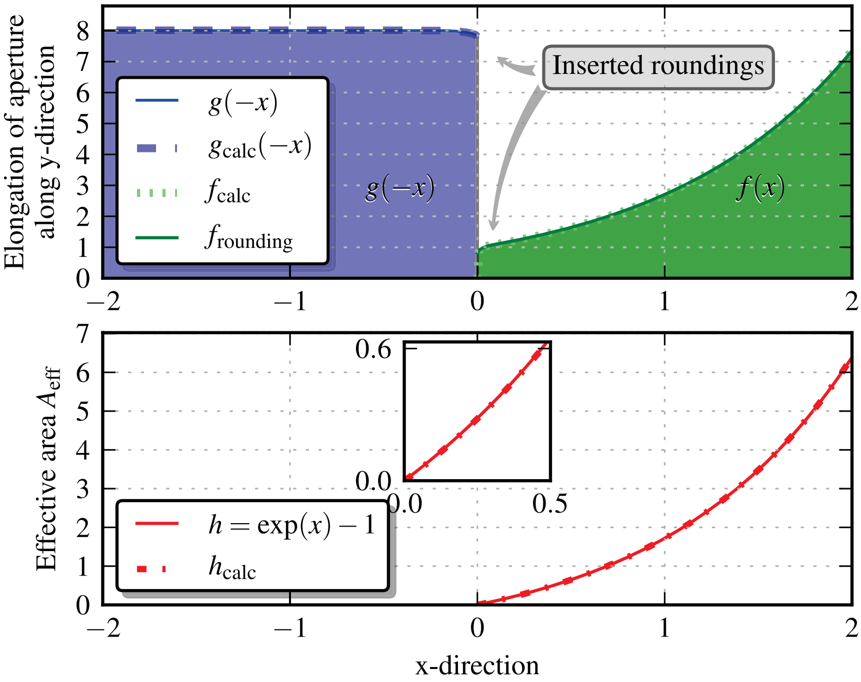

Figure 4.11: Exponential output transfer function: The upper plot depicts the prespecified aperture $g(x)$ together with the computed one $f(x)$. Filled areas depicted transparent areas. The desired output transfer function is depicted in the lower plot along with the finally computed convolution result taking roundings at the apertures into account. The inset reveals good agreement also for smaller values of x.

tion where the run of the resulting transfer-function is parallel to $\log(x+1)$. The decreased values are due to the rounding of the f-form function resulting in a reduction of overlapping area. Equivalent offset-affected for the $\sqrt{x}$ transfer-function are depicted in Fig. 4.13. To overcome the offset the rest position for the sensor must be shifted by the corresponding x-offset to the right. The three examples demonstrate, that it is easily possible to gener-

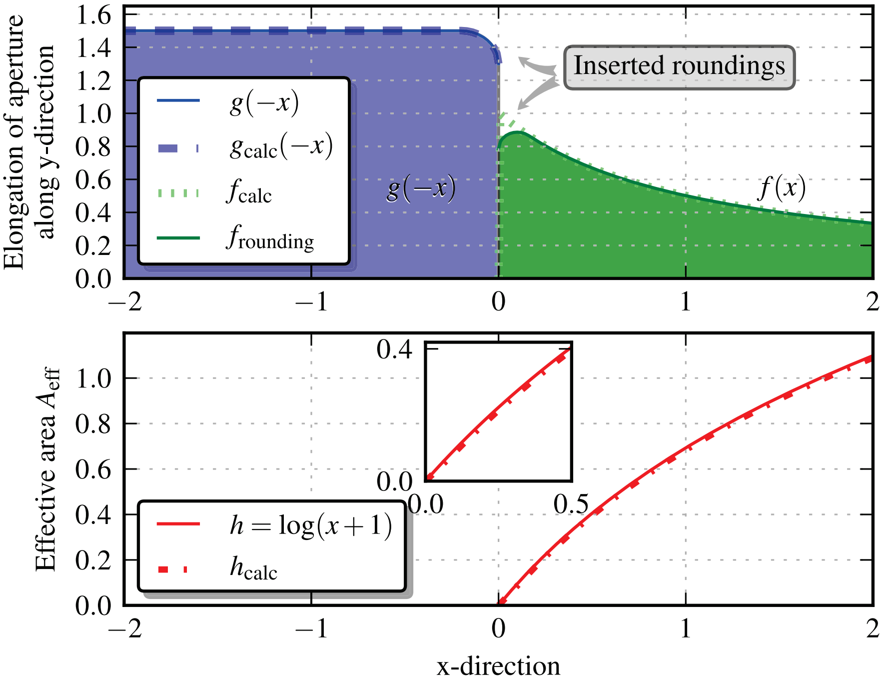

Figure 4.12: Logarithmic output transfer function: The upper plot depicts the prespecified aperture $g(x)$ together with the computed one $f(x)$. Filled areas illustrate transparent regions. The desired output transfer function is depicted in the lower plot along with the finally computed convolution result taking roundings at the apertures into account. The inset reveals good agreement also for smaller values of x.

ate the desired output transfer function with the proposed procedure and to consider simultaneously fabrication specific details like roundings.

The procedure described above is also valid for the square-root operation which is needed to linearize e.g., the quadratic transfer function of a MEMS combdrive.

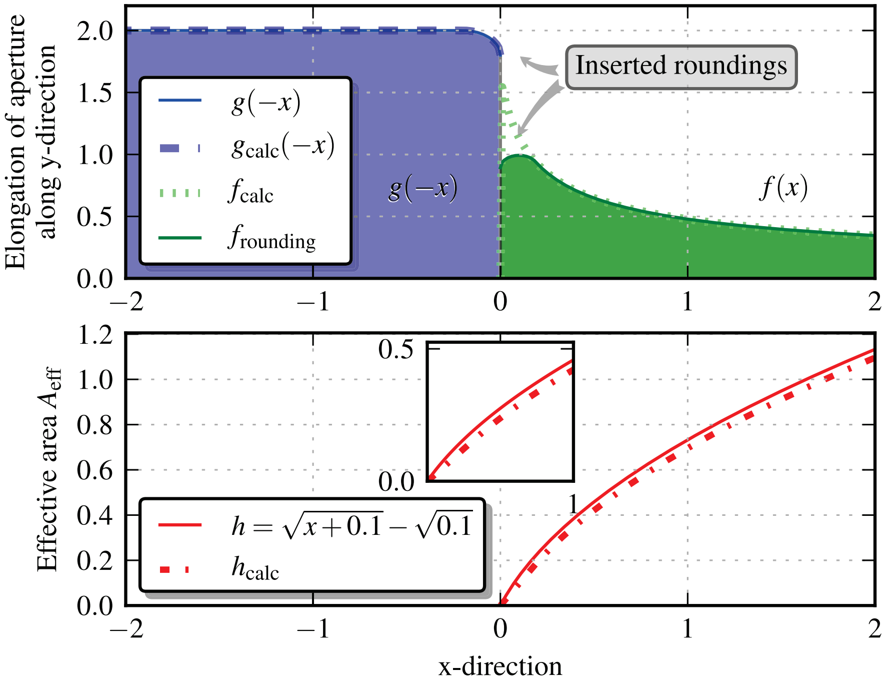

Figure 4.13: Output transfer function $\sqrt{x}$: The upper plot depicts the prespecified aperture $g(x)$ together with the computed one i.e., $f(x)$. Filled areas illustrate transparent areas. The desired output transfer function is depicted in the lower plot along with the finally computed convolution result taking roundings at the apertures into account.

4.5 Two Dimensional Convolution

Compared to the 1D convolution, the usage of the two-dimensional convolution operation is a more powerful approach which has to be applied to the form functions depending on the spatial coordinates x and y. The previous 1D convolution can be interpreted as a special case of the 2D convolution where the results were only considered for relative movements along one coordinate axis. An illustration of both cases can be found in Fig. 4.4. Accordingly the 2D convolution separates the spatial dimension of the aperture and the function value at a certain spatial point. Multiplying the function values inside the convolution integral is required to determine the output operation in 2D. This is especially interesting because 2D apertures can also feature more than the values between 0 and 1 representing a semitransparent property.

The following two sections will deal with the 2D convolution examples, the resulting output transfer functions and their effects on time dependent deflection signals.

4.5.1 Numerical Computation of 2D Convolution

"Figure. 4.14 exhibits the results of a two dimensional convolution which was numerically computed. The upper two axes in Fig. 4.14 display the 2D form-functions which do not have to be [symmetric]. The white regions represent the transparent areas of the apertures. The aperture depicted in the upper left axes is therefore [completely] transparent inside [a] given region while the second aperture shown in the upper right plot is only transparent in the star-shaped region in the middle. The outside of the apertures has to be considered as black (non-transparent) and the lower right plot illustrates the result of the 2D convolution of $g(x, y)$ and $f(x, y)$. This result indicates when the output changes in relation to the deflection in x and y. Symmetry of both apertures along x and y results in an also symmetric output transfer function. The plot in the lower left shows also the output characteristic along the x-axis at $y = 0$. The output is zero as long as the edge of the square of $g(x, y)$ does not touch the star geometry of $f(x, y)$. The complete resulting characteristic can be seen in the lower left of Fig. 4.14 as dashed red line. The second run depicted in this plot indicates the output characteristic when using [an] inverted $f(x, y)$ aperture. Additional examples of possible output characteristics $A_{\text{eff}}(x)$ can be found in Fig. 4.15."[41]

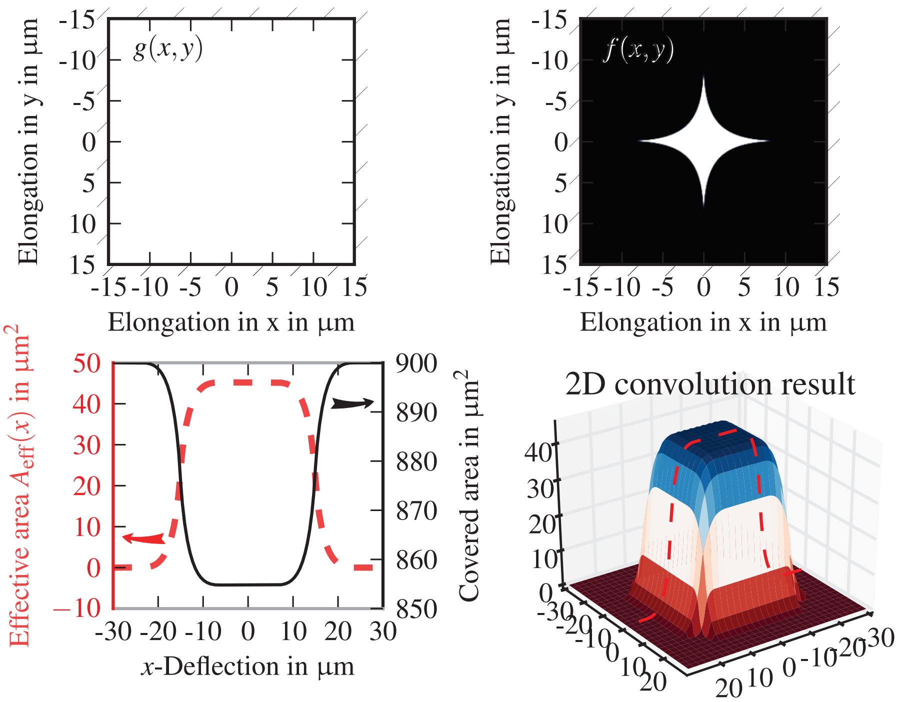

Figure 4.14: Example of the 2D convolution of two 2D binary valued apertures (upper diagrams where white indicates transparent areas). The result of the convolution is depicted in the lower right plot. For a relative deflection of the apertures in $x-$direction only, the output characteristic shown in the lower left plot is achieved. This characteristic corresponds to the values along the red dashed line in the lower left plot.

"Rectangular openings in silicon and in the chromium aperture yield to a linear characteristic, as long as the aperture is not completely covered or fully transparent which occurs with multiples of the pitch period. Starting with a completely uncovered opening, A_{eff} is linear decreasing with x. At the point of x where the apertures become fully intransparent, A_{eff} increases again [in a linear manner]. The two linear regions for opening or closing the apertures are connected by discontinuity points in $A_{\mathrm{eff}}(x)$, making it much more complicated to analytically calculate time signals of $A_{\mathrm{eff}}(x)$. Therefore, the demonstrated examples of $A_{\mathrm{eff}}(x)$ were calculated numerically with MATLAB and SciPy[1].

---

[1] Scientific Tools for Python, http://www.scipy.org.

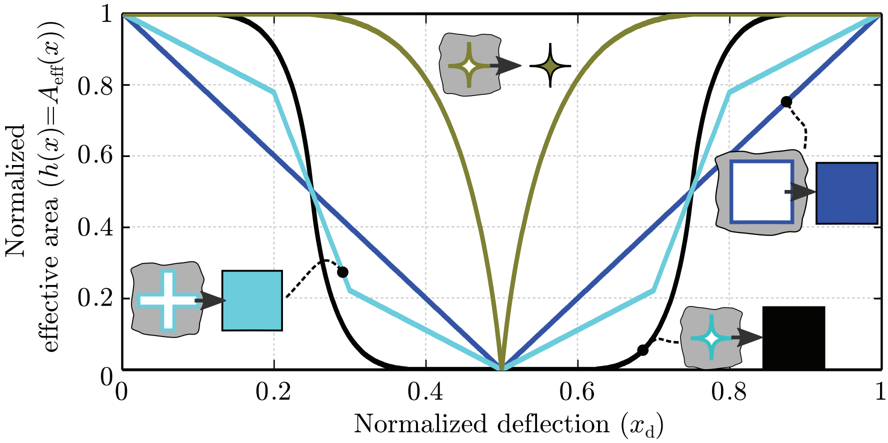

Figure 4.15: Convolution results for different pairs of apertures. Each curve was normalized by the corresponding maximum value of A_{eff}. White areas in the depicted apertures are transparent. Dependent on the form of the apertures linear, partially linear, continuous or partially continuous transfer characteristics can be achieved.

The influence of the determined deflection dependent output characteristics onto time dependent input deflection is demonstrated in the following subsection."[41]

4.5.2 Time Signal Examples

"If the apertures are sinusoidally shifted with respected to each other, x_{d} becomes dependent in time as shown in the lower left diagram of Fig. 4.16. By different offsets of sinusoidal curves of $x_{\text{d}}(t)$ the time dependent output related function $A_{\text{eff}}(t)$ is mapped out of the shape of $A_{\text{eff}}(x_{\text{d}})$. This mapping is indicated by arrows illustrated in Fig. 4.16 and Fig. 4.17. As the time signals in Fig. 4.16 indicate, the system behaves like a mechanical rectifier when the apertures are deflected according to $x(t) = x_{\text{d}}(t) = \hat{x}_{\text{d}} \sin(\omega t)$ around the completely intransparent point of operation where $A_{\text{eff}}(x) = 0$. If the operation point is set on one of the two particular linear slopes of the curve of A_{eff} and it is ensured that a further deflection will not exceed the linear parts of $A_{\text{eff}}(x)$, the signal input x_{d} can be recovered out of $A_{\text{eff}}(t) = \hat{A}\sin(\omega t)$.

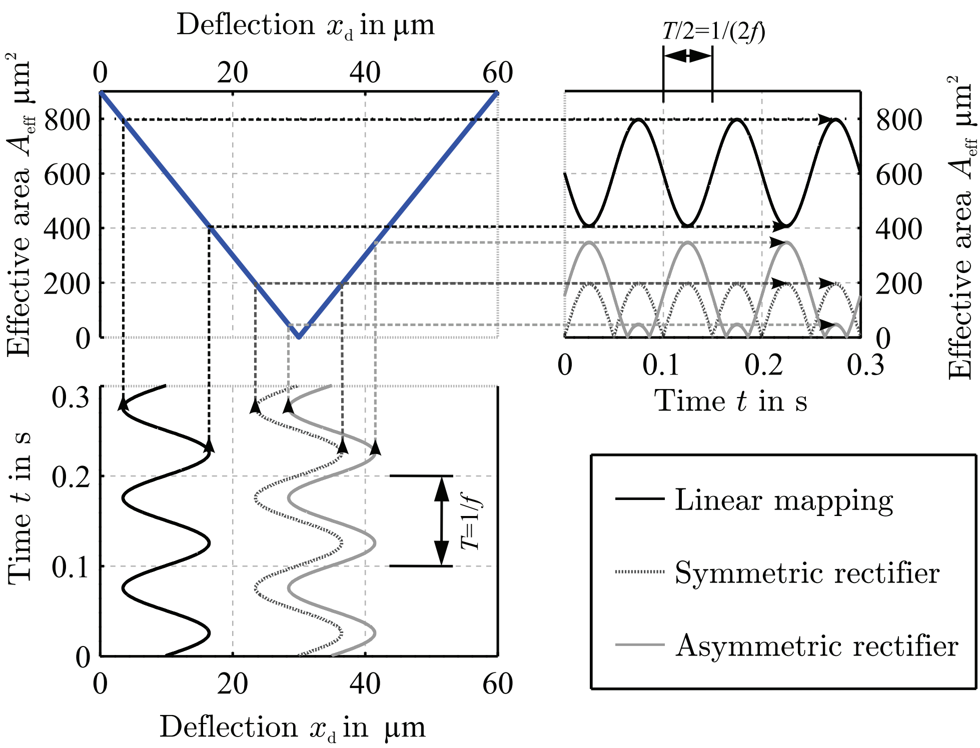

Figure 4.16: Examples for the output time signal of the effective area caused by relative sinusoidal movement of two rectangular apertures. Three different main cases are depicted: linear mapping from input deflection to output signal; symmetric and asymmetric 'rectifier' where parts of the input signal become inverted dependent on the position of the aperture.[41]

Depending on the combination of different geometries (Fig. 4.15) the input/output characteristics [may or may not contain] discontinuities. For example, the convolution of a star geometry with a rectangular shaped and intransparent aperture yields a smooth, continuous but inherent nonlinear output behavior (Fig. 4.17). On the other hand, the combination of two stars results in a transfer characteristics with a discontinuity at the point where $A_{\text{eff}}(x)$ is equal to zero. All presented aperture geometries were symmetric to x. An asymmetric geometry function $f(x)$ [also] results in an asymmetric transfer behavior of $A_{\text{eff}}(x)$ offering additional design capability, [such as] implementing nonlinear device characteristics by hardware."[41]

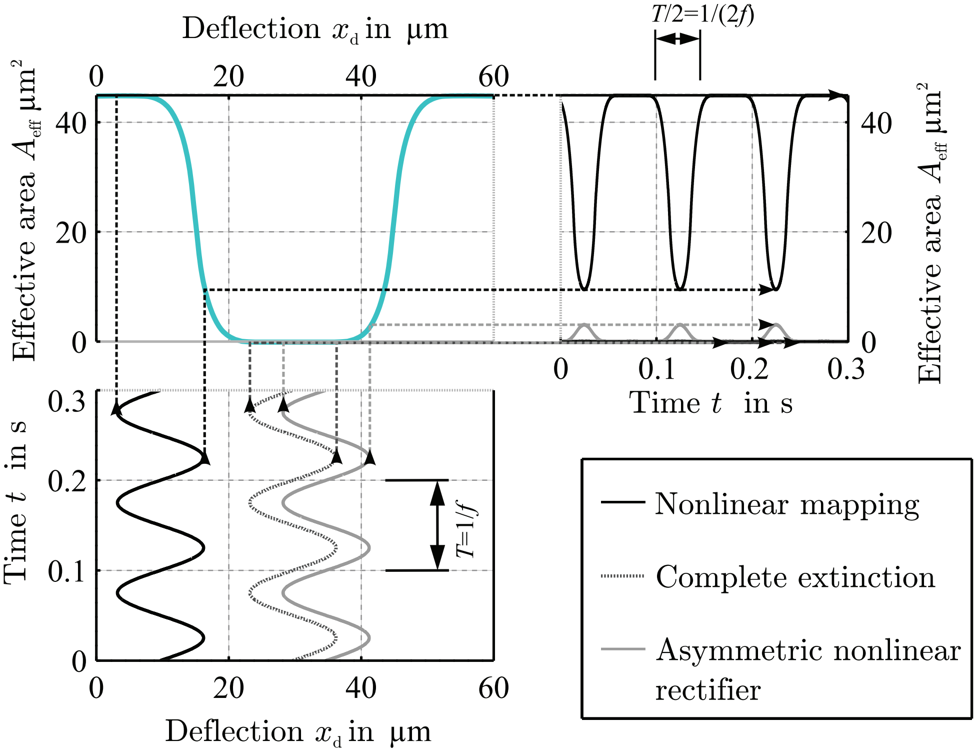

Figure 4.17: Examples for the output signal when moving a rectangular-shaped aperture sinusoidal over a star-shaped one. All three input deflection signals are nonlinear transfered to the output. It is also possible to cancel out special input deflection ranges.[41]

4.6 Two-Dimensional Deconvolution Limitations

Analog to the 1D deconvolution operation in subsection 4.3.4 it is also possible to deconvolve 2D functions. Fig. 4.18 serves as an example that the restrictions to the apertures to be real-valued and positive are more severe in the 2D case. Hence, computation of the second aperture shape from a predefined 2D output-transfer-function and a given 2D aperture was not possible because it produced complex-valued results. The real part of the computed aperture-function is depicted in the upper right part of Fig. 4.18.

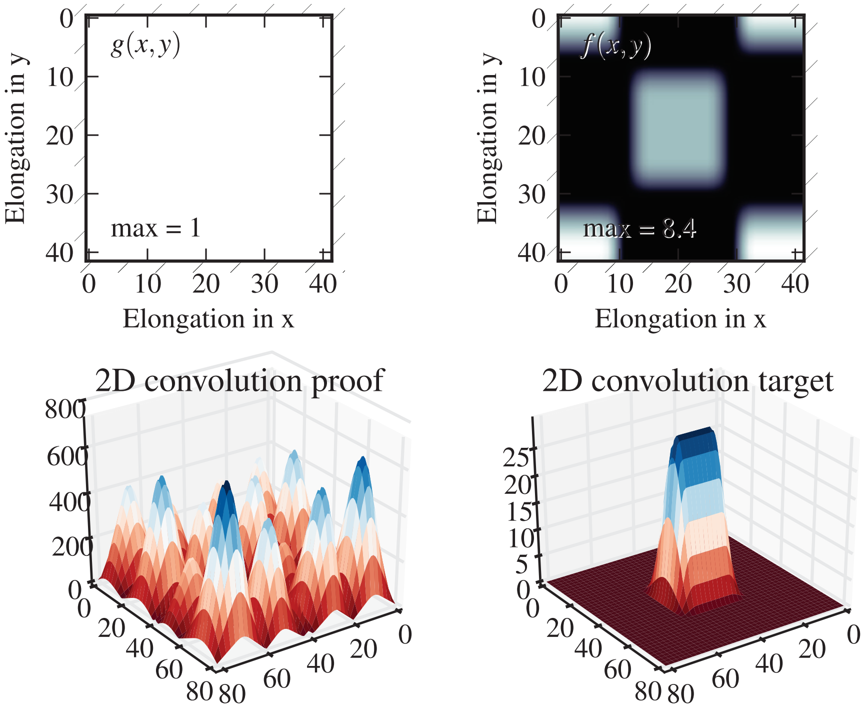

Figure 4.18: Example of the 2D deconvolution of a given 2D output characteristic resulting one aperture shape which is shown in the lower right. The requested transfer function is a $\sin^2(y)$ along the $y-$axis and a $\sin^2(x)$ with a plateau along the $x-$axis. The upper left plot depicts the predefined aperture which is completely transparent. The upper right plot illustrates the real values of the identified aperture. The lower left plot shows the convolution of the prespecified aperture with the identified one which does not match the requested output transfer function.

Convolving the prespecified aperture $f(x, y)$ with the computed aperture $g(x, y)$ yield the result depicted in the lower left of Fig. 4.18 which does not fit the original defined transfer function.

A computation analog to the algorithm discussed in Sec. 4.4 is still possible but has to be done column after column and row after row of the requested 2D output function.

Chapter 5

Conclusion

The features of a novel transduction of relative displacement was investigated exploiting MEMS arrangements for vibration detection. The displacement was generated by inertial forces acting on a spring suspended plate made from monocrystalline silicon. The plate exhibits a regular array of microapertures through which a light source shines on a photodetector. A second mask, featuring congruently positioned openings is fixed to the silicon frame by a dedicated hybrid technology. Both masks combine to form a variable aperture. The size is controlled by the displacement of the spring suspended plate. The mask arrangement translates the relative displacement into variations of the light flux received by the photodetector that is further converted into electrical signals.

This work proves that the conversion procedure combines an exceptionally large dynamic range for displacements with a great freedom for shaping of the conversion characteristic.

Investigated implementations of the transducer concept merge instances of the described light flux modulator with low cost LED's and 2D-photodetectors. Such prototypes achieved displacement ranges of several µm combined with encouraging sub $1\,\mathrm{pm}/\sqrt{\mathrm{Hz}}$ resolutions corresponding to sub $1\,\mu\mathrm{g}/\sqrt{\mathrm{Hz}}$ in terms of acceleration (Fig. 5.1). Moreover, the change in relative displacement between the masks can originate from a variety of forces. Beside inertial forces, any quantity that can be translated into spatial displacement may be converted as well. Thus gravitation, magnetic and electrostatic field related forces, pressure or temperature expansion can be easily covered with this transduction principle.

Due to the freely selectable shape of the mask apertures, the light flux modulator inherits a unique potential to manipulate the displacement-to-light flux transfer. This work presents a thorough analysis of the crucial relationships. Appropriate aperture shaping enables a linear relation between the electronic output signal and the particular input quantity. Alternatively, a desired dynamic compression is feasible enabling constant relative resolution, for example. Such properties can be achieved without any need for additional electronic circuitry.

5.1 Outlook

All presented results in this thesis were obtained from a first set of prototypes, confirming the introduced model for sensitivity and noise floor of the sensor. These confirmed models and design criteria now allow the development of further improved sensor devices.

5.1.1 Potential for Further Enhancement

The displacement resolution can further be improved by increasing the effective moving edge length l_e during mask design while considering the fabrication related issues for narrower apertures and the available chip area. It should be stated however, that enhanced resolution is very probably achieved at the cost of reduced dynamic range.

The lowest resolvable deflection is limited by the fluctuations of the dark current and the thermal noise of the mechanical system. The noise level of the opto-electrical components can be further reduced using advanced photodetectors featuring a lower dark current noise.

The presented MOEMS sensors were characterized at atmospheric pressure. Lowering the pressure inside the sensor housing results in a reduction of the thermo-mechanical induced Brownian noise and an increase in the quality factor of the mechanical system. However, it seems worth investing in the development of MEMS with reduced thermo-mechanical damping without the need of hermetically sealed devices. Further studies have to be carried out to predict the not yet fully understood damping behavior of a high-definition MEMS part. Due to the hybrid assembly of the MEMS and commercially available opto-electrical components, the devices developed during this thesis are not fully integrated ones. Consequently, a further increase in sensitivity can be expected from integrated implementations on chip-level of the light transmitter, the receiver, and the TIA. However, further integration may raise additional issues such as the homogeneous illumination of larger aperture arrays when integrating the light transmitter and the fixed aperture.

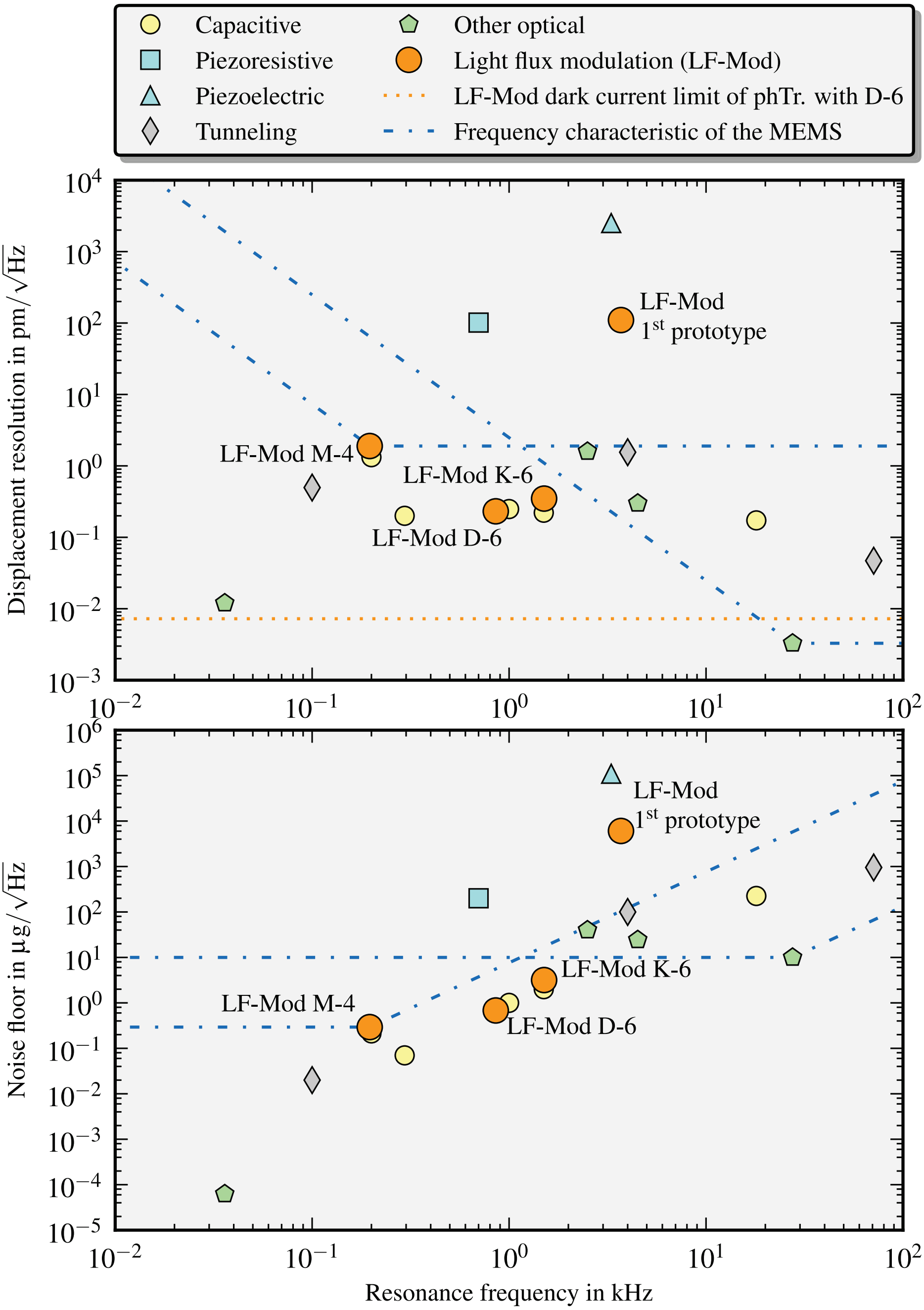

Figure 5.1: Displacement and acceleration resolutions of various MOEMS sensors. The corresponding frequency characteristics of a critically damped mass-spring transducer (blue dot-dashed line) is schematically added to indicate the course characteristic of displacement resolution for different sensors. Furthermore, the achieved data of the first handcrafted demonstrator (LF-Mod 1^{st} prototype) and the latest achieved results are included. The dotted line indicates the detection limit corresponding to the dark current noise of the phototransistor (PhTr). The corresponding citations can be found in Fig. 1.1 and the related measurement data is listed in Table 3.5.

Considering the available potential for improvement, a femto-meter resolution seems to be reachable with this versatile and cost-effective intensity modulation method.

The potential for further enhancements can be summarized as:

- Signal to noise ratio improvement due to reduction of gas damping; Encapsulated MOEMS devices operated at lowered gas pressure exhibit a enhanced signal to noise ratio inversely proportional to the gas damping (Eq. 2.30, 2.31).
- Development of advanced light detection circuitry and use of adopted optoelectronics components; Fabrication and usage of tailored designed LEDs or PIN diodes incorporating the fixed aperture together with an integrated TIA. During the redesign of the receiver, special attention has to be given to the dark current of the receiver, which limits the resolution of the opto-electronic readout. A modulation of the light flux generated by the LED and an adjusted demodulation at the receiver can be used to reduce the overall power consumption while avoiding 1/f noise at low frequencies and drift regarding the temperature and the voltage supply.
- Enhancing the seismic mass by using wafer-thin MEMS in conjunction with the infrared approach; A redesign of the current proof-of-concept structures is mandatory for operating them with the infrared readout which enables a further increase in seismic mass and, therefore, improves the signal to noise ratio (Eq. 2.30, 2.31) while simplifying the fabrication process.

5.1.2 Applications

Plenty of sensor characteristics are feasible by designing the shape of the apertures, offering a variety of opto-mechanical transfer characteristics and therefor different applications.

During the time of writing this thesis an international patent (PCT/EP2012/057098) concerning the MOEMS sensor principle was filed. The patent covers the usage of the sensors as readout for all kinds of forces acting onto the movable grating in combination with the implementation of an opto-mechanical transfer function.

Various applications are also feasible due to the inherent galvanic separation of the force or deflection inputs and the opto-electronic signals. The optical readout in combination with a fiber optical link to the evaluation circuit allows the sensor to be operated in harsh environments, e.g., for magnetic field measurements in high or low temperature environments. Specially designed electro-static actuators inside the MOEMS allow their application as electric field sensors, which are read by optical fibers. No electrical connections are needed for the MEMS part, ensuring minimum distortion of to the electric field to be measured.

The main fields of application can be summarized as:

- Displacement sensor or accelerometer; The applicability as displacement sensor or accelerometer with high resolution was demonstrated within this thesis. Further investigation is needed to analyze the operation of these MOEMS in harsh environments such as in high electromagnetic fields or at extreme temperatures.
- Integrated MOEMS voltage sensor with galvanic separation; This type of sensor was already implemented within this thesis and was used in a reversed manner for the characterization of the aperture related noise behavior (Sec. 3.5). There, the width of the aperture was controlled by a voltage applied to comb-drives incorporated into the MOEMS. The nonlinear dependency of the deflection on the applied voltage can be compensated with appropriate design of the shape of the apertures.
- Fiber-optic MOEMS sensor for electrostatic field measurements; This sensor is similar to the voltage sensor but features a fiber optical readout to ensure minimal distortion of the field to be measured. Finally, shielding and unwanted mechanical vibrations have to be considered to gain maximum sensitivity while keeping the field interference at a minimum.

Bibliography

[1] A.A. Barlian, W.-T. Park, J.R. Mallon, A.J. Rastegar, and B.L. Pruitt. Review: Semiconductor piezoresistance for microsystems. *Proceedings of the IEEE*, 97(3):513 –552, march 2009.

[2] Neil Barbour and George Schmidt. Inertial sensor technology trends. *IEEE Sensors Journal*, 1(4):332–339, 2001.

[3] Kensall D. Wise. Integrated sensors, MEMS, and microsystems: Reflections on a fantastic voyage. *Sensors and Actuators A: Physical*, 136(1):39 – 50, 2007.

[4] Marc J. Madou. *Fundamentals of Microfabrication and Nanotechnology: From MEMS to Bio-MEMS and Bio-NEMS : manufacturing techniques and applications*. Fundamentals of Microfabrication and Nanotechnology. Taylor & Francis Group, 2012.

[5] Michael Kraft. Micromachined inertial sensors: The state of the art and a look into the future. *IMC Measurement and Control*, 33:164–168, 2000.

[6] D.L. DeVoe and A.P. Pisano. Surface micromachined piezoelectric accelerometers (pixls). *Microelectromechanical Systems, Journal of*, 10(2):180 –186, June 2001.

[7] Cheng-Hsien Liu and T.W. Kenny. A high-precision, wide-bandwidth micromachined tunneling accelerometer. *Microelectromechanical Systems, Journal of*, 10(3):425 –433, September 2001.

[8] Chingwen Yeh and K. Najafi. Micromachined tunneling accelerometer with a low-voltage cmos interface circuit. In *Solid State Sensors and Actuators, 1997. TRANSDUCERS '97 Chicago., 1997 International Conference on*, volume 2, pages 1213–1216, June 1997.

[9] R.L. Kubena, G.M. Atkinson, W.P. Robinson, and F.P. Stratton. A new miniaturized surface micromachined tunneling accelerometer. *Electron Device Letters, IEEE*, 17(6):306 –308, June 1996.

[10] Adxl105 datasheet. ADXL105: ±5g Single Axis High Performance Accelerometer with Analog Output.

[11] J. Bernstein, R. Miller, W. Kelley, and P. Ward. Low-noise MEMS vibration sensor for geophysical applications. *Journal of Microelectromechanical Systems*, 8(4):433–438, 1999.

[12] B. Homeijer, D. Lazaroff, D. Milligan, R. Alley, J. Wu, M. Szepesi, B. Bicknell, Z. Zhang, R.G. Walmsley, and P.G. Hartwell. Hewlett packard's seismic grade MEMS accelerometer. In *Micro Electro Mechanical Systems (MEMS), 2011 IEEE 24th International Conference on*, pages 585 –588, 2011.

[13] Xuesong Jiang, Feiyue Wang, Michael Kraft, , and Bernhard E. Boser. An Integrated Surface Micromachined Capacitive Lateral Accelerometer with 2ug/sqrt(Hz) Resolution. *Solid-State Sensor, Actuator and Microsystems Workshop*, 2002.

[14] A. Partridge, J.K. Reynolds, B.W. Chui, E.M. Chow, A.M. Fitzgerald, L. Zhang, N.I. Maluf, and T.W. Kenny. A high-performance planar piezoresistive accelerometer. *Microelectromechanical Systems, Journal of*, 9(1):58 –66, March 2000.

[15] U. Krishnamoorthy, D.W. Carr, G.R. Bogart, M.S. Baker, and R.H. Olsson. In-Plane Nano-G Accelerometer Based on an Optical Resonant Detection System. In *Solid-State Sensors, Actuators and Microsystems Conference, 2007. TRANSDUCERS 2007. International*, pages 1195 –1198, 2007.

[16] N.A. Hall, M. Okandan, R. Littrell, D.K. Serkland, G.A. Keeler, K. Peterson, B. Bicen, C.T. Garcia, and F.L. Degertekin. Micromachined accelerometers with optical interferometric read-out and integrated electrostatic actuation. *Microelectromechanical Systems, Journal of*, 17(1):37 –44, 2008.

[17] O. Bochobza-Degani, R. Yechieli, S. Bar-Lev, U.B. Yehuda, and Y. Nemirovsky. Characterization of a novel micromachined accelerometer with enhanced-midos. *Transducers, Solid-State Sensors, Actuators and Microsystems, 12th International Conference on, 2003*, 2:1395 – 1398, jun. 2003.

[18] Alexander G. Krause, Lin Qiang, and Painter Oskar. A high-resolution microchip optomechanical accelerometer. *Nature photonics*, 6:768–772, 2012.

[19] Thomas M. Adams and Richard A. Layton. *Introductory MEMS*. Springer US, 2010.

[20] G. Krishnan, C. U. Kshirsagar, G. K. Ananthasuresh, and N. Bhat. Micromachined high-resolution accelerometers. *Journal of the Indian Institute of Science*, 87(3):333–361, 2007.

[21] Cenk Acar and Andrei M Shkel. Experimental evaluation and comparative analysis of commercial variable-capacitance MEMS accelerometers. *Journal of Micromechanics and Microengineering*, 13(5):634, 2003.

[22] T. Kenny. Nanometer-scale force sensing with MEMS devices. *Sensors Journal, IEEE*, 1(2):148–, 2001.

[23] Mohamed Gad el Hak. *The MEMS Handbook*. CRC Press LLC, 2002.

[24] Navid Yazdi, Farrokh Ayazi, and Khalil Najafi. Micromachined inertial sensors. *Proceedings of the IEEE*, 86:1640 – 1659, 1998.

[25] A. Fargas-Marques and A.M. Shkel. On electrostatic actuation beyond snapping condition. In *Sensors, 2005 IEEE*, page 4, Nov. 2005.

[26] Tao Chen, Liguo Chen, Lining Sun, and Xinxin Li. Design and fabrication of a four-arm-structure MEMS gripper. *Industrial Electronics, IEEE Transactions on*, 56(4):996–1004, 2009.

[27] W. Hortschitz, H. Steiner, T. Sauter, F. Kohl, M. Sachse, M. Stifter, F. Keplinger, and J. Schalko. Robust precision position detection with an optical MEMS hybrid device. *Industrial Electronics, IEEE Transactions on*, PP(99):1, 2012.

[28] R.G. Walmsley, M.A. Hopcroft, P.G. Hartwell, G. Corrigan, and D. Milligan. Three-phase capacitive position sensing. In *Sensors, 2010 IEEE*, pages 2658 –2661, nov. 2010.

[29] G. Langfelder, Antonio Longoni, A. Tocchio, and E. Lasalandra. MEMS Motion Sensors Based on the Variations of the Fringe Capacitances. *Sensors Journal, IEEE*, 11(4):1069–1077, 2011.

[30] A. Tocchio, G. Langfelder, A. Longoni, and E. Lasalandra. In-plane and out-of-plane MEMS motion sensors based on fringe capacitances. *Procedia Engineering*, 5(0):1392 – 1395, 2010.

[31] O.D. Bernal, K. Choe, P.K. Gopalakrishnan, Hsiu-Yu Cheng, K.R. Krishna, D. Nuttman, N. Axelrod, and Minkyu Je. A low-power high-performance accelerometer ASIC for high-end medical motion sensing. In *Engineering in Medicine and Biology Society (EMBC), 2010 Annual International Conference of the IEEE*, pages 190–193, 2010.

[32] W. Bracke, P. Merken, R. Puers, and C. Van Hoof. On the optimization of ultra low power front-end interfaces for capacitive sensors. *Sensors and Actuators A: Physical*, 117(2):273 – 285, 2005.

[33] H. Baltes, O. Brand, G.K. Fedder, C. Hierold, J.G. Korvink, and O. Tabata. *CMOS-MEMS: Advanced Micro and Nanosystems*. Advanced Micro and Nanosystems. John Wiley & Sons, 2008.

[34] S Tadigadapa and K Mateti. Piezoelectric MEMS sensors: state-of-the-art and perspectives. *Measurement Science and Technology*, 20(9):092001, 2009.

[35] Jian Lu, Yi Zhang, T. Itoh, and R. Maeda. Design, fabrication, and integration of piezoelectric MEMS devices for applications in wireless sensor network. In *Design, Test, Integration and Packaging of MEMS/MOEMS (DTIP), 2011 Symposium on*, pages 217–221, 2011.

[36] B.E.N. Keeler, D.W. Carr, J.P. Sullivan, T.A. Firedmann, and J.R. Wendt. Experimental demonstration of a laterally deformable optical nanoelectromechanical system grating transducer. *Optics Letters*, 29(11):1182–1184, 2004.

[37] Ebrahim Abbaspour-Sani, R.-S. Huang, and Chee Yee Kwok. A novel optical accelerometer. *Electron Device Letters, IEEE*, 16:166 – 168, 1995.

[38] N. Lindenmann, G. Balthasar, D. Hillerkuss, R. Schmogrow, M. Jordan, J. Leuthold, W. Freude, and C. Koos. Photonic wire bonding: a novel concept for chip-scale interconnects. *Opt. Express*, 20(16):17667–17677, Jul 2012.

[39] F. Mohd-Yasin, C.E. Korman, and D.J. Nagel. Measurement of noise characteristics of MEMS accelerometers. In *Semiconductor Device Research Symposium, 2001 International*, pages 190 –193, 2001.

[40] F Mohd-Yasin, D J Nagel, and C E Korman. Noise in MEMS. *Measurement Science and Technology*, 21(1):012001, 2010.

[41] Wilfried Hortschitz, Franz Kohl, Harald Steiner, Matthias Sachse, Johannes Schalko, and Franz Keplinger. Design of linear and nonlinear hybrid optical MEMS displacement sensors. In *Smart Sensors, Actuators, and MEMS V*, volume 8066, pages 80660 P–1 – 80660 P–9, 2011.

[42] T.B. Gabrielson. Mechanical-thermal noise in micromachined acoustic and vibration sensors. *IEEE Transactions on Electron Devices*, 40:903 – 909, May 1993.

[43] Christian Riesch. *Micromachined Viscosity Sensors*. PhD thesis, Oct. 2009.

[44] Francisco H. De La Moneda, Eugene R. Chenette, and Aldert Van Der Ziel. Noise in phototransistors. *IEEE Transactions on Electron Devices*, ED-18:340–346, 1971.

[45] K.B. Cook and V.W. Ruwe. A phototransistor optical isolator noise model. *Solid-State Circuits, IEEE Journal of*, 15(3):361 – 365, Jun 1980.

[46] Ofir Bochobza-Degani, Dan J. Seter, Eran Socher, and Yael Nemirovsky. Design and noise consideration of an accelerometer employing modulated integrative differential optical sensing. *Sensors and Actuators A: Physical*, 84(1-2):53 – 64, 2000.

[47] Wilfried Hortschitz, Franz Kohl, Matthias Sachse, Michael Stifter, Thilo Sauter, Harald Steiner, Johannes Schalko, Artur Jachimowicz, and Franz Keplinger. Noise considerations on hybrid optical MEMS displacement sensors. In *Sensors, 2011 IEEE*, pages 363 –366, oct. 2011.

[48] M.A. Hopcroft, W.D. Nix, and T.W. Kenny. What is the Young's Modulus of Silicon? *Microelectromechanical Systems, Journal of*, 19(2):229 –238, april 2010.

[49] W. Hortschitz, H. Steiner, M. Sachse, F. Kohl, J. Schalko, and F. Keplinger. Hybrid optical MEMS vibration sensor. *Procedia Engineering*, 5(0):420 – 423, 2010.

[50] W. Hortschitz, M. Sachse, H. Steiner, F. Kohl, T. Sauter, J. Schalko, and F. Keplinger. Optical MEMS vibration sensor. In *Sensors, 2010 IEEE*, pages 1731 –1735, 2010.

[51] W. Hortschitz, H. Steiner, M. Sachse, M. Stifter, F. Kohl, J. Schalko, A. Jachimowicz, F. Keplinger, and T. Sauter. An Optical In-Plane MEMS Vibration Sensor. *Sensors Journal, IEEE*, 11(11):2805 –2812, nov. 2012.

[52] Wilfried Hortschitz, Andreas Kainz, Joerg Encke, Franz Kohl, Harald Steiner, Michael Stifter, Thilo Sauter, and Franz Keplinger. Exploiting Infrared Transparency of Silicon for the Construction of Advanced MOEMS Vibration Sensors. In *Smart Sensors, Actuators, and MEMS V*, 2013.

[53] D. Meschede and C. Gerthsen. *Gerthsen Physik*. Springer-Lehrbuch. Springer, 2010.

[54] Jeff Hecht. *Semiconductor Diode Lasers*, pages 265–316. John Wiley & Sons, Inc., 2008.

[55] Martin A. Green. Self-consistent optical parameters of intrinsic silicon at 300 k including temperature coefficients. *Solar Energy Materials and Solar Cells*, 92(11):1305 – 1310, 2008.

[56] J. Iyer. Photodetectors demystified. *Potentials, IEEE*, 12(4):5 –10, dec. 1993.

[57] H. Beneking. Gain and bandwidth of fast near-infrared photodetectors: A comparison of diodes, phototransistors, and photoconductive devices. *Electron Devices, IEEE Transactions on*, 29(9):1420 – 1431, sep 1982.

[58] H. Steiner, M. Sachse, J. Schalko, W. Hortschitz, F. Kohl, and A. Jachimowicz. Experimental setup for the coating of chlorosilane based self assembling monolayers to reduce stiction in MEMS devices. In *Smart Sensors, Actuators, and MEMS V*, pages 806624–806624–9, 2011.

[59] St.J. Dixon-Warren. Motion sensing in the iPhone 4: MEMS accelerometer http://www.memsjournal.com/2010/12/motion-sensing-in-the-iphone-4-mems-accelerometer.html, 02 2013.

[60] Johannes Schalko. Private communication.

[61] M.J.A. MADOU. *Fundamentals of Microfabrication: The Science of Miniaturization, Second Edition*. Taylor & Francis Group, 2002.

[62] Polytec. *VD-02 Velocity Decoder - MEASURING VIBRATION VELOCITY*.

[63] Wilfried Hortschitz, Joerg Encke, Franz Kohl, Thilo Sauter, Harald Steiner, Michael Stifter, and Franz Keplinger. Receiver and amplifier optimization for hybrid MOEMS. In *Sensors, 2012 IEEE*, pages 1 –4, oct. 2012.

[64] Wilfried Hortschitz, Joerg Encke, Franz Kohl, Thilo Sauter, Harald Steiner, Michael Stifter, and Franz Keplinger. Optimized hybrid MOEMS sensors based on noise considerations. In *Sensors, 2012 IEEE*, pages 1 –4, oct. 2012.

[65] L. Pavesi and D.J. Lockwood. *Silicon Photonics*. Number Bd. 1 in Topics in Applied Physics. Springer, 2004.

[66] *Roithner Lasertechnik - InGaAs Large Area Photodiode - LAPD-series*.

[67] *Osram - SFH4680 - Narrow beam LED in MIDLED package*.

[68] *Osram - SFH3600 - Phototransistor in MIDLED package*.

[69] Sophocles J. Orfanidis. Electromagnetic waves and antennas, 8 2010.

[70] E.D. Palik. *Handbook of Optical Constants of Solids, Volumes I, II, and III: Subject Index and Contributor Index*. Academic Press Handbook Series. Elsevier Science & Tech, 1985.

[71] Refractiveindex.info, http://refractiveindex.info, 03 2013.

[72] Anti-reflection coating on silicon wafer, http://www.accucoatinc.com/ac_155.html, 03 2013.

[73] M. Cid, N. Stem, C. Brunetti, A.F. Beloto, and C.A.S. Ramos. Improvements in anti-reflection coatings for high-efficiency siliconsolar cells. *Surface and Coatings Technology*, 106:117 – 120, 1998.

[74] D. Wolf. *Noise in physical systems: proceedings of the Fifth International Conference on Noise, Bad Nauheim, Fed. Rep. of Germany, March 13-16, 1978*. Springer series in electrophysics. Springer, 1978.

[75] H.J. Dirschmid. *Mathematische Grundlagen der Elektrotechnik: Graph. Darst*. Number Bd. 1. Vieweg, 1990.

[76] I.N. Bronstein and K.A. Semendjajew. *Taschenbuch der Mathematik*. Deutsch Harri GmbH, 2008.

[77] A. Theuwissen. Cmos image sensors: State-of-the-art and future perspectives. In *Solid State Circuits Conference, 2007. ESSCIRC 2007. 33rd European*, pages 21 –27, sept. 2007.

[78] R. Fontaine. Recent innovations in cmos image sensors. In *Advanced Semiconductor Manufacturing Conference (ASMC), 2011 22nd Annual IEEE/SEMI*, pages 1 –5, may 2011.

[79] Jonghwa Jeong, Debra Mascaro, and Steve Blair. Precise pixel patterning of small molecule organic light-emitting devices by spin casting. *Organic Electronics*, 12(12):2095 – 2102, 2011.

[80] M. Ogihara, T. Sagimori, M. Mutoh, T. Suzuki, T. Igari, H. Furuta, Y. Nakai, S. Morisaki, H. Fujiwara, I. Abiko, and M. Sakuta. 1200dpi thin film LED array by silicon photonics technology. In *Electronic Components and Technology Conference, 2008. ECTC 2008. 58th*, pages 765–772, 2008.

[81] S.M. Kay. *Fundamentals Of Statistical Signal Processing*. Prentice Hall, 2001.

[82] A.V. Oppenheim and R.W. Schafer. *Discrete-time signal processing*. Prentice-Hall signal processing series. Prentice Hall, 2010.

Acknowledgments

First of all I want to thank my family for supporting me especially over the last years.

Second, I would like to express my deep gratitude to my supervisor and mentor Franz Kohl for his guidance and support. His tremendous expertise in the field of sensors, together with his altruistic willingness to contribute in numerous ways, has significantly influenced the quality of this work. Nevertheless, it was also fun to work with Franz.

I want to express my deepest gratitude to Prof. Dr. Franz Keplinger for his encouragement and marvelous support during the last years. He always asked the ultimately important questions which helped me improving my experimental set-up and the developed sensor models.

I want to express my gratitude to Prof. Vittorio Ferrari for his kind disposition to review this thesis.

My gratitude goes to my PhD study colleagues Harald Steiner and Michael Stifter for the productive discussions on research topics, for their friendship and for their support in all phases of the thesis. These discussions and countless rounds of table soccer finally made this work a success.

I want to show my gratitude to Jörg Encke and Andreas Kainz for their support and help when setting up the measurements in Vienna and their valuable discussions not only on the field of sensors. They were also excellent conference fellows and did keep up a fine working atmosphere. I want to thank Roman Beigelbeck for his valuable support and the discussions on most of the analytical models presented in this thesis. Furthermore, I want to thank Steve McDermott and Andreas Kainz for reviewing my thesis and correcting numerous ’ly’s and linguistic terms.

For generally supporting my research on the Center for Integrated Sensor Systems (CISS) in Wiener Neustadt I want to thank Thilo Sauter and Albert Treytl. This work was financially supported by the Austrian Research Promotion Agency FFG, Project TRP 226-N24 and the province of Lower Austria, which was kindly acknowledged.

Technological discussions with Artur Jachimovicz and Johannes Schalko were instrumental in making this work a success. For their support in processing the sensors I want to thank Peter and Edeltraud Svacek. For realizing some of the electronics circuits I want to thank Gábor Kovacs, and Johannes Steurer for the valuable discussions and his advise regarding the selection of electronic components. My thanks also goes to Ewald Pirker for fabricating the crucial mechanical parts of the measurement system.

Special thanks are devoted to Matthias Sachse and the colleagues in Wiener Neustadt for all sorts of discussions and inspiration.

Finally but foremost I owe my deepest gratitude to my wife Sabine for always being supportive and patient. Thank you for your continuous love and support during the course of this thesis!

Curriculum Vitae

Education

2007	**Dipl.-Ing. degree**, Johannes Kepler University Linz, Upper-Austria, Development of a low-cost sensor for online-grain-counting
1998	**Matura**, HTBLuVA - Mechanical Engineering (Federal Higher Technical Institute for Educating), Wiener Neustadt, Lower-Austria

Experience

2007 – 2013	**Researcher**, Austrian Academy of Sciences, IISS, Capacitive MEMS for implantable devices and MOEMS displacement sensors
2008 – 2010	**Lecturer**, University of Applied Sciences Wiener Neustadt, Methodological development of Microsystems
2009 – 2013	**Ph.D. student**, Vienna University of Technology, ISAS
2013 – cur.	**Researcher**, Danube University Krems, ZISS, Design of hybrid MOEMS sensors

Additional Skills and Interests

MEMS Mechatronics	Sensor development and interdisciplinary working. Development of all sorts of electro mechanical systems with a focus on MOEMS.